POLITECNICO DI TORINO

MASTER THESIS

**MONITORING GLACIERS USING GIS AND OPEN
SOURCE SATELLITE DATA**

AUTHOR:

Neeraj Chowdary Jonnalagaddda

SUPERVISOR

Prof:.Marco Piras

CO-SUPERVISOR

Prof:.Stefania Tamea

POLITECNICO DI TORINO

Abstract

Faculty Name

Dipartimento di Ingegneria dell'Ambiente, del Territorio e delle Infrastrutture

Master's degree Civil Engineering

Monitoring Glaciers using GIS and Open-source satellite data.

By Neeraj Chowdary Jonnalagadda

Due to climate change, it has become essential and necessary to monitor the critical land masses of the Earth in this thesis we are going to see how the Belvedere glacier which is located in the northwest part of Italy in Italian alps can be monitored Earth observation technologies. Since this glacier is very unstable the local geomorphology of the glacier varies continuously with time and space, so it is not very safe to collect data on site using laser scanning and photogrammetric techniques etc. Thanks to advances in space science we can now monitor any part earth surface and atmospheric variables around any time of the year using active remote sensing and passive remote sensing .The main emphasis of this thesis is that DEM's generated using stereo optical images pairs from Spot 5 satellite which belongs to passive remote sensing and SAR interferometry techniques using sentinel 1 radar images which belongs to active remote sensing and check the quality of DEM'S from both the approaches or technologies and try to answer the question are they are reliable to calculate the volume of the glacier lost over a period from 2003 to 2016 and compare the volume lost in the glacier to the discharge measured with Hydrologiska Byråns Vattenbalansavdelning(HBV) model used to analyse discharge in the catchment where the glacier is located for which essential climate variables such as precipitation, temperature and stream flow of the catchment are used as input to model the discharge in the catchment.

Acknowledgments

CONTENTS

LIST OF TABLES

LIST OF FIGURES

LIST OF ABREVATIONS

IPCC-Intergovernmental Panel on Climate **C**hange

DEM -Digital Elevation Model

GSD-Ground Sampling Distnace

InSAR Interferometric synthetic aperture radar

SREX Special Report on Managing the Risks of Extreme Events

ELA   Equilibrium line altitude

AAR   Area accumulation ratio

GNSS Global navigation satellite system

LiDAR Light detection and ranging

SNAP   Sentinel application platform

TM   Thematic mapper

ETM+ Enhanced Thematic mapper plus

MSS   Multi spectral scanner

OLI   Operational Land Imager

TIRS   Thermal Infrared Sensor

HRIV   High Resolution Visible and Infrared

HRV   High Resolution Visible

HRS   High Resolution Stereoscopic

HRG   High Resolution Geometry

SWIR   Short wave Infra Red

NAOMI New Astrosat Optical Modular Instrument

SAR   Synthetic Aperture Radar

GIS   Geographic Information Systems

Chapter 1

Introduction

High mountain regions share common features, including rugged terrain, a low-temperature climate regime, steep slopes and institutional and spatial remoteness. These features are often linked to physical and social-ecological processes that, although not unique to mountain regions, typify many of the special aspects of these regions. Due to their higher elevation compared with the surrounding landscape, mountains often feature cryosphere components, such as glaciers, snow cover and permafrost, with a significant influence on surrounding lowland areas even far from the mountains [1]. Hence the mountain cryosphere plays a major role in large parts of the world. Considering the close relationship between mountains and the cryosphere, high mountain areas are addressed in a dedicated chapter within this special report. Almost 10% (671 million people) of the global population lived in high mountain regions in 2010, based on gridded population data and this population is expected to grow to 736–844 million across the shared socioeconomic pathways by 2050[2]. Many people living outside of mountain areas and not included in these numbers are also affected by changes in the mountain cryosphere. Now the topic which we are interested in this thesis is not entire cryosphere but just one portion of it which is glacier. Glaciers are the largest reservoir of fresh of water on planet. They supply water by melting during summer that supports human communities both close to the glacier and far away from the glacier, for example for agriculture or drinking water . Most important rivers in world are fed from the melt of the glacier water and their flow is

maintained throughout the year. For example according to government of India official population data in India there are around 300 million people depend on river Ganges for agricultural needs and drinking water, which originates from Gangotri glacier and this glacier is major water source for this river, apart from precipitation. In Europe also there are some important rivers that depend on glaciers as a major water source such as Rhine in Germany, River Po in Italy, Rhône in Switzerland and France to name a few. So it's important to monitor the glaciers in the European alps since they play a very important role to maintain the flow the major European Rivers. But its also important to monitor the glaciers which acts as a water source for small rivers such as River Toce because the people living around this river valley will become marginalized in discussion of climate change since this is not a major river in Italy like River po. The Toce is a river in Piedmont, Italy, which stretches the length of the Val d'Ossola from the Swiss border to Lake Maggiore into which it debouches near Fondotoce in the commune of Verbania. The river is 83.6 km long. Belvedere Glacier gives birth to the Anza, a tributary of the Toce River, the Anza is a 35-kilometre Alpine torrent of the Ossola in northern Italy. It flows from the glaciers of Monte Rosa through the Valle Anzasca and into the river Toce, of which it is a right tributary.

The main motivation of this glacier study in terms of human perceptive is, what happens to the community of the people who are depending on the snow for their daily water needs and winter touristic activities such as skiing, snowboarding as their main source of the income for most part of the year. As an engineer I believe that climate crisis is the most important crisis faced by mankind in this 21 century. I want to help communities to understand what's the situation is they are facing, how dangerous and catastrophic it would become if our governments doesn't make strategic investments in the technologies and policies, which will help to fight this climate crisis. I'm not mentioning what technologies they should invest because that is a story for another thesis not this one. So, my goal is to help people through my scientific work help them understand that climate crisis is an important issue which should be included in the people agenda apart from economy, corruption, religion etc while electing the governments in their respective countries. I would also like to mention one American documentary film maker James Balog who inspired me and created an awareness in me how important snow and ice through documentary chasing ice. I would encourage everyone to see that film because we can see how huge polar icebergs and glaciers are melting and retreating respectively in our polar regions if you compare those glaciers to our case study belvedere glacier, which is discussed in chapter 6, our study area is minuscule in size, and we don't even stand a chance in front of

nature. So, I have raised an important question should we be worried that glaciers as melting? yes, can we navigate this climate crisis with minimum damage? absolutely yes, if all the stake holders are working as a community for their future generation survival still. So, I think we still have hope to avoid the catastrophe which IPCC(Intergovernmental panel for Climate Change) report by United Nations describes about when we breach the 2°C.

Due to climate change the temperatures are rising rapidly in the past decade and snow and ice are very sensitive for the temperature. The Italian glaciological committee reports more than 700 glaciers in Italy out of which 200 have disappeared since 1895.Now imagine if all the glaciers have disappeared then we will not have sufficient water for Po River valley or other rivers in northern Italy. This may look like a doom's day scenario. But this will happen in future for sure we will breach the 2°C threshold temperature rise which was set according to Paris Climate Accords 2016.Due to various reasons such as human activity, Air pollution, Carbon emissions etc. The natural water cycle of the rivers are disrupted. So, to know how much volume of water is available at the end of each glacier period for each year, in our case it is during August-September we should have an understanding how fast the glacier is disappearing in terms of volume lost at the end of the glacier period. So, to calculate volume of the glacier lost we first need to generate the DEM (Digital elevation model) for the glacier at different time intervals to have a multitemporal view of understanding how fast the glacier is melting. Now here comes the important question how we can generate a DEM for a glacier at different time intervals. The only option we have is to look for a repository of old satellite images which are available in online. But since commercial satellite data is expensive and not easy to obtain, I have to compromise to use available open-source data which is easily downloadable for any region of interest for the whole world, and it is free to use for non-commercial purposes. Since I have chosen open-source satellite data for the analysis the quality of DEM has to be validated before we use it to use to calculate volume of the glacier lost and the calculated volume loss of glacier can be try related to the discharge of Anza tributary of belvedere glacier which can be modelled using hydrological modelling.

The focus of this thesis is to have a remote sensing and hydrological point of view, about volume of the belvedere glacier lost from August 2003 between August 2019.To achieve this goal we are looking at different techniques such as InSAR and stereoscopic imaging and which can be used reconstruct the Belvedere glacier DEM using different open-source satellite data from Sentinel-1 and Spot-5 satellites and comparing this with the results that can be obtained by a hydrological model using temperature and precipitation and discharge data from gauge stations near the and around glacier to do this we have to prepare a catchment of and calibrate the catchment and vegetation zone parameters for the study area we are interested in and then use them for hydrological modelling.

The thesis is subdivided into 10 chapters. The first chapter explains the importance of glaciers as a water source, why it is important to monitor them and why humans should be concerned about the climate change. Chapter 2 deals with the impact of climate change on glaciers what are the factors affecting them, and what strategies can be adopted for monitoring the glaciers While chapter 3 deals with various Earth Observational technologies from various space agencies and what are the available remote sensing data that can be used to monitor glaciers and Interferometric synthetic aperture radar(InSAR) technique which is used to generate DEM. Chapter 4 describes about the various types of hydrological models available and the model which suits our study area which in our can case HBV(Hydrologiska Byråns Vattenbalansavdelning) model, whereas chapter 5 describes the technique which can be used to generate DEM from a high resolution optical scenes from a satellite and chapter 6 describes the study area which we are interested in and different types of data that was used for data processing to achieve our goal in this thesis . Chapter 7 deals with processing of spot 5 images in Metashape and the processing of sentinel 1 radar images in Sentinel Application platform (SNAP) and obtained results.

Chapter 8 deals with the HBV model stimulation for the timeseries 2003-2009 data of both meteorological and hydrological parameters. Chapter 9 describes the validation of results obtained in chapter 7,8 and final chapter 10 concludes with the challenges and comments on the results that have been obtained during the analysis of the belvedere glacier.

Chapter 2

The problem of Glacier and climate change and strategies adopted for monitoring the Glaciers.

2.1 Introduction

High mountain regions share common features, including rugged terrain, a low-temperature climate regime, steep slopes and institutional and spatial remoteness. These features are often linked to physical and social-ecological processes that, although not unique to mountain regions, typify many of the special aspects of these regions. Due to their higher elevation compared with the surrounding landscape, mountains often feature cryosphere components, such as glaciers, snow cover and permafrost, with a significant influence on surrounding lowland areas even far from the mountains [1]. Hence the mountain cryosphere plays a major role in large parts of the world. This chapter is in line with latest report published by Intergovernmental Panel on Climate Change (IPCC) assesses recent and projected changes in glaciers, snow cover and permafrost in high mountain areas, their drivers, as well as their impact on the different services provided by the cryosphere and related adaptation.

This chapter uses IPCC calibrated language for the communication of confidence in the assessment process [3]. Calibrated language is designed to consistently evaluate and communicate uncertainties that arise from incomplete knowledge due to a lack of information, or from disagreement about what is known or even knowable. The IPCC calibrated language uses qualitative expressions of confidence based on the robustness of evidence for a finding, and (where possible) uses quantitative expressions to describe the likelihood of a finding.

Qualitative expressions (confidence scale) describe the validity of a finding based on the type, amount, quality and consistency of evidence, and the degree of agreement between different lines of evidence as shown in Figure 2.1. Evidence includes all knowledge sources, including Indigenous knowledge and Local Knowledge where available. Very high and high confidence findings are those that are supported by multiple lines of robust evidence with high agreement. Low or very low confidence describe findings for which there is limited evidence and/or low agreement among different lines of evidence and are only presented in chapter if they address a major topic of concern.
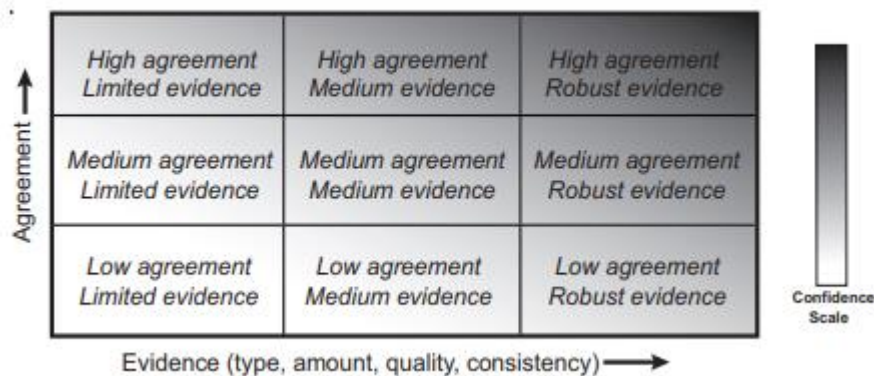
Figure 2.1: A depiction of evidence and agreement statements and their relationship to confidence. Confidence increases towards the top-right corner as suggested by the increasing strength of shading. Generally, evidence is most robust when there are multiple, consistent independent lines of high-quality evidence.

Quantitative expressions (likelihood scale) are used when sufficient data and confidence exists for findings to be assigned a quantitative or probabilistic estimate (Table 2.1). In the scientific literature, a finding is often said to be significant if it has a likelihood exceeding 95% confidence. Using calibrated IPCC language, this level of statistical confidence would be termed extremely likely. Lower levels of likelihood than those derived numerically can be assigned by expert judgement to consider structural or measurement uncertainties within the products or data used to determine the probabilistic estimates (e.g., refer to IPCC AR6 report Table CB1.1). Likelihood statements may be used to describe how climate changes relate to the ends of distribution functions, such as in detection and attribution studies that assess the likelihood that an observed climate change or event is different to a reference climate state.

.

Term	Likelihood of the Outcome
Virtually certain	99-100% probability
Very likely	90-100% probability
Likely	66-100% probability
About as likely as not	33 to 66% probability
Unlikely	0-33% probability
Very unlikely	0-10% probability
Exceptionally unlikely	0-1% probability

Table 2.1 Likelihood Scale

The glacier areas considered in this chapter, including all glacier regions in the world except those in Antarctica, Greenland, the Canadian and Russian Arctic, and Svalbard (since our study area is a mountain glacier see chapter 6) include ~170,000 glaciers covering an area of ~250,000 km2 (4) with a total ice volume of 87 ± 15 mm sea level equivalent [5]. These glaciers span an elevation range from sea level, for example in south-east Alaska, to >8,000 m a.s.l(above the sea level), in the Himalaya and Karakoram, and occupy diverse climatic regions. Their mass budget is determined largely by the balance between snow accumulation and melt at the glacier surface, driven primarily by atmospheric conditions. Rapid changes in mountain glaciers have multiple impacts for social-ecological systems, affecting not only biophysical properties such as runoff volume and sediment fluxes in glacier-fed rivers, glacier related

hazards, and global sea level (Chapter 4) but also ecosystems and human livelihoods, socioeconomic activities, and sectors such as agriculture and tourism, as well as other intrinsic assets such as cultural values. While glaciers worldwide have experienced considerable fluctuations throughout the Holocene driven by multidecadal variations of solar and volcanic activity, and changes in atmospheric circulation [6]. This section focuses on observed glacier changes during recent decades. Satellite and in situ observations of changes in glacier area, length and mass show a globally largely coherent picture of mountain glacier recession in the last decades [7], although annual variability and regional differences are large (very high confidence). The global trend is statistically significant despite considerable interannual and regional variations [8]. Since previous IPCC report AR5's global 2003–2009 estimate[9] several new estimates of global-scale glacier mass budgets have emerged using largely improved data coverage and methods. These estimates combined with available regional estimates (refer to IPCC report Table 2.A.1) indicate that the glacier mass budget of all mountain regions (excluding Antarctica, Greenland, the Canadian and Russian Arctic, and Svalbard) was very likely -490 ± 100 kg m–2 yr–1 (-123 ± 24 Gt yr–1) during the period 2006–2015 with most negative averages (less than -850 kg m–2 yr–1) in the Southern Andes, Caucasus/ Middle East, European Alps and Pyrenees. It is very likely that atmospheric warming is the primary driver for the global glacier recession [10]. There is limited evidence (high agreement) that human-induced increases in greenhouse gases have contributed to the observed mass changes [11]. It was estimated that the anthropogenic fraction of mass loss of all glaciers outside Greenland and Antarctica increased from 25 ± 35% during 1851–2010 to 69 ± 24% during 1991–2010 [12].

Other factors, such as changes in meteorological variables other than air temperature or internal glacier dynamics, have modified the temperature-induced glacier response in some regions (high confidence). For example, glacier mass loss over the last seven decades on a glacier in the European Alps was intensified by higher air moisture leading to increased longwave irradiance and reduced sublimation [13]. Changes in air moisture have also been found to play a significant role in past glacier mass changes in eastern Africa [14], while an increase in shortwave radiation due to reduced cloud cover contributed to an acceleration in glacier recession in the Caucasus [15].

2.2 Impacts and Risks of Glacier melt due to climate change.

There is a vast impact on the environment due to melting of glaciers due to climate change. The scope of this thesis is limited to hydrological impact and risks of Glacier melt so in the below section only that topics has been discussed but to have clear overview of this impacts and risk of the glacier melt due to climate change please refer to IPCC lastest report (chapter 2 section 2.3).

- **Changes in River Runoff.**

The mountain cryosphere is an important source of freshwater in the mountains themselves and in downstream regions. The runoff per unit area generated in mountains is on average approximately twice as high as in lowlands [16] making mountains a significant source of fresh water in sustaining ecosystem and supporting livelihoods in and far beyond the mountain ranges themselves. The presence of snow, glaciers, and permafrost generally exert a strong control on the amount, timing, and biogeochemical properties of runoff. Changes to the cryosphere due to climate change can alter freshwater availability with direct consequences for human populations and ecosystems.

Glaciers supply water that supports human communities both close to the glacier and far away from the glacier, for example for agriculture or drinking water. Rising temperatures cause mountain glaciers to melt and change the water availability. At first, as the glacier melts, more water runs downhill away from the glacier. However, as the glacier shrinks, the water supply will diminish and farms, villages and cities might lose a valuable water source. Melting glaciers can affect river runoff, and thus freshwater resources available to human communities, not only close to the glacier but also far from mountain areas. As glaciers shrink in response to a warmer climate, water is released from long-term glacial storage. At first, glacier runoff increases because the glacier melts faster, and more water flows downhill from the glacier. However, there will be a turning point after several years or decades, often called 'peak water', after which glacier runoff and hence its contribution to river flow downstream will decline. Peak water runoff from glaciers can exceed the amount of initial yearly runoff by 50% or more. This excess water can be used in different ways, such as for hydropower or irrigation. After the turning point, this additional water decreases steadily as the glacier continues to shrink, and eventually stops when the glacier has disappeared, or retreated to higher elevations where it is still cold enough for the glacier to survive. As a result, communities downstream lose this

valuable additional source of water. Total amounts of river runoff will then depend mainly on rainfall, snowmelt, ground water and evaporation.

Furthermore, glacier decline can change the timing in the year and day when the most water is available in rivers that collect water from glaciers. In mid- or high latitudes, glacier runoff is greatest in the summer, when the glacier ice continues to melt after the winter snow has disappeared, and greatest during the day when air temperature and solar radiation are at their highest. As peak water occurs, more intense glacier melt rates also increase these daily runoff maxima significantly. In tropical areas, such as parts of the Andes, seasonal air temperature variations are small, and alternating wet and dry seasons are the main control on the amount and timing of glacier runoff throughout the year.

The effects of glaciers on river runoff further downhill depend on the distance from the glacier. Close to the glaciers (e.g., within several kilometres), initial increases in yearly glacier runoff until peak water followed by decreases can affect water supply considerably, and larger peaks in daily runoff from the glaciers can cause floods. Further away from the glaciers the impact of glacier shrinkage on total river runoff tends to become small or negligible. However, the melt water from glaciers in the mountains can be an important source of water in hot and dry years or seasons when river runoff would otherwise be low, and thereby also reducing variability in total river runoff from year to year, even hundreds of kilometres away from the glaciers. Other components of the water cycle such as rainfall, evaporation, groundwater, and snowmelt can compensate or strengthen the effects of changes in glacier runoff as the climate changes.

According to the fifth IPCC report (AR5) there is a increase in winter flows and a shift in timing towards earlier spring snowmelt runoff peaks during previous decades (robust evidence, high agreement). In glacier-fed river basins, it was projected that melt water yields from glaciers will increase for decades in many regions but then decline (very high confidence). These findings have been further supported and refined by a wealth of new studies since AR5.

Recent studies indicate considerable changes in the seasonality of runoff in snow and glacier dominated river basins (very high confidence; refer to chapter 2 last IPCC report Table SM2.9). Several studies have reported an increase in average winter runoff over the past decades, for example in Western Canada [17], the European Alps [18,19] and Norway [20], due to more precipitation falling as rain under warmer conditions. Summer runoff has been observed to decrease in basins, for example in Western Canada (Brahney et al., 2017) and the European

Alps (Bocchiola, 2014), but to increase in several basins in High Mountain Asia [21;22;23]. Both increases, for example, in Alaska [24] and the Tian Shan Mountain ranges (25), and decreases, for example, in Western Canada [26] have also been found for average annual runoff. In Western Austria, detected an increase in annual flow at high elevations and a decrease at low elevations between 1980–2010[27].

In addition to changes in ice and snow melt, changes in other variables such as precipitation and evapotranspiration due to atmospheric warming or vegetation change affect runoff amounts and timing (19). Changes in melt water from ice and snow often dominates the runoff response to climate change at higher elevations, while changes in precipitation and evapotranspiration become increasingly important at lower elevations [27]. Permafrost thaw may affect runoff by releasing water from ground ice (28) and indirectly by changing hydrological pathways or ground water recharge as permafrost degrades [29]. The relative importance of runoff from thawing permafrost compared to runoff from melting glaciers is expected to be greatest in arid areas where permafrost tends to be more abundant [30]. Because glaciers react more rapidly to climate change than permafrost, runoff in some mountain landscapes may become increasingly affected by permafrost thaw in the future (28). In summary, there is very high confidence that glacier and snow cover decline have affected and will continue to change the amounts and seasonality of river runoff in many snow-dominated and/or glacier-fed river basins.

- **Landslide, Avalanche and Flood Hazards**

High mountains are particularly prone to hazards related to snow, ice and permafrost as these elements exert key controls on mountain slope stability [31]. Hazards assessed in this section range from localised effects on mountain slopes and adjacent valley floors (distance reach of up to several kilometres) to events reaching far into major valleys and even surrounding lowlands (reach of tens to hundreds of kilometres) and include cascading events. Changes in the cryosphere due to climate change influence the frequency and magnitude of hazards, the processes involved, and the locations exposed to the hazards. Natural hazards and associated disasters are sporadic by nature, and vulnerability and exposure exhibit strong geographic variations. Assessments of change are based not only on direct evidence, but also on laboratory experiments, theoretical considerations and calculations, and numerical modelling.

Permafrost degradation and thaw as well as increased water flow into frozen slopes can increase the rate of movement of frozen debris bodies and lower their surface due to loss of ground ice (subsidence). Such processes affected engineered structures such as buildings,

hazard protection structures, roads, or rail lines in all high mountains during recent decades. Movement of frozen slopes and ground subsidence/heave are strongly related to ground temperature, ice content, and water input [31]. Where massive ground ice gets exposed, retrogressive thaw erosion develops [32]. The creep of rock glaciers (frozen debris tongues that slowly deform under gravity) is in principle expected to accelerate in response to rising ground temperatures, until substantial volumetric ice contents have melted out [33;34]. As documented for instance for sites in the European Alps and Scandinavia for recent years to decades, rock glaciers replenished debris flow starting zones at their fronts, so that the intensified material supply associated with accelerated movement contributed to increased debris flow activity (higher frequency, larger magnitudes) or slope destabilisation [35;36].

There is high confidence that the frequency of rocks detaching and falling from steep slopes (rock fall) has increased within zones of degrading permafrost over the past half-century, for instance in high mountains in North America, New Zealand, and Europe [37;38; 39]. Ice break-off and subsequent ice avalanches are natural processes at steep glacier fronts. How climate driven changes in geometry and thermal regime of such glaciers influenced ice avalanche hazards over years to decades depended strongly on local conditions, as shown for the European Alps [40;41]. The few available observations are insufficient to detect trends. Where steep glaciers are frozen to bedrock, there is, however, medium evidence and high agreement from observations in the European Alps and from numerical simulations that failures of large parts of these glaciers were and will be facilitated in the future due to an increase in basal ice temperature (40; 41).

Snow avalanches can occur either spontaneously due to meteorological factors such as loading by snowfall or liquid water infiltration following, for example, surface melt or rain-on-snow, or can be triggered by the passage of people in avalanche terrain, the impact of falling ice or rocks, or by explosives used for avalanche control [42]. There is no published evidence found that addresses the links between climate change and accidental avalanches triggered by recreationists or workers. Changes in snow cover characteristics are expected to induce changes in spontaneous avalanche activity including changes in friction and flow regime [43;44].

Glacier-related floods, including floods from lake outbursts (GLOFs), are documented for most glacierised mountain ranges and are among the most far-reaching glacier hazards. Past events affected areas tens to hundreds of kilometres downstream [45]. Retreating glaciers produced lakes at their fronts in many high mountain regions in recent decades [46; 47; 48]. Lake systems

in High Mountain Asia also often developed on the surface of down wasting, low-slope glaciers where they coalesced from temporally variable supraglacial lakes [49;50]. Corroborating SREX(Special Report on Managing the Risks of Extreme Events and Disasters to Advance Climate Change Adaptation by United nations) and AR5 findings, there is high confidence that current global glacier shrinkage caused new lakes to form and existing lakes to grow in most regions, for instance in South America, High mountain Asia and Europe [48;51;52;53]. Exceptions occurred and are expected to occur in the future for few lakes where evaporation, runoff and reduced melt water influx in total led to a negative water balance [54]. Also, advancing glaciers temporarily dammed rivers, lake sections, or fjords [55], for instance through surging [56], causing particularly large floods once the ice dams breached. Outbursts from water bodies in and under glaciers can cause floods like those from surface lakes but little is known about the processes involved and any trends under climate change.

2.3 GLACIER MONITORING STRATAGIES

- **Calculating Annual Glacier Mass Balance**

The annual mass balance of a glacier is a hydrologic budget measuring the difference between the amounts of accumulation and ablation experienced by a glacier during the hydrologic year [57]. Depending on the quantity of annual accumulation and ablation; the mass balance value may be positive, negative, or zero. Glacier mass balance is a good measure of the general health of a glacier. A positive mass balance indicates mass accumulation, and that the glacier is growing; conversely, a negative balance indicates that the glacier is shrinking. A glacier with a mass balance of zero is in a steady-state and has a constant volume.

Beginning in the 1870s in the Swiss Alps, glacier mass balance monitoring has been used extensively to quantify and assess glacier changes [58; 59]. Glacier mass balance monitoring is well accepted by the glaciological community as the most direct measure of glacier health. Mass change is directly linked to changes in glacier volume, climate, and glacial runoff. North Cascades National Park in Washington selected mass balance monitoring as the primary indicator of glacier change in their long-term glacier monitoring plan for the following reasons: "First, it accounts for approximately 90% of the annual change in volume of temperate glaciers. Second, it can readily be measured on the only accessible part of a glacier—its surface" [60].

Climatic changes can be inferred from temporal trends of mass balance dynamics because changes in glacier mass balance are highly correlated to variations in temperature and precipitation [61]. Trends of positive mass balance over time generally relate to increased

24

precipitation (increased accumulation) or decreased temperature (reduced ablation); and the opposite is typically true for negative mass balance. Monitoring glacier mass balance can provide a seasonal measure of water accumulation, storage, and loss, which is useful for extrapolation to the greater population of glaciers in the region [60].

Equilibrium Line Altitude and Accumulation-Area Ratio

It is well established that the equilibrium line altitude (ELA) (altitude on a glacier where annual accumulation equals annual ablation) at the end of the ablation season is directly related to the annual mass balance of the glacier [62]. If annual mass balance increases, the ELA will be located at a lower elevation. Conversely, an unusually high ELA indicates a decrease in annual mass balance. Figure 2.2 shows the position of the ELA on an unnamed cirque glacier in Denali National Park and Preserve in Alaska. If the area above or below the ELA and the total glacier area are known, an

accumulation area ratio (AAR) can be calculated. The AAR is determined by dividing the glacier's accumulation area by the total glacier area (62). Monitoring annual variations in the ELA and AAR of a glacier provides a good estimate of changes in mass balance and variations in climate. There are a variety of acceptable methods for determining ELA, including repeat photography, direct survey with a GNSS receiver, and satellite or aerial imagery.

Figure 2.2 Equilibrium line on an unnamed glacier in Denali National Park and Preserve,USA. Photo: R.D. Karpilo Jr., 2004.

Repeat photography methodology for monitoring the ELA and AAR consists of photo site selection and establishment, photography, ELA plotting, and AAR calculation. The two options for selecting a photo site are to establish a new site or to reoccupy the site of an historic photograph. Reoccupying a previous photo location is preferable if a quality historic photograph of the glacier exists and was taken from an acceptable location. The following criteria should be considered when evaluating a potential photo site: current and future view of the equilibrium line, accessibility, repeatability, and potential hazards. The photo site can be permanently established by installing a fence post, reinforcing bar (rebar) stake, or expansion bolt and washer, or by selecting a suitable natural feature, such as a boulder, as a marker. The position of the site marker is recorded with a GNSS receiver and marked on a map. The photo site is photographed, and a written description of the location is recorded to assist in relocating the site in the future. The tripod and camera is positioned at the marked location and several images with bracketed exposures are captured. A field notebook is used to record the photo direction, tripod height, lens focal length, camera data, exposure number, date and time, weather conditions, and other observations. For detailed information about photographic monitoring field methods and techniques see Hall (2002), Jorgenson et al. (2006), and National Park Service (2006). The photographs are used to visually estimate and plot the ELA position

on a map or to digitize it using geographic information systems (GIS) software. If a digital elevation model (DEM) of the glacier and surrounding area is available, the oblique photographs can be georeferenced to the DEM and the ELA and area of the glacier can be precisely digitized using GIS software. See Corripio (2004) for detailed instructions for georeferencing oblique photographs to DEMs. If the total glacier area is available, the ELA is used to determine the area of the accumulation zone. The AAR is calculated by dividing the accumulation area by the total glacier area. Repeat photography visits should be conducted on days with favourable weather and high visibility and coincide with the late-summer end of the ablation season when the maximum area of snow-free ice is exposed [67]. In order to produce a data, set useful for identifying mass balance trends, monitoring and mapping of the ELA should occur on an annual basis.

The primary limitation of this method is that it is an approximation of glacier mass balance. The actual relationship of AAR to mass balance differs from glacier to glacier. Also, it assumes that the snowline is the equilibrium line. While this assumption is fairly accurate for most temperate glaciers, at higher elevations and latitudes the effect of internal refreezing of meltwater at the base of the season snowpack becomes important. In this situation, the refrozen meltwater looks like ice or firn (recrystallized and partially compacted snow from previous seasons) rather than seasonal snow, and the estimated ELA is mistakenly plotted too high on the glacier [62]. This error has never been quantified. Poor topographic map accuracy of the glacier may contribute to errors in plotting the ELA location. This concern is important because most topographic maps are decades old, despite revision dates, and given the general recession of most glaciers they are no longer accurate. Lastly, timing is a limitation because it is important to perform the monitoring near the end of the ablation season, before the first snowfall. While ELA and AAR do not provide estimates of mass change, unless other site-specific information is available, they are good indicators of variations in glacier mass balance and climatic conditions [64;65]. If annual mass balance increases, the ELA will be located at a lower elevation and the AAR will be larger, and vice versa. A "typical" alpine glacier with a mass balance of zero will have an AAR value between 0.5 [65] and 0.7 [62]. If mass balance measurements are available, a relationship between ELA and mass balance can be established, and the mass balance measurements can be terminated. However, the glacier cannot change geometry (area-altitude) significantly; otherwise the relation between the two variables will change.

Glaciological Mass Balance

The glaciological method is the most widely used technique for monitoring glacier mass balance [66]. Direct measurement of glacier mass balance components provides the most detailed information about the processes that control mass balance, spatial differences, and changes over time [67]. Mass balance for the entire glacier is determined based on repeated a number of point

measurements on the glacier surface [62]. The depth of snow or ice that has accumulated or ablated at each point is measured and multiplied by the snow or ice density to determine the mass balance at that point [68]. The point values are interpolated and extrapolated across the glacier surface to calculate the mass balance for the entire glacier. Most commonly, point locations of mass balance are measured against poles drilled into the glacier surface. An ideal network consists of ablation poles (or stakes) installed in a pattern covering the entire glacier. In many cases, logistical constraints dictate that the stakes are installed along the centreline of the glacier with occasional transverse profiles perpendicular to the longitudinal profile of the glacier. Stakes should be distributed by equal elevation intervals, not equal horizontal distances [68]. The location of each stake must be recorded using a GNSS receiver). Ablation stakes of PVC pipe, wood, aluminium, steel, plastic, and bamboo have all been used successfully for mass balance investigations [67;69]. An aluminum ablation stake is visible in

Figure 2.3**.** Stakes are installed on the glacier by drilling holes 2–4 cm in diameter and up to 10 m in depth with a steam drill or hand auger [60].

Figure 2.3 A monitoring technician measures the length of ablation stake exposed on the East Fork Toklat Glacier in Denali National Park and Preserve, Alaska. Photo: R.D Karpilo Jr., 2003.

The network of ablation stakes is used in conjunction with snow pits to determine the depth of snow or ice that has melted or accumulated at each measurement location on the glacier [68]. Ablation determinations are made by measuring the length of exposed stakes with a tape measure at the beginning and end of the mass balance year. The stakes can be used to measure accumulation if the depth of new snow does not exceed the length of exposed stakes. This is often not possible because in many areas deep snow accumulations bend or break installed stakes; therefore, snow accumulation depths must be determined using snow pits or snow-depth probes [68; 60]. The density of the snow is determined using a snow density tube and a scale [68]. The mass change at each ablation site is calculated by multiplying the change in length of the exposed stakes at the end of the mass balance season by the density of the snow or ice. The density of snow needs to be determined in the field. See Riedel and Burrows (2005) for detailed field methods for measuring snow density. Glacier ice is assumed to have a density of 900 kg m–3 [62]. The mass gained or lost at each stake location is calculated and extrapolated across the entire glacier surface to determined total mass balance. The interpolation/extrapolation of the point data varies according to glacier conditions and the person making the evaluation. A GIS method is presented by Riedel and Burrows (2005) and the contour method is explained by Kaser et al. (2003). At a minimum, mass balance field visits should be conducted biannually—one visit at the end of the accumulation season and one at the end of the ablation season [68]. This schedule allows direct measurement of the magnitude of seasonal accumulation and ablation [67]. Additional visits may be required to inspect and maintain/replace ablation stakes, particularly in regions where ice melt exceeds several meters per summer [68]. The glaciological method is an excellent technique for assessing glacier mass

balance; but it does have several inherent limitations. One potential limitation is that this method does not account for ablation due to calving [69]. Mass balance calculations on calving glaciers require the monitoring of the terminus position and glacier velocity to determine calving rates. A second limitation is that the glaciological method only measures ablation on the glacier surface. Approximately 90% of ablation occurs on the glacier surface; thus it is assumed that the subsurface change is negligible and can be ignored in the calculations [60]. The third limitation is that crevasses or steep terrain may not allow installation of stakes in a desired arrangement. Other complications include field visits under adverse weather conditions, complicated and expensive logistics and labor, and the slow rate of data acquisition [68]. The glaciological method is the most accurate surface-based method to date and provides highly detailed information on the spatial variation of mass balance magnitudes. Monitoring glacier mass balance provides insights into the hydrologic cycle of the glacier and allows a comprehensive evaluation of glacier dynamics.

Geodetic Mass Balance

Geodetic mass balance is determined by calculating an ice mass's volumetric change through time from repeated topographic surveys of surface elevation and extent [62]. This technique offers a remote-sensing alternative or complement to the field-based glaciological method. There are several acceptable methods for determining the geodetic mass balance of a glacier, including the use topographic maps, DEMs based on satellite or aerial imagery, and light detection and ranging (LiDAR) surveys [68].

The geodetic method is an effective technique for remotely assessing glacier volume change, but it does have several inherent limitations. The primary limitation of this method is the high cost of obtaining geodetic-quality aerial imagery [60].The second limitation is the potential error derived from assuming "the density of the material gained or lost is equal to the density of ice" [70]. This assumption may result in overestimating the mass of snow and firn in the accumulation area. Other complications include errors from areas of limited photographic contrast (including icefields with limited relief), and poor DEM registration, typical of the snow-covered accumulation zones [71;72;73].

It is important to note the difference between this method and the glaciological method because the products can be confused. The geodetic method produces a volume change for the entire glacier, which after some assumptions about density, is converted to mass change. This method provides an important check on the glaciologic method and should be used in conjunction with

it. The geodetic method does not provide point-specific mass balance data, such as annual mass balance up a centerline. For example, a glacier in equilibrium will show zero volume change and zero elevation change up the centerline. In contrast, the glaciological method will show increasingly negative mass balance down glacier from the equilibrium line and increasingly positive mass balance up glacier. The sum of the glaciologic mass balance along the centerline would be zero. The difference in results from the geodetic and glaciologic methods is because the geodetic method measures the geometric response to changes in mass input and output, whereas the glaciologic method measures the actual input and output. he greatest utility of the geodetic mass balance method is in calculating average balances over long periods of time and in validating the glaciological cumulative mass balance [66]. This technique can be used to extend the mass balance record into the past by applying the methodology to historic aerial photography and topographic maps.

- **Glacier Terminus Position**

The glacier terminus position is defined as the physical position of the snout of the glacier [66]. Figure 2.4 shows the terminus of La Perouse Glacier in Glacier Bay National Park and Preserve, Alaska. In non-calving glaciers, the glacier terminus continually adjusts to variations in mass balance by advancing or retreating; and is useful in validating mass balance measurements [66;67] Glacial extent is a critical indicator of climate change; therefore, monitoring changes in terminus position provides useful data for understanding the impact of climate change on water resources and ecosystem evolution [67;68;75]. Additionally, past terminus positions can be reconstructed from historic photographs and terminal or recessional moraines to understand changes in past climate (68; 76;77;78).

Figure 2.4 The terminus of La Perouse Glacier on the outer coast of Glacier Bay National Park and Preserve, Alaska. Photo: R.D. Karpilo Jr., 2003

Vertical aerial photographs and satellite images are a highly efficient tool for documenting changes of glacier terminus positions [67]. Remote-sensing techniques allow the monitoring of many glaciers without the effort associated with field-based techniques. Additionally, historic aerial photos or satellites images of glaciers are often available, extending the terminus monitoring record into the past. Historical sequences of images provide a visual representation of glacier change over time and are useful for communicating glacier change to diverse audiences. Glacier terminus positions can be digitized from georeferenced images using a GIS. The digitized terminus positions are then used to quantify changes in glacier length and area. Vertical aerial photography and satellite imagery with ground control "provides a quantitative base for accurate mapping of surface features" [89]. The methodology consists of image acquisition, image scanning and georeferencing, and glacier terminus digitizing. Images are obtained through vendors or appropriate government agencies specializing in aerial photography or satellite imagery (examples include Landsat, ASTER, or SPOT-5). The acquired images must be of sufficient resolution to discern glacier margins from the surrounding terrain and must be taken late in the ablation season [60]. The purchased images should be georeferenced and delivered in a GIS-compatible digital format. Once the images are loaded into the GIS, the spatial position of the glacier terminus is recorded using manual, on-screen digitizing techniques [60]. Interpretations from this monitoring technique require the comparison of a minimum of two mapped terminus positions. If no historical aerial imagery

exists, the first digitized data set will establish a baseline for future comparison and may be useful for comparisons with historic terminus positions derived from terminal moraines. The use of the GIS for data analysis facilitates the comparison of the mapped terminus positions and aids in the quantification of glacier change by calculating changes in glacier length and estimating changes of glacier area. This method allows the efficient monitoring of future glacier change over large areas and the ability to systematically integrate historic imagery to identify past trends.

3.Glacier Area

Monitoring changes in glacier area is important because it generally provides a direct measure of glacier advance and retreat and the associated creation or destruction of terrestrial and aquatic habitats[60]. Measuring the surface area of a glacier is critical for calculating glacier mass balance, identifying the location of the ELA, and calculating accumulation-area ratios. Monitoring changes in glacier area provides an indicator linking the response of glacier length to changes in mass balance [68]. Documenting long-term trends of glacier area change provides a good index for understanding local climatic changes. Vertical aerial photographs and satellite images are a highly efficient tool for documenting changes of glacier area [67]. Remote-sensing techniques allow the monitoring of a large number of glaciers without the effort associated with field-based techniques. Historical sequences of images provide a visual representation of glacier change over time and are useful for communicating glacier change to diverse audiences. Glacier areas can be digitized from georeferenced images using a GIS. The first set of digitized areas can be compared to measurements from subsequent years to identify trends and quantify rates of changes in glacier length and area. The primary limitation of this method is the high cost of obtaining large-scale satellite or aerial imagery [79]. Aerial imagery of mountainous environments often contains shadowed areas that may conceal glacial margins, making it difficult to interpret the glacial boundary. Debris-covered glaciers pose a substantial challenge for mapping, as it can be difficult to discern debris-covered ice from the surrounding terrain. Additionally, it is important to define where the stagnant ice ends and the active ice terminus begins. It is important that the satellite or aerial photography survey occur late in the ablation season before the first snowfall of winter. terpretations from this monitoring technique require the comparison of a minimum of two mapped glacier areas. If no historical aerial imagery exists, the first digitized data set season will establish a baseline for future comparison. The use of the GIS for data analysis facilitates the comparison of the mapped areas and allows the

quantification of glacier change by calculating changes in glacier length and area. The greatest utility of this method is the ability to identify quantifiable trends and rates of glacier change.

4.Glacier Surface Velocity

Glacier surface velocity is a measure of the rate at which a glacier is moving downhill under the influence of gravity, through the processes of sliding on its bed and internal deformation of the ice[66]. Generalized, singular velocities are often presented for entire glaciers, but it is wrong to imagine the motion of the glacier to be like that of a train, uniformly descending a mountain pass. On the contrary, the nature of glacier movement is temporally and spatially variable. Glacier movement is analogous to the internal motion of water in a river; in which the friction of the bed and the banks reduces the water velocity relative to the faster, unimpeded water near the surface centreline of the main channel. Glaciers typically behave in a similar fashion; the velocity of a glacier is greatest at the surface along the centerline and least near the valley walls and floor, where flow is inhibited by friction [66]. Changes in gradient along the glacier profile results in variable flow velocities. Steep gradients, such as those found at icefalls, yield the highest flow rates. Typical valley glaciers have surface velocities ranging from 10 to 200 m yr–1 for most of their length, while icefalls may have rates as high as 1 or 2 km yr–1 [66]. During the quiescent phase, surging glaciers may have a velocity consistent with non-surging glaciers (10–200 m yr–1) until interrupted by short periods of rapid advance. Rates of up to 100 m d–1 were observed during the 1993 surge of Bering Glacier in Alaska[81]. Glacier movement is seasonal, with the highest flow velocities coinciding with warmer ice temperatures and increased presence of basal meltwater during the summer [57]. A few glaciers exhibit summer velocities that are twice as fast as their winter rates [66]. he fact that glaciers move is critical to the hydrologic cycle, the functioning of the ocean/atmospheric system, and to all geological and geomorphological phenomena that arise from glaciation" [57]. Monitoring glacier movement provides an important link between fluctuations in mass balance and the corresponding changes in glacier geometry[67]. The rate of glacier flow determines how quickly mass is redistributed and is an important factor in determining whether the glacier is advancing or retreating [83].

Increases in the climatic variables of temperature and precipitation can affect glacier velocity. An increase in air temperature increases ice temperature, which correspondingly reduces the ice viscosity and increases glacier velocity. Increasing the air temperature increases the volume

of basal meltwater, which reduces basal friction and increases glacier velocity. If precipitation increases, the ice thickness also increases, which can result in increased glacier velocity.

Surveying the position of artificial targets on the surface of a glacier with GNSS is a simple but highly precise method of monitoring glacier surface velocity. This technique requires installing velocity stakes on the glacier surface and repeatedly surveying the position of the stakes using high-precision GNSS receiver. The change in distance of the location of the velocity stake and the known interval of time between surveys can be used to calculate the surface velocity of the glacier at the target location. he methodology for monitoring surface velocity with GNSS surveying consists of velocity stake installation, data collection, post-processing, and velocity calculation. A convenient alternative to installing new stakes specifically for glacier velocity monitoring is to utilize stakes installed for mass balance monitoring[68]. If mass balance stakes are not available, velocity stakes must be installed by drilling a small diameter hole several meters deep with a steam drill or ice auger and inserting the velocity stake. Data collection involves recording a precise location of the velocity stake using a survey-grade GNSS receiver.To maximize precision, the position of the lowest exposed portion of the stake should be used for the measurement [68]. If the GNSS receiver supports real-time differential-correction it should be employed during data collection. After the GNSS data is collected, it is downloaded to a computer and differentially corrected using data collected simultaneously at a GNSS base station. Post-processing the GNSS data mitigates the signal degrading effects of the atmosphere and improves the accuracy of the data. Positional accuracy of differentially corrected data collected with a survey-grade GNSS receiver is generally within a few centimetres [90]. At this point, data should be imported into the GIS for inspection and quality control. After the prescribed interval, the velocity stake must be resurveyed. Calculating the surface velocity requires dividing the change in distance of the velocity stake (calculated using the GIS) by the change in time between surveys. The calculated velocity can be presented on a topographic map as a vector representing the magnitude and direction of the measurement [66]. he primary limitation of ground-based GNSS surveying is that it is highly labor intensive and limited to the accessible portions of the glacier[80]. Surveying enough points to satisfy a complex ice-dynamics investigation is generally time-consuming and expensive. Data collectors should also be aware that poor GNSS signal reception is commonly encountered in narrow valleys and other terrain with a limited view of the sky. Despite the limitations, monitoring glacier surface velocity with GNSS by utilizing

existing mass balance stakes, or installing velocity stakes, provides a good indication of the glacier's dynamic response to changes in mass balance [68].

Tracking the motion of natural targets on a glacier surface using a series of vertical aerial photographs or satellite images is an effective technique for monitoring glacier velocity (69; 67;80]. Remote-sensing techniques facilitate the monitoring of many glaciers without the effort associated with field-based techniques. The displacement of natural features can be calculated from a series of georeferenced images using a GIS. The change in distance of the location of the target in the photo pairs and the known time interval between images can be used to calculate the surface velocity of the glacier at the target location. The use of aerial photographs or satellite images is a proven method for monitoring glacier surface velocity. Interpretations from this monitoring technique require the comparison of images from a minimum of two-time horizons. Historical images may be utilized to determine past surface velocities. If no historical aerial imagery exists, the first digitized data set will establish a baseline for future comparison. "For a long-term program, where the mass and volume of a glacier are expected to change, a coincident data set of flow information is useful for determining the dynamic response of glaciers to changes in mass input [67]. Understanding how a glacier responds to changes in mass balance provides useful insight into how the glacier may respond to future climate changes. The potential limitation is that monitoring is restricted to glaciers with easily identifiable, natural targets, so measurements may be limited to a few sample locations on each glacier and may not be repeatable due to the target traveling down the glacier. Measurements are restricted to the ablation zone because year-round snow covers most potential natural targets in the accumulation zone. Additionally, it is important that the satellite image or aerial photography survey occurs after the spring snowmelt, but before the first snowfall of winter to assure that the targets are visible.

Chapter 3

Earth Observation Technologies

3.1 Introduction

Back in the 19 and till mid of 20 century mostly Aerial photography was used to map the earth surface. The first known aerial photograph was taken in 1858 by French photographer and balloonist, Gaspar Felix Tournachon, also known as "Nadar". In 1855 he had patented the idea of using aerial photographs in mapmaking and surveying, but it took him 3 years of experimenting before he successfully produced the very first aerial photograph. It was a view of the French village of Petit-Becetre taken from a tethered hot-air balloon, 80 meters above the ground. This was no mean feat, given the complexity of the early collodion photographic process, which required a complete darkroom to be carried in the basket of the balloon! Unfortunately, Nadar's earliest photographs no longer survive, and the oldest aerial photograph known to be still in existence is James Wallace Black's image of Boston from a hot-air balloon, taken in 1860 as shown in Fig 3.1. Following the development of the dry-plate process, it was no longer necessary carry so much equipment, and the first free flight balloon photo mission was carried out by Triboulet over Paris in 1879.

Source: Professional Aerial Photographers Association, International

Figure 3.1 (left) Nadar "elevating photography to the condition of art", caricature by Honoré Daunier. Published in Le Boulevard 25th May 1862. (center) Nadar's earliest surviving aerial image, taken above Paris in 1866. (right) Boston from a tethered balloon, 13th October 1860, by James Wallace Black.

Gradually, improvements in photographic technology made it easier to take cameras into the skies. Besides hot air balloons, early pioneers also used kites, pigeons, and rockets to carry their cameras aloft. The English meteorologist E. D. Archibald was among the first to take successful photographs from kites in 1882. He used a string of kites, with the camera being attached to the last. In France, Arthur Batut took an aerial photograph from a kite in 1889, in Labruguiere, France. He suspended his still rather large camera from a single kite and set an automatically timed exposure. A slow burning fuse, responding to a rubber band driven device, triggered the shutter within a few moments of the kite being launched. Batut's first aerial photograph was taken in May 1888.

In California, the devastation of San Francisco after the 1906 earthquake and fire was captured by George R. Lawrence as shown in Figure 3.2, using a camera attached to a string of kites high above the city. His specially designed large-format camera had a curved film plate to provide panoramic images, which remain some of the largest aerial exposures ever taken. The camera, which was large and extremely heavy, took as many as 17 kites to lift it 2,000 feet into the air. Lawrence also used ladders and high towers to capture lower level "aerial" photographs.

Source: Professional Aerial Photographers Association, International

Figure 3.2 (left) Batut's kite, and (center top) his photograph of Labrugiere(right) Lawrence's kites, and (center bottom) one of his panoramas of San Francisco after the earthquake and fire.

The Bavarian Pigeon Corps used their pigeons to carry messages and for aerial reconnaisance. In 1903, Julius Neubranner designed a tiny breast-mounted camera for carrier pigeons. The camera could be set to take automatic exposures at 30-second intervals as the pigeon flew along. The flight path was not always reliable, however! Mostly used for military purposes, the

birds were introduced at the 1909 Dresden International Photographic Exhibition, where postcards of aerial photographsas shown in Figure 3.3 taken above the exhibition were very popular with the public.

Source: Professional Aerial Photographers Association, International

Figure 3.3 (left) Neubranner's pigeon mounted camera (center and right) Aerial photographs taken on pigeon photo flights. Note the wingtips showing in the center top image of the castle.

The first successful aerial photograph as shown Figure 3.4 from a rocket mounted camera was taken by the Swedish inventor, Alfred Nobel in 1897. He is best known now a days for the Nobel prize. In 1906, Albert Maul in Germany, produced a more reliable method by using a rocket propelled by compressed air. His camera took an aerial photograph from a height of 2,600 feet, before being ejected and parachuted back to earth. He had patented the idea of using powder rockets in 1903, and by 1904 was testing gyroscopically stabilised cameras launched by rockets and recovered by parachute. In 1912 he demonstrated his perfected rocket to the Austrian Army, but by then airplanes were found to be more effective.

Figure 3.4 (left) Aerial photograph of the Swedish countryside, taken by Alfred Nobel from a rocket powered camera(right) Albert Maul's rocket, and (center) one of Maul's aerial photographs of the German countryside.

The first aerial photography as shown in Figure 3.5 taken from an airplane was in 1909, by Wilbur Wright. He was in Italy, engaged in marketing planes to the Italian government, when he carried a passenger who took motion pictures of the military field at Centocelli, near Rome.

During World War I, aerial photography soon replaced sketching and drawing by the aerial observers. The battle maps used by both sides were produced from aerial photographs, and by the end of the war, both sides were recording the entire front at least twice a day. Cameras especially designed for use in airplanes were being produced, including thermal infra-red detectors. Stability and shutter speed remained a problem, and towards the end of the war Sherman M. Fairchild developed a camera with the shutter located inside the lens. This design significantly improved the quality of the images and became the standard for aerial camera systems over the next 50 years.
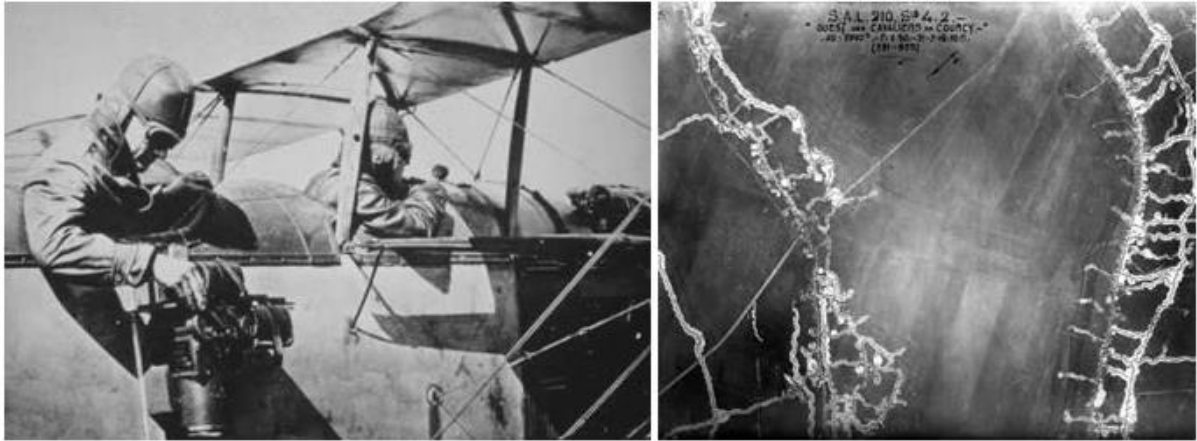
Figure 3.5 (left) Military aerial observer/photographer during World War I (right) Vertical aerial photograph of trenches in 1916.

Fast forward to 1957 USSR (Union of Soviet Socialist Republics) surprised the whole world by launching Sputnik 1. It was the first artificial Earth satellite. It was launched into an elliptical low Earth orbit by the Soviet Union on 4 October 1957 as part of the Soviet space program. It sent a radio signal back to Earth for three weeks before its three silver-zinc batteries ran out, and continued in orbit for three months until aerodynamic drag caused it to fall back into the atmosphere on 4 January 1958. The satellite's unanticipated success precipitated the American Sputnik crisis and triggered the Space Race, which was part of the Cold War between the two nations. The launch was the beginning of a new era of political, military, technological and scientific developments.

3.2 Frame to Digital image

An image is a two-dimensional representation of objects in a real scene. Remote sensing images are representations of parts of the earth surface as seen from space. The images may be analog or digital. Aerial photographs are examples of analog images while satellite images acquired using electronic sensors are examples of digital images.

A digital image comprises of a two-dimensional array of individual picture elements called pixels arranged in columns and rows. Each pixel represents an area on the Earth's surface. A pixel has an intensity value and a location address in the two-dimensional image as shown in Figure 3.6.

The intensity value represents the measured physical quantity such as the solar radiance in each wavelength band reflected from the ground, emitted infrared radiation, or backscattered radar

intensity. This value is normally the average value for the whole ground area covered by the pixel. The intensity of a pixel is digitised and recorded as a digital number. Due to the finite storage capacity, a digital number is stored with a finite number of bits (binary digits). The number of bits determine the radiometric resolution of the image. For example, an 8-bit digital number ranges from 0 to 255 (i.e. 2^8 - 1), while a 11-bit digital number ranges from 0 to 2047. Radiometric Resolution refers to the smallest change in intensity level that can be detected by the sensing system. The intrinsic radiometric resolution of a sensing system depends on the signal to noise ratio of the detector. In a digital image, the radiometric resolution is limited by the number of discrete quantization levels used to digitize the continuous intensity value. The detected intensity value needs to be scaled and quantized to fit within this range of value. In a Radiometrically Calibrated image, the actual intensity value can be derived from the pixel digital number. The address of a pixel is denoted by its row and column coordinates in the two-dimensional image. There is a one-to-one correspondence between the column-row address of a pixel and the geographical coordinates (e.g. Longitude, latitude) of the imaged location as shown in below Figure 3.6. In order to be useful, the exact geographical location of each pixel on the ground must be derivable from its row and column indices, given the imaging geometry and the satellite orbit parameters.
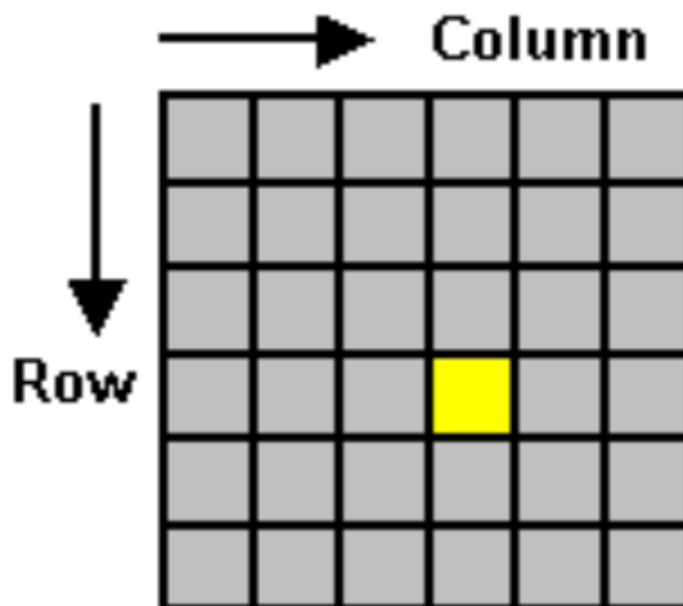
Figure 3.6 Digital image structure is a two-dimensional array of pixels. Each pixel has an intensity value (represented by a digital number) and a location address (referenced by its row and column

Multilayer Image

Several types of measurement may be made from the ground area covered by a single pixel. Each type of measurement forms an image which carry some specific information about the area. By "stacking" these images from the same area together, a multilayer image is formed. Each component image is a layer in the multilayer image.

Multilayer images can also be formed by combining images obtained from different sensors, and other subsidiary data. For example, in figure a multilayer image may consist of three layers from a SPOT multispectral image, a layer of ERS synthetic aperture radar image, and perhaps a layer consisting of the digital elevation map of the area being studied.

Source: https://crisp.nus.edu.sg/~research/tutorial/image.html
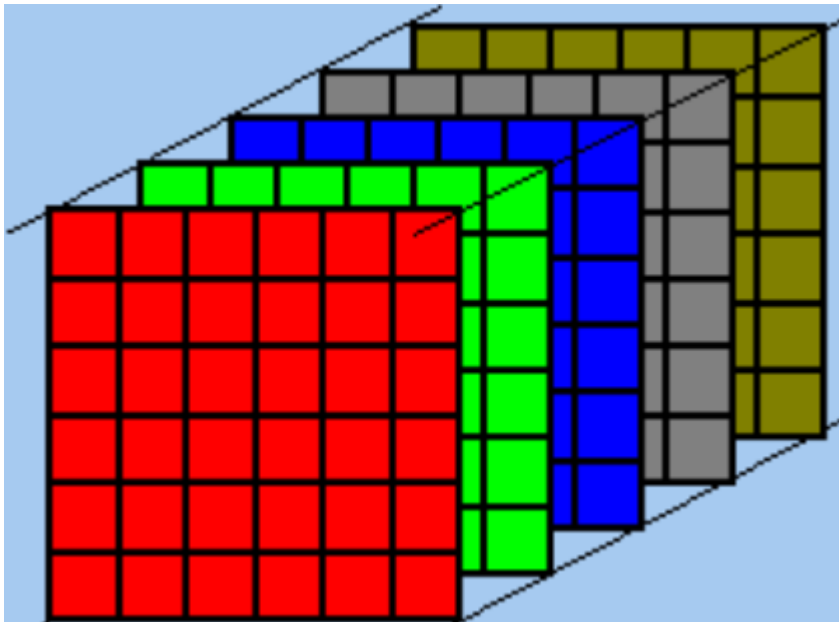
Figure 3.7 An illustration of a multilayer image consisting of five component layers.

Multispectral Image

A multispectral image consists of a few image layers, each layer represents an image acquired at a particular wavelength band. For example, the SPOT 5 HRG and HRS sensor operating in the multispectral mode detects radiations in three wavelength bands: the green (500 - 590 nm), red (610 - 680 nm), near infrared(IR)(790 - 890 nm) short wave infrared(SWIR)(1.58-1.75 nm) and Panchromatic(0.51 - 0.73nm) bands. A single SPOT-5 multispectral scene consists of Five intensity images in the Five wavelength bands. In this case, each pixel of the scene has three intensity values corresponding to the three bands. While a Landsat Thematic mapper

multispectral image consists of seven bands: blue, green, red, near-IR bands, two SWIR bands, and a thermal IR band.More detailed discussion on SPOT satellite images and Landsat images is presented in the next section

Spatial resolution refers to the size of the smallest object that can be resolved on the ground. In a digital image, the resolution is limited by the pixel size, i.e. the smallest resolvable object cannot be smaller than the pixel size. The intrinsic resolution of an imaging system is determined primarily by the instantaneous field of view (IFOV) of the sensor, which is a measure of the ground area viewed by a single detector element in a given instant in time. However, this intrinsic resolution can often be degraded by other factors which introduce blurring of the image, such as improper focusing, atmospheric scattering and target motion. The pixel size is determined by the Ground sampling distance (GSD). In remote sensing, ground sample distance (GSD) in a digital photo (such as an orthophoto) of the ground from air or space is the distance between pixel centres measured on the ground. For example, in an image with a one-meter GSD, adjacent pixels image locations are 1 meter apart on the ground.

A "High Resolution" image refers to one with a small resolution size. Fine details can be seen in a high-resolution image as shown in Figure 3.8(a). On the other hand, a "Low Resolution" image is one with a large resolution size, i.e., only coarse features can be observed in the image as shown in Figure 3.8

(a)   (b)
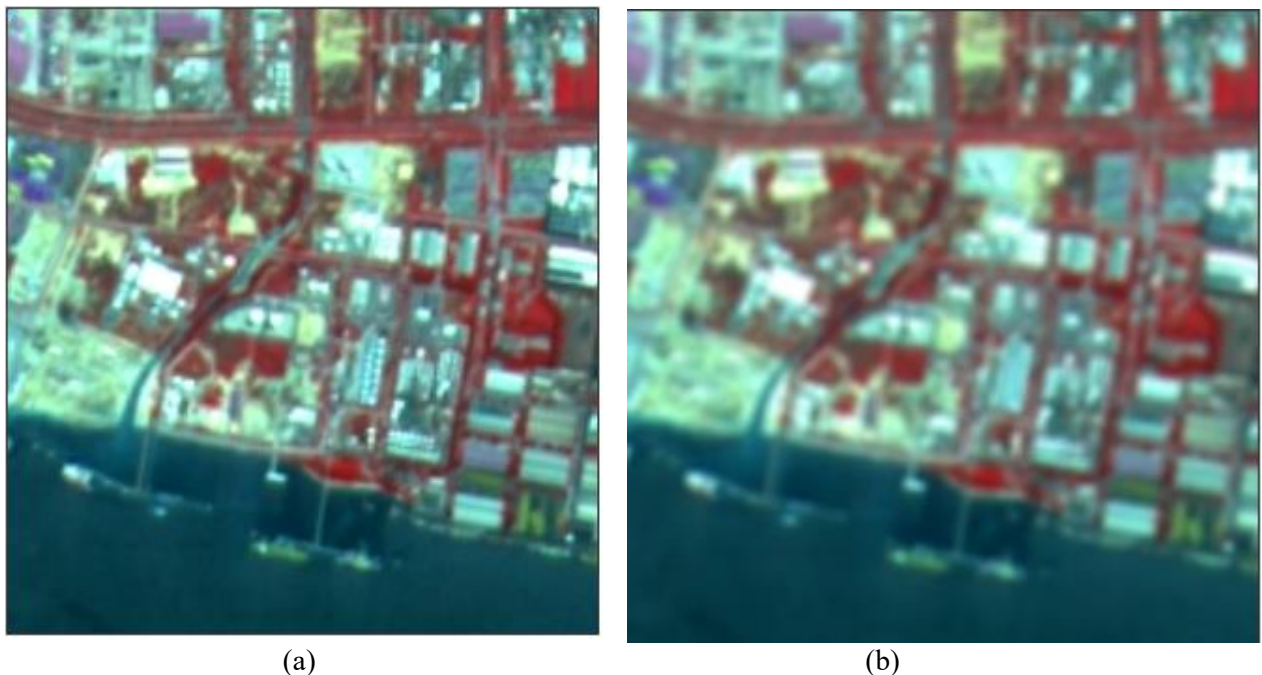
Figure 3.8 (a). False colour images from spot 5 with 10 m resolution (b)false colour Landsat 5 with 30 m resolution we can clearly see the effect of spatial resolution on the fine details of the image

Radiometric Resolution refers to the smallest change in intensity level that can be detected by the sensing system. The intrinsic radiometric resolution of a sensing system depends on the signal to noise ratio of the detector. In a digital image, the radiometric resolution is limited by the number of discrete quantization levels used to digitize the continuous intensity value.

The following images illustrate the effects of the number of quantization levels on the digital image. The first image Figure 3.9(a)is a SPOT panchromatic image quantized at 8 bits (i.e., 256 levels) per pixel. The subsequent image Figure 3.9(b) is with 2-bit quantization (4 levels).
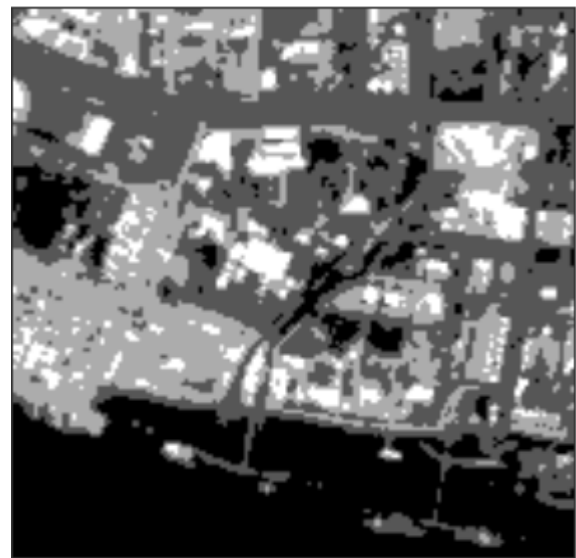
(a)   (b)

Figure 3.9 images show the effects of degrading the radiometric resolution by using fewer quantization levels.

Digitization using a small number of quantization levels does not affect very much the visual quality of the image. However, if the image is to be subjected to numerical analysis, the accuracy of analysis will be compromised if few quantization levels are used.

3.2 Landsat program

In 1965, William T. Pecora, the then director of the United States Geological Survey, proposed the idea of a remote sensing satellite program to gather facts about the natural resources of our planet. Pecora stated that the program was "conceived in 1966 largely as a direct result of the demonstrated utility of the Mercury and Gemini orbital photography to Earth resource studies." While weather satellites had been monitoring Earth's atmosphere since 1960 and were largely considered useful, there was no appreciation of terrain data from space until the mid-1960s. So, when Landsat 1 was proposed, it met with intense opposition from the Bureau of Budget and those who argued high-altitude aircraft would be the fiscally responsible choice for Earth remote sensing. Concurrently, the Department of Defence feared that a civilian program such as Landsat would compromise the secrecy of their reconnaissance missions. Additionally, there were also geopolitical concerns about photographing foreign countries without permission. In 1965, NASA began methodical investigations of Earth remote sensing using instruments mounted on planes. In 1966, the USGS convinced the Secretary of the Interior, Stewart Udall, to announce that the Department of the Interior (DOI) was going to proceed with its own Earth-observing satellite program. This savvy political stunt coerced NASA to expedite the building of Landsat. But budgetary constraints and sensor disagreements between application agencies (notably the Department of Agriculture and DOI) again stymied the satellite construction process. Finally, by 1970 NASA had a green light to build a satellite. Remarkably, within only two years, Landsat 1 was launched, heralding a new age of remote sensing of land from space.

It contributed invaluable data and launched a revolution in remote sensing technology. The satellite was designed to last one year, but surpassed expectations by orbiting an additional five years before being decommissioned on January 6, 1978. During its six-years, Landsat 1 acquired images covering about 75% of the Earth's surface. Inside Landsat 1 was a Return Beam Vidicon (RBV) and a secondary, experimental Multi-Spectral Scanner (MSS). The RBV was supposed to be the prime instrument, but the MSS data was demonstrably superior. With the success of Landsat NASA expanded the Landsat program and you can find the chronology of the launch of the satellites in Table 2.1. Landsat 5 is having the largest archive of the earth observation data it was decommissioned on June 5,2013 after 29 years of operation.

Satellites	Launched	Terminated
Landsat1	23 July 1972	6 January 1978
Landsat 2	22 January 1975	25 February 1982
Landsat 3	5 March 1978	31 March 1983
Landsat 4	16 July 182	14 December 1993
Landsat 5	1 March 1984	5 June 2013
Landsat 6	5 October 1993	Failed to reach the orbit
Landsat 7	15 April 1999	6 April 2022
Landsat 8	11 February 2013	Still active
Landsat 9	27 September	Still active

Table 3.1 Landsat program timeline for each satellite in the series

Landsat 1 through 5 carried the Landsat Multispectral Scanner (MSS). Landsat 4 and 5 carried both the MSS and Thematic Mapper (TM) instruments. Landsat 7 uses the Enhanced Thematic Mapper Plus (ETM+) scanner. Landsat 8 uses two instruments, the Operational Land Imager (OLI) for optical bands and the Thermal Infrared Sensor (TIRS) for thermal bands. All these instruments operate in visible and infrared region of Electromagnetic spectrum as shown in Figure 3.10.The spectral and spatial resolution of each satellite is summarised as shown in the Tables 3.2 ,3.3 ,3.4.We are not getting into details of senor characteristics of each satellite that is out of scope for this thesis which you will see in chapter 5.
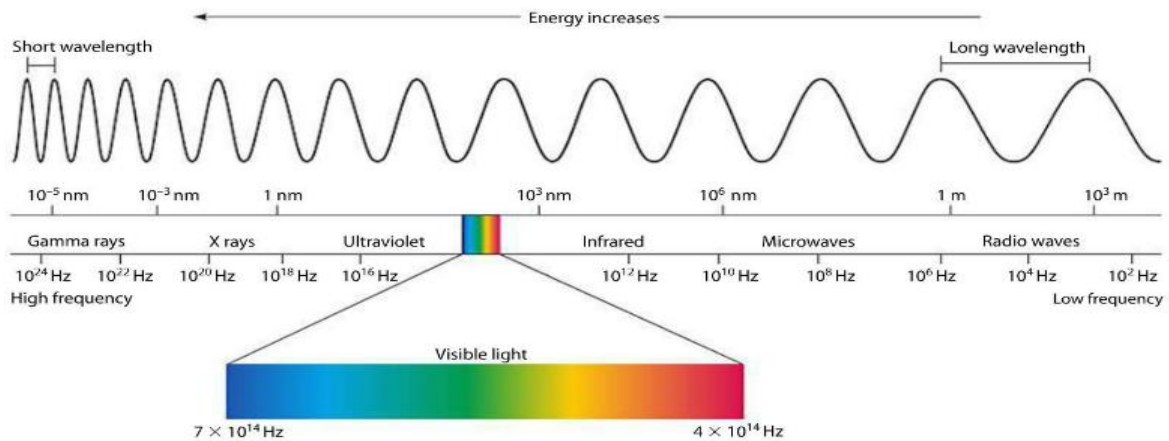
Figure 3.10 Electromagnetic spectrum covering all the wavelengths from low frequency to high frequency.

Landsat 1–3 MSS	Landsat 4–5 MSS	Wavelength (micrometers)	Resolution (meters)
Band 4 – Green	Band 1 – Green	0.5 – 0.6	60*
Band 5 – Red	Band 2 – Red	0.6 – 0.7	60*
Band 6 – Near Infrared (NIR)	Band 3 – NIR	0.7 – 0.8	60*
Band 7 – NIR	Band 4 – NIR	0.8 – 1.1	60*

*Original MSS pixel size was 79 x 57 meters; production systems now resample the data to 60 meters

Table 3.2 Landsat 1–5 Multispectral Scanner (MSS) Spectral and spatial resolution

Bands	Wavelength (micrometers)	Resolution (meters)
Band 1 – Blue	0.45 – 0.52	30
Band 2 – Green	0.52 – 0.60	30
Band 3 – Red	0.63 – 0.69	30
Band 4 – NIR	0.76 – 0.90	30
Band 5 – Shortwave Infrared (SWIR) 1	1.55 – 1.75	30

Band 6 – Thermal	10.40 – 12.50	120* (30)
Band 7 – SWIR 2	2.08 – 2.35	30

* TM Band 6 was acquired at 120-meter resolution, but products are resampled to 30-meter pixels.

Table 3.3 Landsat 4–5 Thematic Mapper (TM) Spectral and Spatial resolution

Bands	Wavelength (micrometers)	Resolution (meters)
Band 1 – Blue	0.45 – 0.52	30
Band 2 – Green	0.52 – 0.60	30
Band 3 – Red	0.63 – 0.69	30
Band 4 – NIR	0.77 – 0.90	30
Band 5 – SWIR 1	1.55 – 1.75	30
Band 6 – Thermal	10.40 – 12.50	60* (30)
Band 7 – SWIR 2	2.09 – 2.35	30
Band 8 – Panchromatic	0.52 – 0.90	15

* TM Band 6 was acquired at 60-meter resolution, but products are resampled to 30-meter pixels

Table 3.4 Landsat 7 Enhanced Thematic Mapper Plus (ETM+) Spectral and Spatial resolution

Bands	Wavelength (micrometers)	Resolution (meters)
Band 1 - Ultra Blue (coastal/aerosol)	0.435 – 0.451	30
Band 2 - Blue	0.452 – 0.512	30
Band 3 - Green	0.533 – 0.590	30
Band 4 – Red	0.636 – 0.673	30
Band 5 – NIR	0.851 – 0.879	30
Band 6 – SWIR 1	1.566 – 1.651	30

Band 7 – SWIR 2	2.107 – 2.294	30
Band 8 – Panchromatic	0.503 – 0.676	15
Band 9 – Cirrus	1.363 – 1.384	30
Band 10 – Thermal 1	10.60 – 11.19	100* (30)
Band 11 – Thermal 2	11.50 – 12.51	100* (30)

* Thermal Infrared Sensor Bands was acquired at 100-meter resolution, but products are resampled to 30-meter pixels

Table 3.5 Landsat 8 Operational Land Imager (OLI) and Thermal Infrared Sensor (TIRS) resolution in each band

An advantage of Landsat imagery, and remote sensing in general, is that it provides data at a synoptic global level that is impossible to replicate with in situ measurements. However, there are trade-offs between the local detail of the measurements (radiometric resolution, number of spectral bands) and the spatial scale of the area being measured. Landsat imagery is coarse in spatial resolution compared to using other remote sensing methods, such as imagery from High resolution cameras from drones, UAV's, LiDAR etc which we will discuss in section 3.6. Compared to other satellites, Landsat's spatial resolution is relatively high, yet revisit time is relatively less frequent.

3.3 Spot satellites

After the success of Landsat program even other developed nations started investing in earth observation systems. Spot satellite series Initiated by the French space agency CNES in 1977 and run by Spot Image, based in Toulouse, France, SPOT was the first European Earth-observation satellite programme. The series was developed in association with Belgian and Swedish institutions. The SPOT (Satellite Pour l'Observation de la Terre) series under CNES operated five satellites between 1986 and 2015, creating a 29-year archive of high-resolution imagery.CNES continued the legacy of the original five SPOT satellites(Spot 4 and 5 as shown in Figure 3.11) with the Pléiades satellites, offering improved imaging capabilities.
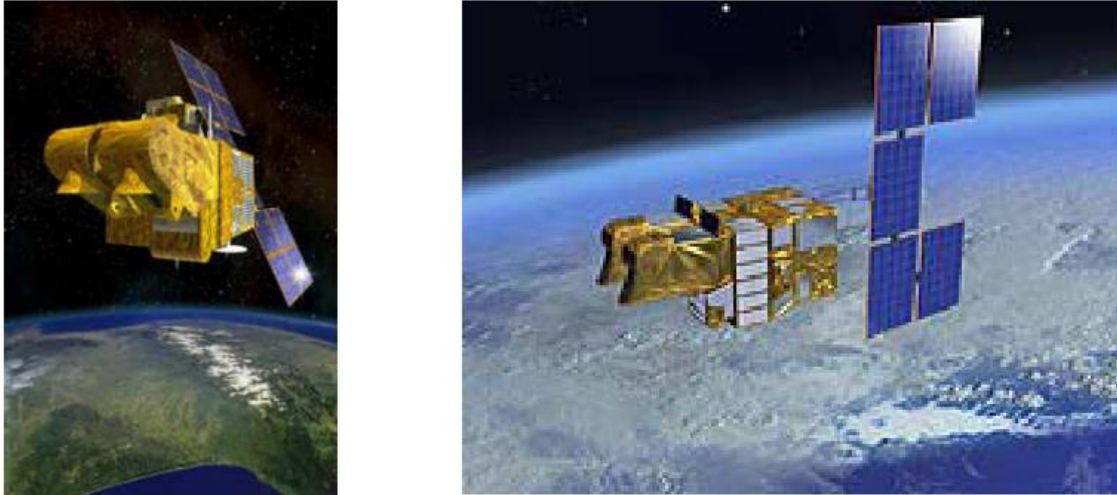
Figure 3.11 Artistic view of Spot 4(left) and Spot 5(Right)

Source: ©2022 CNES

Airbus Defence and Space continued with the SPOT series when CNES ended their programme in 2015. Airbus' commercial SPOT 6 and SPOT 7, launched in 2012 and 2014 respectively, also work with the Pléiades satellites, offering very high-resolution imagery and data continuity for their predecessors in the series.

The SPOT satellite constellation offers acquisition and daily revisit capacity for anywhere in the world. SPOT produces two high resolution optical images. The multispectral mode is in the red, green, and infrared bands of the Electromagnetic spectrum. The panchromatic mode is a single wide band in the visible part of the spectrum with higher resolution. In 1986, SPOT 1 became one of the most sophisticated Earth observation satellites of its time. It had a ground resolution of 10 metres whereas Landsat-5 had 30 metres. SPOT 1 provided the first usable elevation data for a sizeable portion of the planet's landmass, using two-pass stereoscopic correlation.

SPOT 1 sent nearly 2.7 million high-quality images down to Earth, for the benefit of scientists, government agencies, regional authorities, and many other stakeholders. Ten days after the Chernobyl nuclear disaster, SPOT 1 provided images of the highly contaminated zone. 115,000 people were evacuated because of the Chernobyl disaster. This area was known as the "exclusion zone" which is a 30 km buffer around the nuclear power plant. The evacuation area could only be seen by satellite. The first sign of recovery was found in 1988. SPOT 1 uncovered photosynthesis using the near-infrared sensor. Over the years, the SPOT family has kept a watchful eye on new infrastructure, decontamination activities and reforestation of the area.

HRV (High Resolution Visible) instrument was on board for Spot 1,2,3. Two identical HRV imaging instruments on SPOT 1,2,3 provided data at 10 metre spatial resolution and were able to operate in two modes Panchromatic (PAN) mode and 20 metre Multispectral (MS) mode with a swath of 60 km simultaneously or individually. For Spot 4 with respect to the HRV instrument on board SPOT 1, 2 and 3.HRV got a little update to High Resolution Visible and Infrared (HRVIR) had the same geometric imaging characteristics, but improved performance was achieved by adding a new shortwave infrared spectral band (SWIR). Two identical HRVIR imaging instruments on SPOT 4 were able to operate in two modes either simultaneously or individually. SPOT 5 had two High resolution geometric (HRG) instruments as shown in Figure 2.9 that were deduced from the HRVIR of SPOT 4 and High Resolution Stereoscopic (HRS) as shown in Figure 3.12 which can produce across the track stereoscopic images and along the track stereoscopic images which will be discussed in detail in Chapter 5. They offered a higher resolution of 2.5 to 5 metres in panchromatic mode and 10 metres in multispectral mode (20 metre on short wave infrared 1.58 – 1.75 μm). HRG instruments can operate in two modes, either simultaneously or individually; they had a swath of 117 km^2 if operated simultaneously with an overlap of 3 km^2. The HRS imaging instrument operated in panchromatic mode and pointed forward and backward enabling it to take stereo pair images to show map relief with scene lengths up to 600 km^2. SPOT 5 provided imagery with a swath of 120 km^2. For SPOT 6 and 7 we got a new instrument compared to previous spot missions which is Naomi New Astrosat Optical Modular Instrument (NAOMI). Two identical NAOMI instruments on board SPOT 6 provide data up to 1.5 m spatial resolution panchromatic and multispectral. They can operate both in two modes, either simultaneously or individually. In

simultaneous mode the swath is 120 km^2 and individual mode the swath is 60 km^2. spot satellites characteristics and operation timelines are summarized in Table 3.6
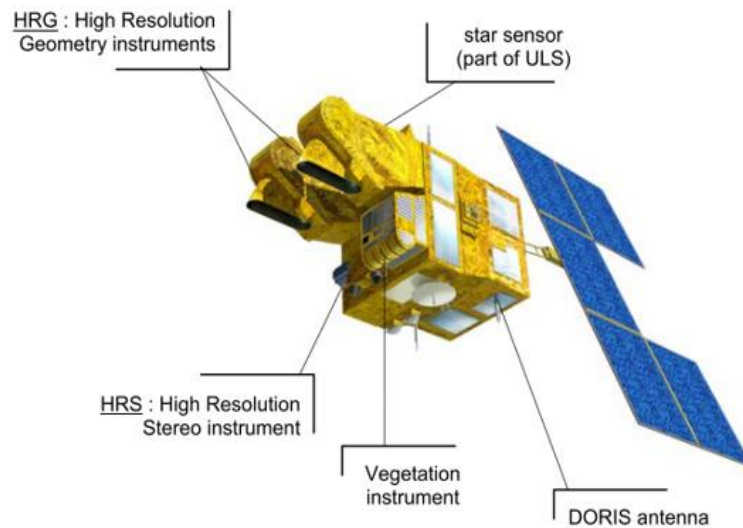
Image source: Spot 5 handbook

Figure 3.12: SPOT 5 Satellite on board instruments

	SPOT 1	SPOT 2	SPOT 3	SPOT 4	SPOT 5	SPOT 6	SPOT 7
Operators	CNES(owner) Spot Image (operator)					Airbus DS	
Launch dates	22 February 1986	22 January 1990	26 September 1993	24 March 1998	4 May 2002	9 September 2012	30 June 2014
EOL	November 2003	July 2009	November 1996	29 June 2013	March 2015	Operating nominally	Operating nominally
Orbit height	832 km					694km	
Orbit type	Near polar, sun-synchronous phased orbit local equator crossing time 10:30 on descending orbit at an altitude of 830 km completing over 14 revolutions per day						
Orbit period	101 minutes					98.79 minutes	
Inclination	98.7º					98.2º	

Repeat cycle	26 days						
Onboard sensors provided under TPM	HRV	HRV	HRV	HRVIR, Vegetation	HRG, HRS Vegetation	Naomi	Naomi
Resolution	HRV: 10 m (PAN), 20 m			HRVIR: 10 m (PAN), 20 m	HRG: 2.5 m (PAN), 10 m (MS), 20 (SWIR) HRS: 10 m (cross track), 5 m (along-track)	1.5 m (PAN), 6 m (MS)	
Swat width	HRV: 117 (60 + 60) km			HRVIR: 117 (60 + 60) km	HRG: 117 (60 + 60) km HRS: 120 km	60 km	

Table 3.6 The launch and operating timeline and characteristics of each spot machines

Spot 5 mission objectives

Here I will be discussing only about the mission objectives of SPOT 5 because the data from this satellite was used for data processing for our case study which we will discuss in detail in chapter 5

The overall mission objectives for SPOT 5 were:

- To provide image acquisition and service continuity consistent with previous SPOT satellites to satisfy the user investments. Hence, the same Sun-synchronous orbit is used providing the existing functional instrument capabilities with a 26 day repeat cycle, the same off-track viewing capability of $\pm 27°$ about nadir, the same spectral band selection, and the same 60 km double swath.
- To improve the spatial resolution of the imagery to < 3 m in the panchromatic band and to 10 m in the multispectral mode. The SWIR (Short wave infrared) band imagery remains at 20 m.
- To offer in parallel a stereoscopic along-track observation capability as shown in Figure 3.13 (instead of the previously provided cross-track capability). The intent is to offer

high-resolution imagery to be used for DEM (Digital Elevation Model) generation with an accuracy of 10 m.
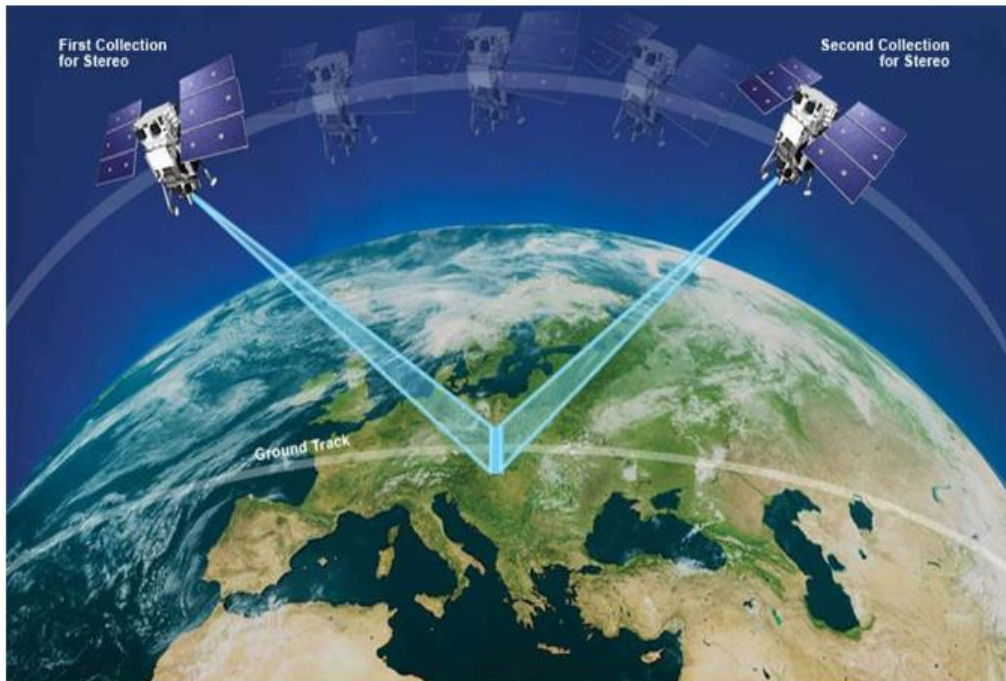
Source: Digital Globe.

Figure 3.13 Along the track stereo collection mode. The sensor collects two shots (45-90 seconds apart) of the same location by adjusting its camera before completing its orbit and spot 5 HRS sensor collects similar the stereo pairs before completion of the orbit.

Upgrades from previous spot missions

Compared to its predecessors, SPOT 5 offered greatly enhanced capabilities: thanks to SPOT 5's improved 5 metre and 2.5 metre resolution and wide imaging swath, which covered 60 x 60 km or 60 km x 120 km. In twin-instrument mode, the SPOT 5 satellite provided an ideal balance between high resolution and wide-area coverage. SPOT 5's other key feature was the unprecedented acquisition capability of the on-board HRS stereo viewing instrument as shown in Fig 2.9, which acquires stereo images over vast areas in a single pass. Stereo pair imagery is vital for applications that call for 3D terrain modelling and computer environments, such as flight simulator databases, pipeline corridors and mobile phone network planning.

3.4 Copernicus program

In May of 1998, a vision for a European environment monitoring programme was agreed upon in Baveno, Italy. In the 20 years since, this vision has grown beyond expectations, giving rise to Copernicus, the most ambitious and successful Earth Observation programme in the world.

The seven Copernicus Sentinel satellites in orbit, complemented by contributing missions, in situ sensors and numerical models, deliver terabytes of full, free and open data daily to hundreds of thousands of users which can be downloaded from Copernicus website(https://www.copernicus.eu/en). Copernicus also supports tens of thousands of jobs and generates billions of Euros in economic benefits, but the full potential of the programme is yet to be unleashed.

As part of the Space Component of the Copernicus programme, state-of-the-art satellites called Sentinels as summarised in Table 3.7 have been developed, produced and launched by the European Space Agency and its partners on behalf of the European Union, which is the owner of the satellites. The free, full and open access to the data provided by the Sentinels enables users worldwide to create ground-breaking applications. The Copernicus programme also includes six thematic services that allow public and private users to use Copernicus data to tackle a wide range of societal challenges.

Satellite	Applications
Sentinel 1	Sentinel-1 is providing all-weather, day and night radar imagery for land, emergency management and ocean applications from 2014.
Sentinel 2	Sentinel-2 is providing high-resolution optical imagery for land services from 2015.
Sentinel 3	Sentinel-3 is delivering high-accuracy optical, radar and altimetry data for marine and land monitoring services from 2016.
Sentinel 4	From 2023 onwards, Sentinel-4 will provide data for atmospheric composition monitoring.
Sentinel 5	As of 2021, Sentinel-5 will also be dedicated to atmospheric composition monitoring.
Sentinel 5p	Sentinel-5 Precursor which was launched in 2017 is a gap filler mission aiming to provide Air Quality data continuity until the launch of Sentinel-5.

Table 3.7 Thematic services of the Copernicus program and their applications

We are not getting into details, what is function and objectives of all the sentinel satellites. We are going discuss briefly about sentinel 1 in the next section 2.4.1 which was used in the data processing for our case study which you see in chapter 5.

3.4.1 Sentinel 1

The Sentinel-1 mission is the European Radar Observatory for the Copernicus joint initiative of the European Commission (EC) and the European Space Agency (ESA). Copernicus is a European initiative for the implementation of information services dealing with environment and security. It is based on observation data received from Earth Observation satellites and ground-based information.

The Sentinel-1 mission includes C-band imaging operating in four exclusive imaging modes with different resolution (down to 5 m) and coverage (up to 400 km). It provides dual polarisation capability, very short revisit times and rapid product delivery. For each observation, precise measurements of spacecraft position and attitude are available.

Synthetic Aperture Radar (SAR) (see section 3.5 for more details) has the advantage of operating at wavelengths not impeded by cloud cover or a lack of illumination and can acquire data over a site during day or night-time under all weather conditions. Sentinel-1, with its C SAR instrument, can offer reliable, repeated wide area monitoring. The mission is composed of a constellation of two satellites, Sentinel-1A and Sentinel-1B, sharing the same orbital plane.

Sentinel-1 is designed to work in a pre-programmed, conflict-free operation mode, imaging all global landmasses, coastal zones and shipping routes at high resolution and covering the global ocean with vignettes. This ensures the reliability of service required by operational services and a consistent long term data archive built for applications based on long time series.

Sentinel-1 operates in four exclusive acquisition modes as shown in Figure 3.14:

• Strip map (SM)

• Interferometric Wide swath (IW)

• Extra-Wide swath (EW)

• Wave (WV).

The Sentinel-1 C-band SAR instruments supports operation in single polarisation (HH or VV) and dual polarisation (HH+HV or VV+VH), implemented through one transmit chain (switchable to H or V) and two parallel receive chains for H and V polarisation.

SM, IW and EW products are available in single (HH or VV) or dual polarisation (HH+HV or VV+VH). WV is single polarisation only (HH or VV).

The primary conflict-free modes are IW, with VV+VH polarisation over land, and WV, with VV polarisation, over open ocean. EW mode is primarily used for wide area coastal monitoring including ship traffic, oil spill and sea-ice monitoring. SM mode is only used for small islands and on request for extraordinary events such as emergency management.

Having the Interferometric Wide swath mode as the one main operational mode satisfies most current service requirements, avoids conflicts, and preserves revisit performance, simplifies mission planning, decreases operational costs, and builds up a consistent long-term archive.

For each mode, it will be possible to produce products at SAR Level-0, Level-1 SLC, Level-1 GRD and Level-2 OCN.
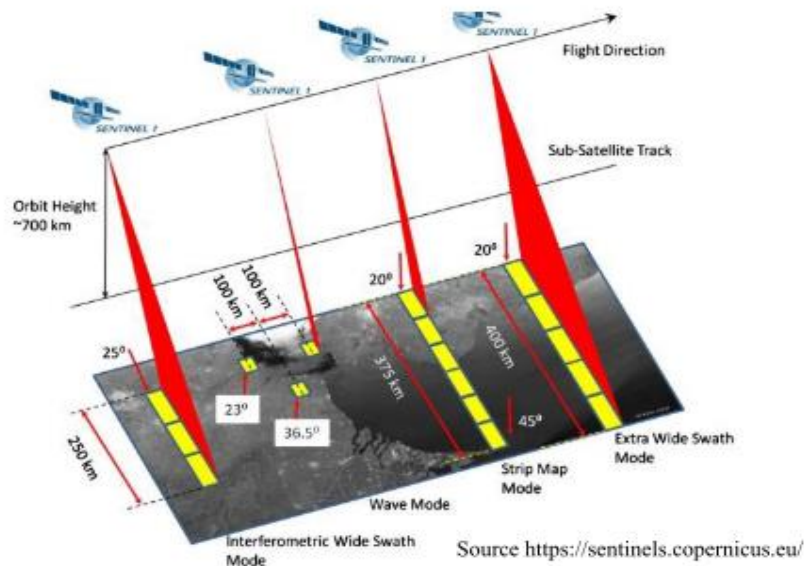
Figure 3.14 Sentinel 1 different product modes

Product Types and Processing Levels

Sentinel-1 data products acquired in SM, IW and EW mode which are generated by the PDGS operationally are distributed at three levels of processing.

• Level-0

• Level-1

• Level-2.

Level-1 products can be one of two product types - either Single Look Complex (SLC) or Ground Range Detected (GRD). Level-2 Ocean (OCN) products can have different components available depending on the acquisition mode.

Products are designated based on their acquisition mode, product type and in the case of Level1 GRD also its resolution.

All products are processed directly from the Level-0 product. Each mode can potentially generate Level-1 SLC, Level-1 GRD and Level-2 Ocean products as shown in Fig 2.12. For WV mode, the Level-0 products are not distributed; the access to WV_SLC product has been possible since 2016.

Source: https://sentinels.copernicus.eu/
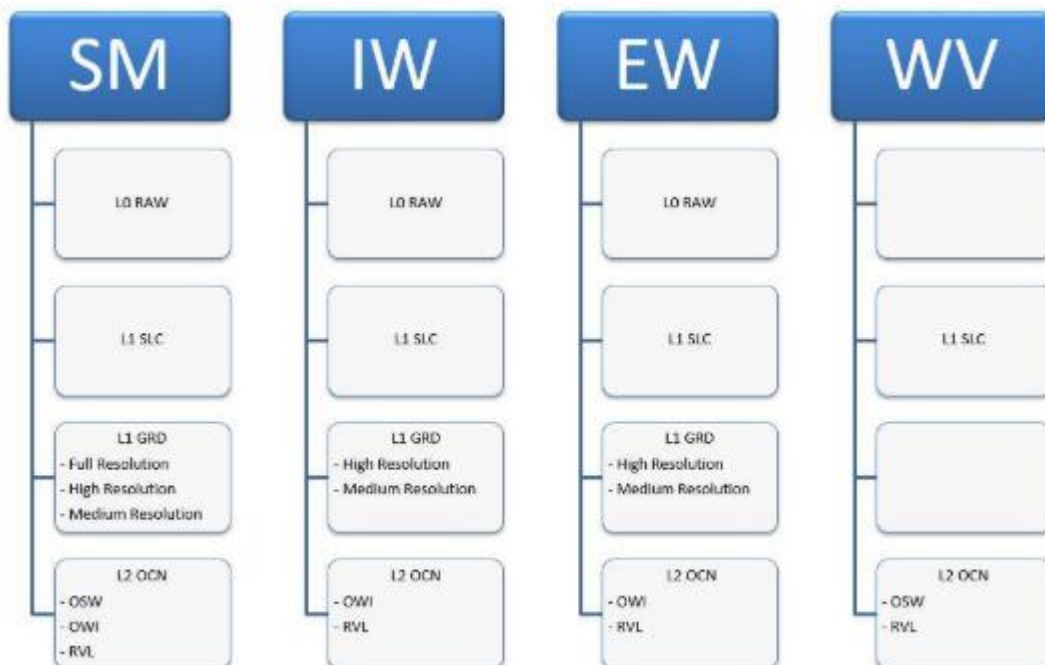
Figure 3.15 Product Levels from each Mode

Revisit and Coverage

The SENTINEL-1 constellation offers an improvement in revisit time over ERS-1/2 and ENVISAT ASAR, and a continuity of wide area coverage with ENVISAT ASAR, but achieving higher resolution and potentially global dual polarisation coverage over landmasses. Each SENTINEL-1 satellite will be in a near-polar, sun-synchronous orbit, with a 12-day repeat cycle and 175 orbits per cycle. Both SENTINEL-1A and SENTINEL-1B share the same orbit plane with a 180° orbital phasing difference. A single SENTINEL-1 satellite is potentially able to map the global landmasses in the Interferometric Wide swath mode once every 12 days, in a single pass (ascending or descending). The two-satellite constellation offers a 6-day exact repeat cycle at the equator. Since the orbit track spacing varies with latitude, the revisit rate is significantly greater at higher latitudes than at the equator.

3.5 DEM Generation using InSAR Technique

The fundamental differences of Earth observation technologies depend on whether the data is collected through a passive or an active remote sensing system.

Passive remote sensing

A satellite has a remote sensing payload to monitor the solar energy which Earth's surface or atmosphere reflects and re-emissions into space. This technology delivers data only in sunlight, cloudless circumstances. Commonly used passive sensors include optical and thermal sensors.

Active remote sensing

A satellite sends energy to Earth and then measures the energy received back from the Earth's surface or atmosphere. Commonly used active sensors include radar and laser technologies. There are two types of radar-based systems that are used for satellite-based microwave imaging:

Real Aperture Radar (RAR)

Synthetic-Aperture Radar (SAR)

Active imaging systems, especially Synthetic-Aperture Radar, is the only instrument that can penetrate clouds and doesn't require sunlight to provide reliable remote sensing data. This is especially relevant for monitoring those areas of the Earth which most of the time are covered with clouds, such as in Northern Europe, South American rainforests, or South-East Asia.

While most of discussing till now in this thesis is about the remote sensing that is passive, for example optical images from the U.S. Geological Survey's Landsat, French space agency (CNES) Spot series satellites, another type of remote sensing data is making waves: Synthetic Aperture Radar, or SAR. SAR is a type of active data collection where a sensor produces its own energy and then records the amount of that energy reflected after interacting with the Earth. While optical imagery is like interpreting a photograph, SAR data require a different way of thinking in that the signal is instead responsive to surface characteristics like structure and moisture.

The spatial resolution of radar data is directly related to the ratio of the sensor wavelength to the length of the sensor's antenna. For a given wavelength, the longer the antenna, the higher the spatial resolution. From a satellite in space operating at a wavelength of about 5 cm (C-band radar), to get a spatial resolution of 10 m, you would need a radar antenna about 4,250 m long. (That's over 47 football fields!).

An antenna of that size is not practical for a satellite sensor in space. Hence, scientists and engineers have come up with a clever workaround — the synthetic aperture. In this concept, a sequence of acquisitions from a shorter antenna are combined to simulate a much larger antenna, thus providing higher resolution data (view geometry figure to the right).

The Role of Frequency and wavelength

Optical sensors such as Landsat's Operational Land Imager (OLI) and Sentinel-2's Multispectral Instrument (MSI) collect data in the visible, near-infrared, and short-wave infrared portions of the electromagnetic spectrum. Radar sensors utilize longer wavelengths at the centimetre to meter scale, which gives it special properties, such as the ability to see through clouds (view electromagnetic spectrum to the right). The different wavelengths of SAR are often referred to as bands, with letter designations such as X, C, L, and P as show in the below Figure 3.16. The table below notes the band with associated frequency, wavelength, and the application typical for that band.
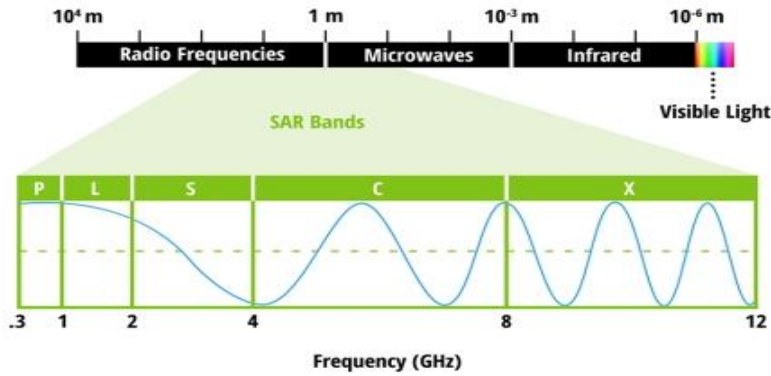
Figure 3.16 The electromagnetic spectrum with microwave bands inset in which SAR
Operates and each band has a specific application and compromise.

Band	Frequency	Wavelength	Typical Application
Ka	27–40 GHz	1.1–0.8 cm	Rarely used for SAR (airport surveillance)
K	18–27 GHz	1.7–1.1 cm	rarely used (H_2O absorption)
Ku	12–18 GHz	2.4–1.7 cm	rarely used for SAR (satellite altimetry)
X	8–12 GHz	3.8–2.4 cm	High resolution SAR (urban monitoring, ice and snow, little penetration into vegetation cover; fast coherence decay in vegetated areas)
C	4–8 GHz	7.5–3.8 cm	SAR Workhorse (global mapping; change detection; monitoring of areas with low to moderate penetration; higher coherence); ice, ocean maritime navigation
S	2–4 GHz	15–7.5 cm	Little but increasing use for SAR-based Earth observation; agriculture monitoring (NISAR will carry an S-band channel; expends C-band applications to higher vegetation density)
L	1–2 GHz	30–15 cm	Medium resolution SAR (geophysical monitoring; biomass and vegetation mapping; high penetration, InSAR)
P	0.3–1 GHz	100–30 cm	Biomass. First p-band spaceborne SAR will be launched ~2020; vegetation mapping and assessment. Experimental SAR.

Table 3.8 Frequency and wavelength range in which each SAR Band and their applications

Wavelength is an important feature to consider when working with SAR, as it determines how the radar signal interacts with the surface and how far a signal can penetrate a medium. For example, an X-band radar, which operates at a wavelength of about 3 cm, has very little capability to penetrate broadleaf forest, and thus mostly interacts with leaves at the top of the tree canopy. An L-band signal, on the other hand, has a wavelength of about 23 cm, achieving greater penetration into a forest and allowing for more interaction between the radar signal and large branches and tree trunks. Wavelength doesn't just impact the penetration depth into forests, but also into other land cover types such as soil and ice.

For example, scientists and archaeologists are using SAR data to help "uncover" lost cities and urban-type infrastructures hidden over time by dense vegetation or desert sands.

Polarization and Scattering Mechanisms

Radar can also collect signals in different polarizations, by controlling the analysed polarization in both the transmit and receive paths. Polarization refers to the orientation of the plane in which the transmitted electromagnetic wave oscillates. While the orientation can occur at any angle, SAR sensors typically transmit linearly polarized. The horizontal polarization is indicated by the letter H, and the vertical polarization is indicated by V.

The advantage of radar sensors is that signal polarization can be precisely controlled on both transmit and receive. Signals emitted in vertical (V) and received in horizontal (H) polarization would be indicated by a VH. Alternatively, a signal that was emitted in horizontal (H) and received in horizontal (H) would be indicated by HH, and so on. Examining the signal strength from these different polarizations carries information about the structure of the imaged surface, based on the following types of scattering: rough surface, volume, and double bounce (view Figure 3.17 below).

Rough surface scattering as shown in Figure 3.17, such as that caused by bare soil or water, is most sensitive to VV scattering. Volume scattering, for example, caused by the leaves and branches in a forest canopy, is most sensitive to cross-polarized data like VH or HV. The last type of scattering, double bounce, is caused by buildings, tree trunks, or inundated vegetation and is most sensitive to an HH polarized signal.
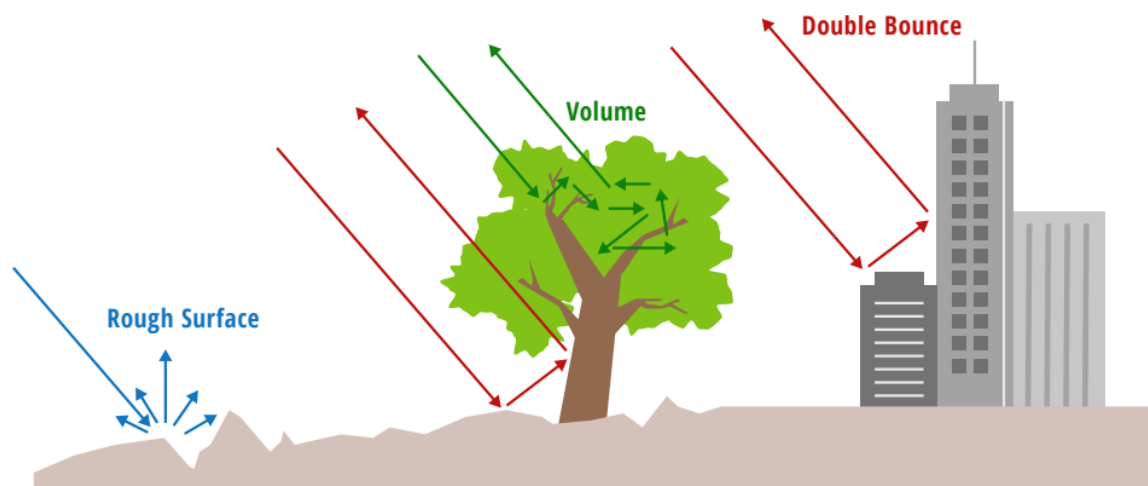
RELATIVE SCATTERING STRENGTH BY POLARIZATION:

Rough Surface Scattering $|S_{VV}| > |S_{HH}| > |S_{HV}|$ or $|S_{VH}|$

Double Bounce Scattering $|S_{HH}| > |S_{VV}| > |S_{HV}|$ or $|S_{VH}|$

Volume Scattering   Main source of $|S_{HV}|$ and $|S_{VH}|$

Image courtesy**:** Nasa SAR handbook

Figure 3.17 Strong scattering in HH indicates a predominance of double-bounce scattering (e.g., stemmy vegetation, manmade structures), while strong VV relates to rough surface scattering (e.g., bare ground, water), and spatial variations in dual polarization indicate the distribution of volume scatterers (e.g., vegetation and high-penetration soil types such as sand or other dry porous soils).

It is important to note that the amount of signal attributed to different scattering types may change as a function of wavelength, as wavelength changes the penetration depth of the signal. For example, a C-band signal penetrates only into the top layers of the canopy of a forest, and therefore will experience mostly roughness scattering mixed with a limited amount of volume scattering. However, a L-band or P-band signal will have much deeper penetration and therefore experience strongly enhanced volume scattering as well as increasing amounts of double-bounce scattering caused by the tree trunk, view canopy penetration in below Figure 3.18.

X-BAND 3 cm   C-BAND 6 cm   L-BAND 24 cm   P-BAND 65 cm
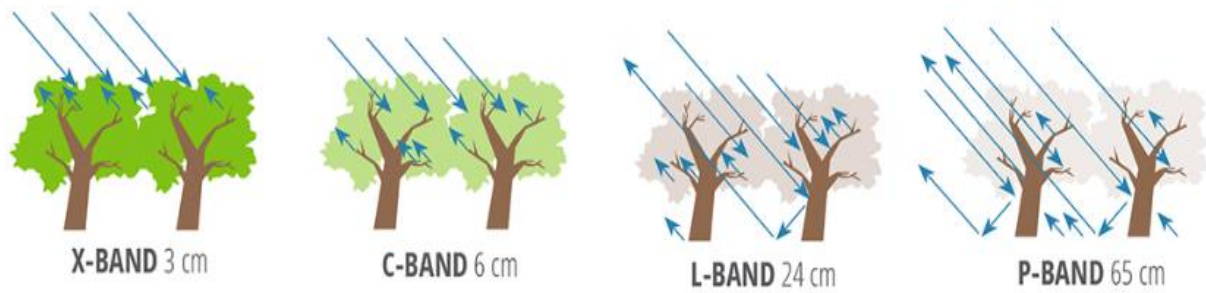
Image courtesy: Nasa SAR book

Figure 3.18 Sensitivity of SAR measurements to forest structure and penetration into the canopy at different wavelengths used for airborne or spaceborne remote sensing observations of the land surface.

Interferometry (InSAR)

SAR data can also enable an analysis method called interferometry, or InSAR. InSAR uses the phase information recorded by the sensor to measure the distance from the sensor to the target. When at least two observations of the same target are made, the distance, with additional geometric information from the sensor, can be used to measure changes in land surface topography. These measurements are very accurate (up to the centimetre level!) and can be used to identify areas of deformation from events like volcanic eruptions and earthquakes (view interferogram to the right).

Data Availability

Only recently have consistent SAR datasets been widely available for free, starting with the launch and open data policy of the European Space Agency's (ESA) Sentinel-1a in 2014. Other sensors have historic data, imagery that is only available for certain areas, or policies that require the purchase of data. All free and publicly available SAR data can be accessed in Nasa Earth data Search.

.

Data Processing and Analysis of SAR data

One of the limitations of working with SAR data has been the somewhat tedious preprocessing steps that lower-level SAR data requires. Depending on the type of analysis you want to do, these preprocessing steps can include:

- **Applying the orbit file**: Defines the relationship between ground and image coordinates, improves accuracy of later orbit-based calibration steps.
- **Radiometric calibration**: Converts the image pixel values from digital number (DN) to a standard geophysical measurement unit of radar backscatter.
- **De-bursting**: Converts the image pixel values from digital number (DN) to a standard geophysical measurement unit of radar backscatter.
- **Multilooking** Uses spatial averaging to reduce image speckle noise and converts to ground range, producing an image with a standard pixel size. Reduces image resolution (optional).
- **Speckle filtering**: Removes noise, or speckle, in an image. Many types of speckle filters can be applied, and different applications have specific filters that may work best. Unlike multilooking, this step does not reduce image resolution.
- **Terrain Flattening (RTF) & Geocoding:** RTF: Uses a DEM to remove geometry-dependent radiometric distortions; normalizes measured backscatter with respect to terrain slope.

To generate DEM using SAR following steps are followed to process the data in (Sentinel Application platform) SNAP software.

1.Coregistration

To exploit the phase difference between of the acquisitions a stack containing both products must be created. Co-registration makes use of image statistics to align both products at sub-pixel accuracy. While conventional strip map radar products can be co-registered with in one step.

2.Interferogram formation and coherence estimation

As interferogram is formed by cross multiplying the reference image with the complex conjugate of the secondary. The amplitude of both images is multiplied while the phase represents the phase difference between the two images. The interferometric phase of each SAR image pixel would depend only on the difference in the travel paths from each of the two

SARs to the considered resolution cell. According the computed interferogram contains phase variation. Coherence is calculated as a separate raster band and shows how similar each pixel is between the secondary and reference images in a scale from 0 to 1. Areas of high coherence will appear bright whereas areas of low coherence will be dark.

3.Tops Deburst

To remove the seam lines between the single bursts, the S-1 tops deburst operator is applied to the interferogram product.it does not require any user input the output will contain the same bands as the input but with merged bursts according to their zero doppler time for more information about this refer to sentinel 1 user guide.

4.Goldstein phase filtering

Interferometric phase can be corrupted by noise from temporal and geometric decorrelation, volume scattering and other processing errors. Phase information in decorrelated areas cannot be restored, but the quality of fringes existing in the interferogram can be increased by applying specialized phase filters, such as Goldstein filter which uses Fast Fourier transformation(FFT) to enhance the signal to noise ratio of the image. This is required for a proper unwrapping in the subsequent step. A detailed description of this filter and its parameters is given in the publication of Goldstein and Werner (1998).

5 Creation of subset

Since the aim of this thesis is to study belvedere glacier, we don't need to process the whole footprint of the sentinel 1 images we can reduce the analysis just to area of interest in order save the processing time of analysis.

6.Phase unwrapping

The absolute unwrapped interferometric phase derived is directly proportional to the difference in path lengths for the SAR image pair. Applications of interferometry relate the unwrapped phase to geophysical parameters such as elevation, and deformation due to ice motion, surface subsidence, earthquakes, volcanic inflation/deflation, and tectonic motion. The complex-valued interferogram values, however, are known only modulo 2π as shown in Figure 3.19 must be unwrapped to obtain a quantitative interpretation. Phase unwrapping is the process of restoring the correct multiple of 2π to each point of the interferometric phase image as shown in Figure 3.19. For a well-behaved smooth phase field all the unwrapped phase differences

between adjacent interferogram samples lie between - π and + π. When this is true, phase unwrapping is straightforward. The unwrapped phase can be evaluated by a simple path independent integration of the phase differences of adjacent wrapped phases, starting from a reference location and using the assumption that all phase differences are in the interval (-π, π).
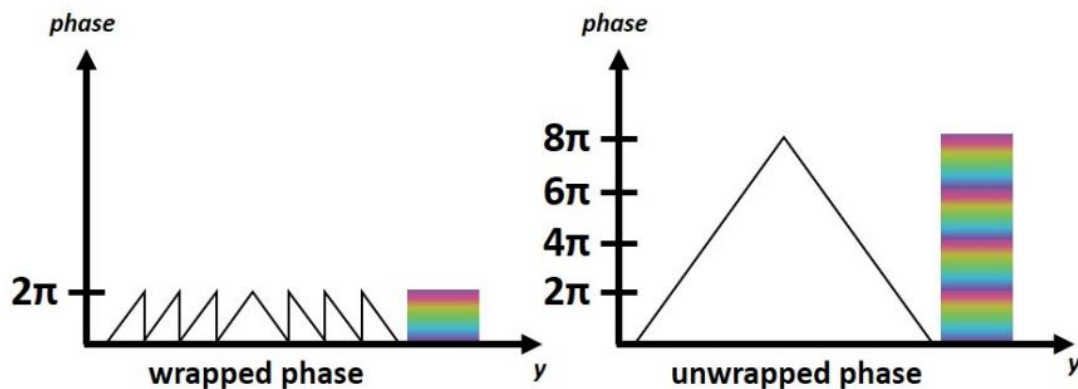
Figure 3.19: Principle of phase unwrapping

In actual interferograms phase unwrapping is more complicated because of phase steps outside the interval (-π, π). Causes for local phase gradients larger than π are:

- Phase Noise: Temporal decorrelation, shadow, and low SNR cause phase noise. For repeat-track interferometry temporal decorrelation is often the main cause.
- Phase Under-sampling: The phase is under sampled when the phase gradient exceeds half a fringe (phase cycle) per sample. In the presence of phase noise, the under-sampling already occurs at lower gradients.
- Phase Discontinuities: In interferograms layover and discontinuous surface deformation (e.g. at sliding faults or at glacier rock interfaces) cause discontinuities in the interferometric phase.

The algorithm used for unwrapping is SNAPHU which is developed by Stanford university. The detailed discussion about this algorithm is explained in chapter 6. The quality and reliability of unwrapped results very much depends on input coherence. Reliable results can be expected in the areas of high coherence. Although no definite threshold exists a minimum coherence of 0.3 is suggested.

Unwrapping in SNAP follows three distinct steps:

- Export of the wrapped phase (and definition of the parameters)
- Unwrapping of the phase (performed outside SNAP by snaphu)
- Import of the unwrapped phase back to SNAP

Depending on the capabilities of the system, the unwrapping can take a considerable amount of time. However, snaphu supports multi-threading which means that the computation can be distributed over multiple processor cores. This must be defined during the export.

7 Phase to elevation

The unwrapped phase now is a continuous raster but not yet a metric measure.phase to elevation operation coverts radian units into absolute heights.It translates the phase into surface heights along the line of sight(LOS) in metres.The LOS is the line between the sensor and a pixel. A SRTM DEM (see chapter 5) is used to put the elevation values in the correct level.

8 Terrain correction

Terrain correction will geocode the image by correcting SAR geometric distortions using a digital elevation model and producing a map projected product. Geocoding coverts an image from slant range or ground range geometry to a map coordinate system Terrain geocoding involves using a Digital elevation model ro correct for inherent geometric distortions, such as foreshortening, Layover and shadow as shown in below Figure 3.20. More information on these effects refer to ESA radar course materials.
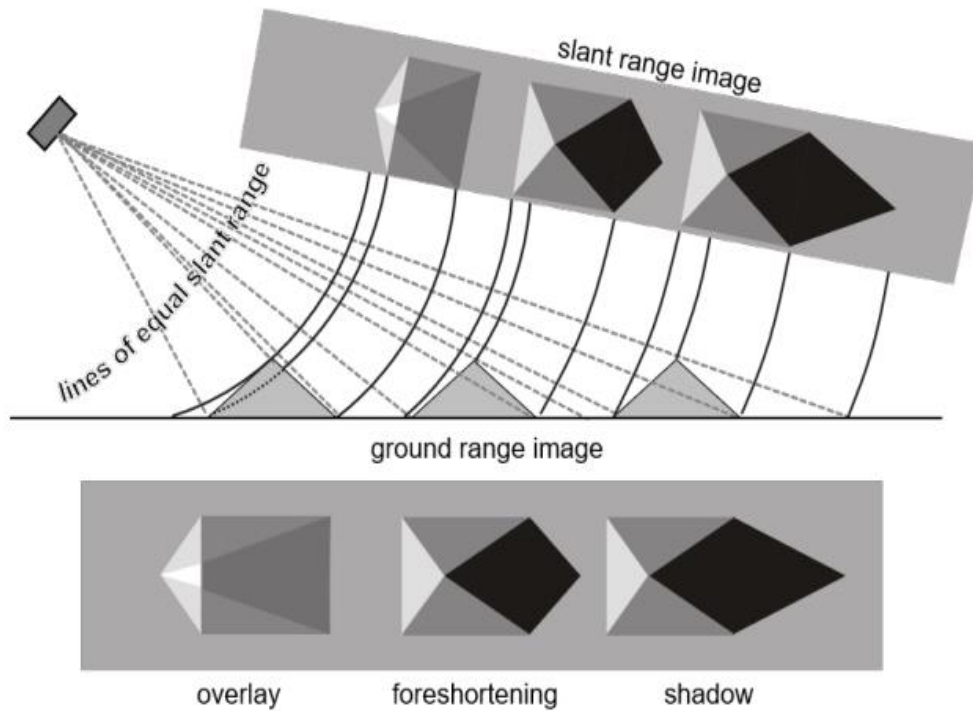
Figure 3.20 Geometric distortions in radar images

3.6 Data model

A geographic data model, geospatial data model, or simply data model in the context of geographic information systems (GIS), is a mathematical and digital structure for representing phenomena over the Earth. Generally, such data models represent various aspects of these phenomena by means of geographic data, including spatial locations, attributes, change over time, and identity. For example, the vector data model represents geography as collections of points, lines, and polygons, and the raster data model represent geography as cell matrices that store numeric values. Data models are implemented throughout the GIS ecosystem, including the software tools for data management and spatial analysis, data stored in a variety of GIS file formats, specifications and standards, and specific designs for GIS installations.

Vector data format

A vector dataset (sometimes called a feature dataset) stores information about discrete objects, using an encoding of the vector logical data model to represent the location or geometry of each object, and an encoding of its other properties that is usually based on relational database technology. Typically, a single dataset collects information about a set of closely related or similar objects, such as all the Lakes in a city as shown in Figure 3.18. In addition to the

geometry of each object, a vector dataset must also be able to store its attributes. For example, a database that describes lakes may contain each lake's depth, water quality, and pollution level. Since the 1970s, almost all vector file formats have adopted the relational database model, either in principle or directly incorporating Relational Database Management system software. Thus, the entire dataset is stored in a table, with each row representing a single object that contains columns for each attribute [91]. Vector datasets usually represent discrete geographical features, such as people, buildings, trees, and counties. However, they may also be used to represent geographical fields by storing locations where the spatially continuous field has been sampled. Sample points (e.g., weather stations and sensor networks), Contour lines and triangulated irregular networks (TIN) are used to represent elevation or other values that change continuously over space. TINs record values at point locations, which are connected by lines to form an irregular mesh of triangles. The face of the triangles represent the terrain surface. Some vector formats commonly used are Shapefile – a popular vector data GIS format, developed by Esri, Keyhole Markup Language (KML) – XML based open standard (by OpenGIS) for GIS data exchange etc.
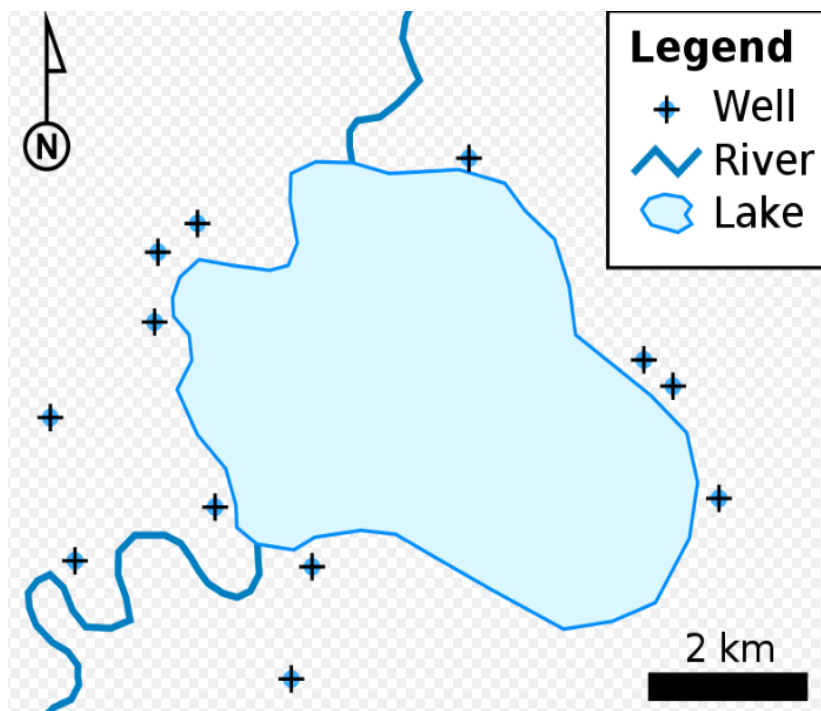
Figure 3.21 A Vector shape file with different attributes such a river lake and well

Raster data format

Like any digital image, raster GIS data is based on a regular tessellation of space into a rectangular grid of rows and columns of cells (also known as pixels) as shown in Figure 3.6, with each cell having a measured value stored. The major difference from a photograph is that the grid is registered to geographic space rather than a field of view. The resolution of the raster data set is its cell width in ground units. Because a grid is a sample of a continuous space, raster data is most commonly used to represent geographic fields, in which a property varies continuously or discretely over space. Common examples include remote sensing imagery, terrain/elevation, population density, weather and climate, soil properties, and many others. Raster data can be images with each pixel (or cell) containing a colour value. The value recorded for each cell may be of any level of measurement, including a discrete qualitative value, such as land use type, or a continuous quantitative value, such as temperature, or a null value if no data is available. While a raster cell stores a single value, it can be extended by using raster bands to represent RGB (red, green, blue) colours, colormaps (a mapping between a thematic code and RGB value), or an extended attribute table with one row for each unique cell value. It can also be used to represent discrete Geographic features, but usually only in exigent circumstances. Raster data is stored in various formats; from a standard file-based structure of TIFF, JPEG, etc to Binary large object (BLOB) data stored directly in a relational database management system (RDBMS) like other vector-based feature classes. Database storage, when properly indexed, typically allows for quicker retrieval of the raster data but can require storage of millions of significantly sized records.

Advantages and disadvantages of raster data and vector data

There are some important advantages and disadvantages to using a raster or vector data model to represent reality:

- Raster datasets record a value for all points in the area covered which may require more storage space than representing data in a vector format that can store data only where needed.
- Raster data is computationally less expensive to render than vector graphics
- Combining values and writing custom formulas for combining values from different layers are much easier using raster data.

- There are transparency and aliasing problems when overlaying multiple stacked pieces of raster images.

- Vector data allows for visually smooth and easy implementation of overlay operations, especially in terms of graphics and shape-driven information like maps, routes and custom fonts, which are more difficult with raster data.

- Vector data can be displayed as vector graphics used on traditional maps, whereas raster data will appear as an image that may have a blocky appearance for object boundaries. (depending on the resolution of the raster file).

- Vector data can be easier to register, scale, and re-project, which can simplify combining vector layers from different sources.

- Vector data is more compatible with relational database environments, where they can be part of a relational table as a normal column and processed using a multitude of operators.

- Vector file sizes are usually smaller than raster data, which can be tens, hundreds or more times larger than vector data (depending on resolution).

- Vector data is simpler to update and maintain, whereas a raster image will have to be completely reproduced. (Example: a new road is added).

- Vector data allows much more analysis capability, especially for "networks" such as roads, power, rail, telecommunications, etc. (Examples: Best route, largest port, airfields connected to two-lane highways). Raster data will not have all the characteristics of the features it displays.

Digital elevation model (DEM)

A digital elevation model (DEM) or digital surface model (DSM) is a 3D computer graphics representation of elevation data to represent terrain or overlaying objects, commonly of a planet, moon, or asteroid. A "global DEM" refers to a discrete global grid. DEMs are used often in geographic information systems (GIS) and are the most common basis for digitally produced relief maps. A digital terrain model (DTM) as shown in Figure 3.19 represents specifically the ground surface while DEM and DSM may represent tree top canopy or building roofs. While a DSM may be useful for landscape modelling, city modelling and visualization applications, a DTM is often required for flood or drainage modelling, land-use studies, geological applications, and other applications.
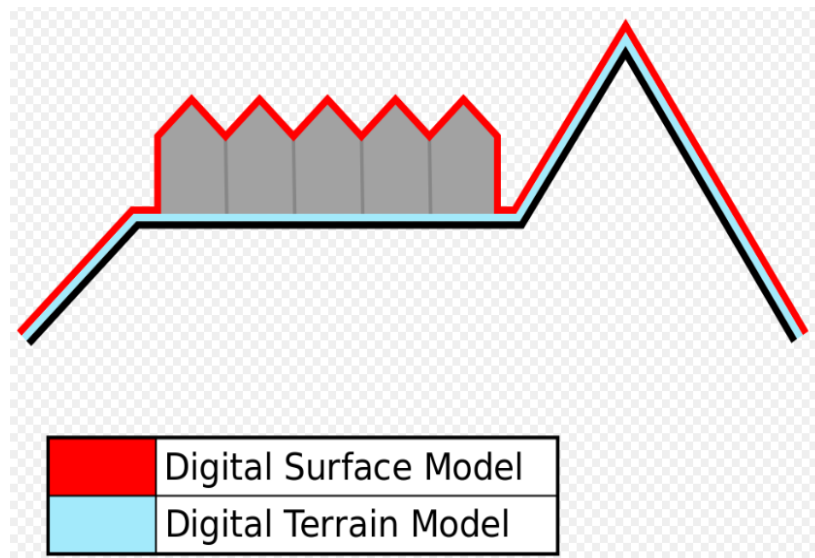
Figure 3.22 Digital Terrain model includes only the bare earth surface whereas digital terrain model includes the physical entities above the earth surface such a buildings trees etc.

A DEM can be represented as a raster (a grid of squares, also known as a heightmap when representing elevation) or as a vector-based triangular irregular network (TIN). The DEM could be acquired through techniques such as photogrammetry, LiDAR, or InSAR, land surveying, etc. (Li et al. 2005). DEMs are commonly built using data collected using remote sensing techniques, but they may also be built from land surveying.

3.7 Alternate Solutions

The main disadvantage of open-source satellite data which I used for our case study (see chapter 6) is, the spatial resolution is very low which is in order of meters and it's very difficult to find a clear cloud over image over belvedere during the end of the glacier period. And there are alternate solutions to create DEM which has very high precision and accuracy but again this will not help in multi temporal analysis because you cant time travel to past to create same quality of DEM in the past wh. The alternate solutions used to produce high resolution Maps, DEM,3D models etc of a specific study area are Photogrammetry and LiDAR. UAV (Unmanned aerial vehicle) lidar and photogrammetry imaging applications are increasing rapidly. This is not surprising as using GNSS enabled UAVs for aerial surveying is very cost effective in comparison to hiring an aircraft with photogrammetry equipment. Because UAVs are relatively inexpensive, organisations will have their own UAV fleet, allowing for rapid surveys over large land areas and infrastructure projects where required. With GNSS equipped

drones, digital cameras and powerful computers, surveys have an accuracy right down to 1 centimetre which is a significant improvement compared to open-source satellite images satellite.

Aerial photography using drones

Aerial photography using drones has become an extremely popular option for surveying and mapping, and it's clear to see why. It's a more accurate, efficient, and reliable alternative to manual inspections and is more cost-effective than LiDAR (Light Detection and Ranging). Photogrammetry is a methodology of making measurements from photographs. The output from photogrammetry is typically a map, a drawing or a 3D model of some real-world object or land mass. Photogrammetry best practice is to have a very clear photos from the drones, if the photos aren't good, then it's going to be difficult to get real quality in your 3D models, no matter how good the software is. If you have Drone see Figure 3.23 with a zoom camera and you zoom in on your aerial photos, are the small features blurry. If so, try to figure out the reason for the blur and your 3D images will improve immensely. Eliminate everything standing in the way of maximum sharpness. This is where more megapixel's matter. Shooting in RAW helps. Lighting is always important in photography. Bright, even lighting will allow you to have a small aperture to reduce the image's depth of field. Shallow depth-of-field is actually a bad thing for photogrammetry because blurred details confuse the software. The goal is to have high detail, sharp, and flat imagery which requires closing the aperture, giving more light. Good lighting will also allow you to lower the ISO, which will reduce grain, and it will allow you to have a high shutter speed which also reduces motion blur.

Figure 3.23 DJI Mavic 2 drones with a transmission range of 4.3 miles (7 km) and a flight time up to 27 minutes, you can cover a lot of ground and this is fitted with 4k stabilized integrated gimbal and camera.

Give the 3D photogrammetry software only high-resolution information. If you are mapping a sculpture or building and don't need the background, then mask it out. If one image is off or not aligning correctly with the images before and after it, then delete this image. Humans are still smarter than software, which will be stitching the images together. Filtering out bad or offline photos before the software gets to work, will make the work of the 3D photogrammetry software easier giving higher image accuracy. If it's not in the picture, then it's not in your mesh and 3D image. Make sure we have the coverage you need to get all the details you want, because it's difficult to go back and re-shoot in the exact same conditions. But we need to georeferenced the images according to the standard coordinate system. In the data processing of this thesis the georeferencing of the image is done using some time invariant points since it is a multi-temporal analysis but there are more accurate methods to geo-reference the images.

Ground Control Points (GCPs)

Ground control points (GCPs) are points on the surface of the earth of a known location. GCPs are tied in during data processing to georeferenced images from a project and convert ground coordinates of the points to real world locations. To put it plainly, GCPs allow the survey drone to obtain accuracy down to a sub-centimetre level, which is very precise. There is one caveat when using GCPs– laying them requires a decent amount of prep work (it can take up to an entire day and a team of people). It's no clean task, especially when working on a huge site with uneven land. Given how tech advances nowadays, newer 'modern' systematic practices, like drone mapping, can become even more simple and less complicated.

GNSS Correction Technology

Before jumping into Real time kinematic/Post processing kinematic technologies and its features, it's necessary to cover GNSS correction technology. GNSS correction technology enhances the quality of location data by using global position system receivers to produce precise, accurate data. It's a technology that's been used with different tools on the ground and on job sites for years. Only recently has it been offered as an add-on to a survey drone for survey-grade photogrammetry. Both GCPs and GNSS Correction Technology possess the ability to produce the same data; however, GNSS Correction Technology doesn't require the same, timely prep work. Today, there are currently two technologies driving the conversation around GNSS correction technology – Real Time Kinematic (RTK) and Post Processing Kinematic (PPK). In that same vein, there's debate on which of the two is a better choice and which you should be looking for to be included on survey drone when looking for a solution. Real Time Kinematic (RTK*)* is a GNNS correction technology technique that provides real-time corrections to location data when the survey drone is capturing photos of a site. Post Processed Kinematic (PPK), another GNSS correction technology technique that works to correct location data, except in the cloud after the drone data has been captured and uploaded. Basically, the main difference between the two is when this positional correcting takes place. RTK corrects during the flight, and PPK corrects after flight. With what we know today, using GNSS correctional technology can improve data gathering by 75%. Additionally, it creates smoother workflows because of that time that is shed. However, it's important to understand

situationally how this all works. Thus prompts the big question — Which one should you choose*?*

Both these technologies are very similar, however, PPK has a decisive advantage — because of its robustness and consistency. Firstly, PPK drones offers more flexibility in terms of the actual flight of the survey drone meaning you have more freedom of how and where the drone is deployed. In contrast, RTK drones requires a very specific base station and other pieces of equipment that work together to process data in real-time. Secondly, a PPK drone can refer to previous and future data relative to the current flight, which creates greater dependability. Having this ability ensures the drone is always on track with the flight. RTK drone has a higher chance of malfunctioning because it cannot retain old or new data to keep the current flight in check. The accountability simply isn't there, which puts accuracy into question. We can take a real-life example if we're on a road trip using GNSS on your mobile device. You might lose signal a couple times but gain it back quickly. PPK operates the same on the job site — if there is an issue with its 'signal' backup data is there to keep the flight on track. RTK does not have this ability; if your mobile device worked with an RTK-equivalent GPS, you'd be lost!

If you're looking to transition from using GCPs to a solution like PPK on your job site, it's a good idea. The flight planning is significantly reduced since you're not spending near the amount of time prepping the job site with ground control points. Make sure you're working with a solution provider that offers PPK as an option so you can make this smooth transition. They'll upgrade you with the type of survey drone conducting the flyover that integrates the product. The PPK drone technology will cost a little more when using a subscription, however, with a drone you'll already have the budget saved. Along with enhancements in time and product, there will also be a change in spirits of the team on the job site. Not having to spend a whole day laying several GCPs is definitely uplifting and creates a more productive team. With all of this considered, it's important to note GCPs still haven't been completely excluded from drone mapping. When working with technologies like PPK, depending on the circumstance, the concept of 'ground control' or 'ground validation' isn't completely irrelevant.

Depending on the size of the site, some ground validation may need to be in place. This allows the survey drone to continue producing a very high level. You're still saving an incredible amount of time when working with PPK and ground validation as opposed to working with GCPs. You may need to lay just 1 ground validation point on the entire job site as opposed to 5 to 8 GCPs. Consider this like a housekeeping task that ensures super precise data. Another

situation in which GCPs carry on applicability is when defending data. Since drone mapping is still a relatively new concept, most of the clients want to see its precision and accuracy. GCPs allow the survey drone to produce a very defensible quality report and really prove the validity of the solution. The post processing of the data collected through drone cameras is done using some commercial softwares such as Agisoft Metashape, photo scan etc.

LiDAR

LiDAR technology can be used in used in multiple ways unlike photogrammetry and Lidar sensors can also pierce dense canopy and vegetation, making it possible to capture bare earth structure which satellites cannot see, as well as ground cover in enough detail to allow vegetation classification and change monitoring. UAV lidar involves mounting a laser scanner see Figure 3.24 on a UAV to measure the height of points in the landscape below the UAV. Lidar means (Light Detection and Ranging). Similarly, we can the mount the laser on a tripod as shown in Figure 3.25 or we also have handheld lidar in the commercial market, their usage depends on our requirement , for example if you want map a glacier we have to use to the UAV LIDAR, where as if we want to collect data of the building for restoration or to verify as build drawings we can use tripod laser scanner and if we need a millimetre level accuracy for a portion of the building then we need to use handheld laser scanner. As we discussed about GCP'S in the previous section of photogrammetry the same GCP's can be used to geo-reference the point clouds captured by the laser scanner.

FIGURE 3.24 OS-1 Aerial LiDAR Where Laser Scanner Mounted on a drone, the Onyx Scan drone is a ultra-light with a Take-Off Weight of only 5.6 kg. This particularity makes it possible to operate both in urban areas and in hard-to-reach zones like mountains valleys glaciers etc.

FIGURE 3.25 Leica P30 3D Laser Scanner 130- metre radius scanning range which has a wide range of applications like safety monitoring of structures through periodic scans and analyse the deformation, wear, and tear of the structure.

3D laser scanning is a construction, engineering, and architectural tool often used to document the existing conditions (as-builts) of any structure or area .3D laser scanners use LiDAR (light detection and ranging) to measure and record precise locations and distances, ultimately producing a point cloud file. These lightweight and mobile scanners produce highly accurate digital measurements and images quickly and easily for use in construction and engineering projects. That data is invaluable in design, prefabrication, asset management, and facility modifications. Precision as-built laser scans have huge benefits for construction companies, and industrial LiDAR scanners are portable, can be automated, and are accurate within millimetres. The primary way a laser scanner works is to send light pulses at high speed which reflect off objects and return to the scanner's sensor (LiDAR). For each pulse, the distance between the scanner and object is measured by determining the elapsed time between the sent and received pulses. Each data point is converted to a pixel with a known x, y, and z coordinate. Laser scans are taken in multiple positions around a site from varying viewpoints. Millions of data points are captured and processed into a point cloud, creating an accurate 3D as built data set of the site. This all happens very quickly, with some scanners, like for example Leica RTC360, capturing and calculating 2 million points per second with 2-4 mm accuracy. The accuracy of the measurements, allow the 3D models created using the lidar drone to be used in planning, design, and decision-making processes across various sectors. The post processing of the data collected through laser scanning is done using some commercial software's such as FARO SCENE, Leica Cyclone etc.

Chapter 4

Hydrological modelling

Computer models, especially conceptual models, are frequently used for catchment hydrology studies. A hydrological model is a simplification of a real-world system (e.g., surface water, soil water, wetland, groundwater, estuary) that aids in understanding, predicting, and managing water resources. Both the flow and quality of water are commonly studied using hydrological models. The main idea of behind this modelling for our case study is to compare the volume lost in the belvedere glacier calculated through the DEM's and compare with the discharge obtained from the hydrological model.

Conceptual modelling uses simplified descriptions of hydrological processes. Such models use storage elements as the main building component. These stores are filled through fluxes such as rainfall, infiltration, or percolation, and emptied through processes such as evapotranspiration, runoff, and drainage. Conceptual models generally have a structure that is specified a priori by the modeler, that is, it is not derived from the observed rainfall–runoff data. In contrast to empirical models, the structure is defined by the modeler's understanding of the hydrological system. However, conceptual models still rely on observed time series of system output, typically stream flow, to derive the values of their parameters during the calibration process. The parameters describe aspects such as the size of storage elements or the distribution of flow between them. Several real-world processes are usually aggregated (in space and time) into a single parameter, which means that this parameter can therefore often not be derived directly from field measurements. Conceptual models make up most models used in practical applications. Most conceptual models consider the catchment as a single homogeneous unit. However, one common approach to consider spatial variability is the segmentation of the catchment into smaller sub catchments, the so-called semi-distributed approach.

One typical example of a conceptual model – Hydrologiska Byråns Vattenbalansavdelning (HBV) – [83] as rainfall–runoff model is given below Figure 4.1`. The HBV model was developed at the Swedish Meteorological and Hydrological Institute (Hydrological Bureau Water balance section). The model was originally developed for Scandinavian catchments but has been applied in more than 30 countries all over the world [84].
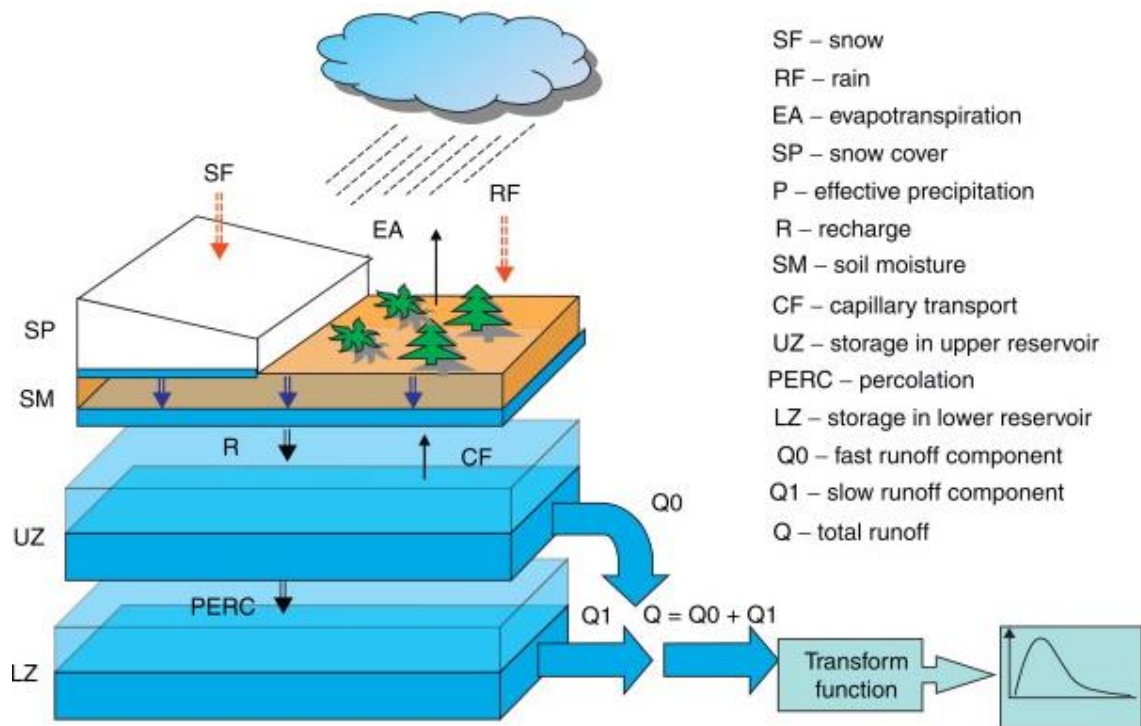
Figure 4.1 Schematic representation of the HBV-96 model with routines for snow, soil, and runoff response. Modified from Lindström G, Johansson B, Persson M, Gardelin M, and Bergström S (1997) Development and test of the distributed HBV-96 hydrological model. *Journal of Hydrology* 201: 272–228.

The runoff generation routine transforms excess water R from the soil moisture zone to runoff. The routine consists of two conceptual reservoirs. The upper reservoir is a nonlinear reservoir whose outflow simulates the direct runoff component from the upper soil zone, while the lower one is a linear reservoir whose outflow simulates the base flow component of the runoff. The total runoff Q is computed as the sum of the outflows from the upper and the lower reservoirs. The total runoff is then smoothed using a triangular transformation function.

Input data are observations of precipitation and air temperature and estimates of potential evapotranspiration. The time step is usually 1 day, but it is possible to use shorter time steps. The evaporation values used are normally monthly averages, although it is possible to use the daily values. Air temperature data are used for calculations of snow accumulation and melt. It can also be used to adjust potential evaporation when the temperature deviates from normal values, or to calculate potential evaporation.

In the early HBV models glaciers are not included in the model routine but in the latest HBV-Light we can include glacier routine to have better representation of mountain hydrology. Glaciers play an important role in high-mountain hydrology (see chapter 2 for more details). While changing glacier areas are considered of highest importance for the understanding of future changes in runoff, glaciers are often only poorly represented in hydrological models. Most importantly, the direct coupling between the simulated glacier mass balances and changing glacier areas needs feasible solutions.

Glacier melt water is an important contribution to discharge in high-mountain catchments (85;86) and can sustain summer streamflow in many large river basins (87; 88). When modelling the hydrology of such catchments for longer periods (>10 years), the changing glacier area has to be considered, especially when climate change is causing glacier retreat. The simplest approach is to update the hydrological model with an externally simulated glacier extent, but this is unsatisfactory, as the mass balance as simulated by the hydrological model might not agree with the updated glacier extent. The use of coupled glacio-hydrological models allows the glacier extent to be linked directly to the simulated glacier mass balance and is, thus, better suited for modelling catchments with changing glacier areas [92; 93]. However, modelers are faced with the question of which degree of complexity is needed to represent glaciers and glacier evolution in hydrological models. The use of a fully distributed, physically based glacier model that considers mass balance, subglacial drainage, ice flow dynamics etc. is often too data demanding and computationally expensive for use in a combined glacio-hydrological model where the non-glacierized part of the catchment also has to be considered. Furthermore, many semi-distributed hydrological models use simplified representations of catchment hydrology using a limited number of conceptual buckets (reservoirs) and coupling such a model with a more complex glacier model would lead to a mismatch in degree of physical and spatial representation. Hence, for hydrological modelling studies there is a need for glacier models that use a similar degree of complexity and data demand as other components of the hydrological model, but which are still able to represent the important glacier processes. Recently an increasing number of hydrological models have incorporated glacier evolution models, using for example an equilibrium line altitude (ELA) shift [94], volume-area (V-A) scaling [95], V-A scaling and morphological image analysis (96), other simple schemes without ice flow [97], or more complex approaches focusing on glacier modelling [98]. One approach with limited glacier input data requirements, which is mass-conserving and well suited for hydrological modelling studies, is the Δh-parameterization,

which describes the spatial distribution of the relative change in glacier surface elevation in response to a change in mass balance [99]. Initially, Huss et al. (2008) introduced the Δh-parameterization as part of their Glacier Evolution Runoff Model (GERM), while a more detailed presentation of the approach, including the derivation of generalized empirical functions applicable to unmeasured glaciers, is given in Huss et al. (2010). Since then, the Δh-parameterization has been applied in global scale modeling by Huss and Hock (2015) as well as in numerous studies applying GERM to simulate individual glaciers or glacierized regions in the Swiss Alps [100;101;102;103;104] and in Central Asia [105]. Several other glacio-hydrological models were coupled with glacier retreat simulations following the Δh-approach (106;107;108;109;110;111). However, details on its practical implementation into the respective conceptual hydrological models have been provided by only few studies, for instance those by Li et al. (2015) and Duethmann et al. (2015). As the Δh-parameterization is based on an empirical approximation to describe glacier retreat, it is subject to uncertainty and several limitations in terms of accurate glaciological modelling at the scale of individual glaciers [99;108;111]. Nevertheless, for the purpose of transient hydrological modelling, particularly for regional studies covering large samples of glacierized catchments, the Δh-approach represents an efficient state-of-the art alternative to more complex glacier evolution models [99;112]. Originally, Huss et al. (2010) derived the Δh-parameterization for periods dominated by negative mass balances and glacier retreat. The missing representation of glacier advance is related to uncertainties in regions with indications for a presence of recent glacier advance [109]. Moreover, it represents a major drawback for long-term hydrological modeling covering past periods, for example with positive mass balance in the European Alps during the 1970s.

Chapter 5

Digital Elevation Model (DEM) generation using very high-resolution stereoscopic satellite images.

There are various techniques to generate a DEM for the study area we are interested in:

Here we are going to discuss two important approaches for a DEM generation using high resolution optical scenes and using radar satellite imagery.

5.1 DEM generation using stereoscopic optical scenes.

There are different high resolution optical satellite data available in the world as shown in the table 4.1 but most of platforms does not make the data available as an open source we need to pay for their services in order to download and use the scenes for our region of interest from the desired satellite platform, but one of the objective of this thesis is to verify the reliability of the open source commercial data which is readily available for usage to generate the DEM for belvedere glacier for a multitemporal analysis of the glacier.

ID	Satellite	Country/ company	Date of launch	Resolution (m)	Swath Width(km)	Mission	Stereo	B/H
1	IKONOS-2	USA/ GeoEye	24 Sep 1999	Pan(N) 0.8 MS(N) 3.2 Pan-sharpened 0.8-1.0	11*11	Commercial	Along Track	0.54-0.83
2	EROS-A1	Israel/ Image sat	5 Dec 2000	Pan(N) 1.9	14*14	Commercial	Along Track, Across Track	Variable
3	Quick Bird	USA/ Digital Globe	18 Oct 2001	Pan 0.61 MS 2.4	16.5*16.5	Commercial	Along Track	Variable
4	Spot 5	France/ Spot image	4 May 2002	Pan 2.5-5 MS-10 Pan 2.5	60*60	Commercial	Along Track, Across Track	Variable
5	Cartosat-1	India	5 May 2005	Pan 2.5	26*26	Commercial	Along track	0.62

6	ALOS (PRISM)	Japan	24 Jan 2006	Pan 2.5	35*35	Commercial	Along-track triplet of images	1
7	EROS-B1	Israel/ Image sat	25 Apr 2006	Pan 0.7	7	Commercial	Along Track, Across Track	Variable
8	KOMPO-SAT 2	Korea/ KARI	28 July 2006	Pan 1 MS 4	15	Commercial /Military	Across Track	Variable
9	World View -1	USA/ Digital Globe	18 Sep 2007	Pan(N) 0.5	17.6*17.6	Dual (comm-ercial with limitations)	Along Track	Variable
10	World View -2	USA/ Digital Globe	8 Oct 2009	Pan(N) 0.46	48*110	Dual (comm-ercial with limitations)	Along track	Variable
11	GeoEye-1	USA/ GeoEye	6 Sep 2008	Pan(N) 0.5 MS(N) 2	15.2	Commercial	Along track	Variable

Table 5.1 List of contemporary very high-resolution optical satellites of producing stereo images.

So now one of the important question arises what open-source data we can choose for the image processing to study belvedere glacier and the answer lies in the above table where you can see the resolution of images which is 2.5-5 m which was best open data available during the period of 2002 now it is freely available to download at https://spot.cnes.fr/en/spot-world-heritage-0. and more detailed explanation is presented in chapter 5 of the data used from spot 5 platform.

Thierry Toutin is an academic researcher from Canada Centre for Remote Sensing. He has contributed to research in topics Digital elevation model & Synthetic aperture radar. A preliminary version of the 3D multi-sensor physical model developed at the Canada Centre for Remote Sensing was developed for the generation of digital elevation models (DEM) from SPOT-5 HRS in-track stereo images (pixel of 5 m by 10 m). Even if three accurate ground control points (GCPs) were enough to set-up the stereo bundle adjustment, ten stereo GCPs collected from 1:20,000 map were used and the 3D modelling was checked on independent points: errors of 14 m, 9 m and 4.7 m in X, Y et Z were obtained. Since these errors included the feature extraction error, the internal accuracy of the stereo modelling is better than a pixel.

The DEM was then generated using an area-based multi-scale image matching method and 3D semi-automatic editing tools and then compared to LIDAR elevation data with to 0.2-m accuracy. As we have chosen spot-5 images I have done some literature review what are techniques that can used to generate a DEM and what is quality of we can achieve from these images. To obtain stereoscopy with images from satellite scanners, two solutions are possible: (1) the along-track stereoscopy from the same orbit using fore and aft images using HRS stereo camera, as shown in Figure 5.1 and (2) the across-track stereoscopy from two different orbits using HRG [113] as shown in Figure 5.2.
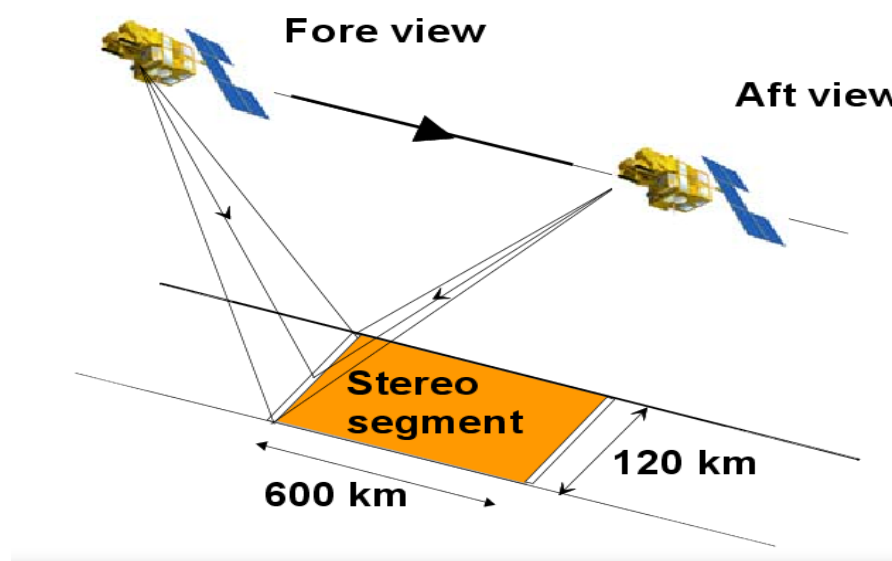
Figure 5.1 Spot 5 HRS Camera capturing the stereo segment in along the track stereoscopy using fore and aft images.
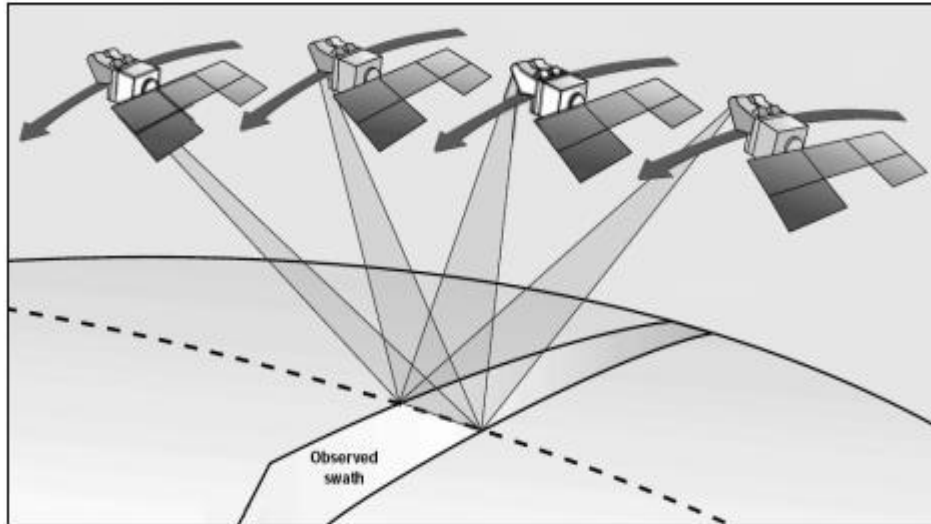
Figure 5.2 SPOT 5 HRG Camera also captures Across-track stereo image acquisition as shown in the schematic diagram the main difference between HRS and HRG stereo image acquisition is the HRS captures the stereo segment in same orbit whereas HRG captures the stereo segment in different orbits.

Since the processing steps of DEM generation using either in-track or across-track stereo images are well known, the six processing steps are summarized in Figure 5.3 [114]:

1.Acquisition and pre-processing of the remote sensing data (images and metadata) to determine an approximate value for each parameter of 3D physical model for the two images.

2.Collection of stereo GCPs with their 3D cartographic coordinates and two-dimensional (2D) image coordinates. GCPs covered the total surface with points at the lowest and highest elevation to avoid extrapolations, both in planimetry and elevation. Ninety-eight and thirty-three GCPs were acquired for in- and across-track stereo-pairs, respectively from 1:20,000 topographic maps (2-3 m accuracy in the three axes). The image pointing accuracy was less than one pixel.

3. Computation of the stereo models, initialized with the approximate parameter values and refined by an iterative least-squares bundle adjustment (coplanarity equations) with the GCPs (Step 2) and orbital constraints. Both equations of collinearity and coplanarity are used as observation equations and weighted as a function of input errors. Theoretically three accurate

GCPs are enough to compute the stereo model, but more GCPs were acquired either to have an overestimation in the adjustment and to reduce the impact of errors or to perform accuracy tests with independent check points (ICPs).

4.Extraction of elevation parallaxes using multi-scale mean normalized cross-correlation method with computation of the maximum of the correlation coefficient. This method gave good results and was commonly used with satellite VIR images (Gülch, 1991).

5.Computation of XYZ cartographic coordinates from elevation parallaxes (Step 4) using the previously computed stereo-model (Step 3) with 3D least-squares stereo-intersection; and

6.Generation of regular grid spacing with 3D automatic and 3D visual editing tools: automatic for blunders removal and for filling the small, mismatched areas and visual for filling the large, mismatched areas and for the lakes.

Figure 5.3 Flow chart of the Processing steps for the generation of DEMs from stereo-images and their evaluation with LiDAR data.

Chapter 6

CASE STUDY

The Belvedere Glacier (Italian: Ghiacciaio del Belvedere) is a valley glacier located above Macugnaga of the Valle Anzasca in the region of Piedmont as shown in below Figure 6.1. The glacier lies at the base of the east face of Monte Rosa. It reaches approximately 2,200 metres above sea level at its highest point and terminates near the Alpe Burki at about 1,800 metres. The glacier is mostly covered by rocks.The glacier is fed by the snows and glaciers on the east side of Monte Rosa, including the Ghiacciaio del Monte Rosa, not to be confused with the Monte Rosagletscher on the Swiss west side, culminating above 4,500 metres, and also the Ghiacciaio Nord delle Loccie on the north side of the Punta delle Loccie (3,497 m).

Figure 6.1 Belvedere glacier: overview map (UTM projection, Zone 32N, Datum ETRF2000)[115]

The glacier is different from normal alpine glaciers since dark glacier it is moronic site not very stable. They are in Northwest region of Italy near Switzerland border historically belvedere glacier is very unstable caused some extreme events in the past and its very risky to go for glacier expedition on site. Belvedere Glacier is a typical debris-covered glacier [116]. The tongue is almost completely covered with debris. The glacier virtually lacks a true accumulation basin and is fed mostly by avalanches flowing down from the eastern face of Monte Rosa, the highest face in the Alps [117]. Due to this peculiar nature of the glacier a team from Politecnico di Torino Glaciology Lab in 2019 went for an onsite expedition of the glacier using Drones, UAV to gather data and they even used a helicopter, fixed with high resolution camera and with the help of professional pilot they were able to gather the data at the top portion of glacier which is at 2200 metres to gather the data which was used to obtain high quality DEM of 20 cm and a ortho photo of 15cm of the glacier as shown in below Figure 6.2 and this DEM will be used to georeferenced the images of spot 5 which will be discussed in chapter 7.

Figure 6.2 Orthophoto of belvedere glacier of 15cm resolution generated by Politecnico di Torino glaciology lab in 2019 using Drones and UAV and Photogrammetry techniques and Lidar.

Data used for DEM generation using Very high-resolution optical satellite images.

Spot 5 images

To calculate the volume lost in the glaciers over a period of time we can use satellite images to generate a DEM (See chapter 2 section 2) at different time intervals at the end of the glacier period. we need to define certain conditions to download a certain satellite image. Two conditions are followed to select the images the first condition is look for the images during the end of the glacier period which is typically during August and September in Europe where you don't have new snow fall on the glacier you just have melting of the glacier during the summer and the second condition is the have a least cloud coverage in the available data.

Data used from SPOT 5 archive (https://regards.cnes.fr/user/swh/modules/60) for belvedere glacier analysis .

- **001-002_S5_054-257-1_2003-08-03-10-35-53_HRG-2_A_DT_TT**
- **004-006_S5_054-257-0_2003-09-24-10-35-37_HRG-2_A_DT_TT**

The above images are in panchromatic band with a resolution of 5m which is very high quality back in 2003.You can see in the file name of the images these are HRG images so we are going to use across the track stereoscopic technique which was explained in chapter 4 since these images are from two different days i.e. 8 August 2003 and 24 September 2003 as shown in Figure 5.3 .For my study area which is defined in Figure 5.3 I could not take advantage of spot 5 HRS camera which was discussed in chapter 3 section** because I could not find a clear cloud free image for my study area.

Note: **HRG**: High Resolution Geometry, **HRS**: High Resolution Stereoscopic
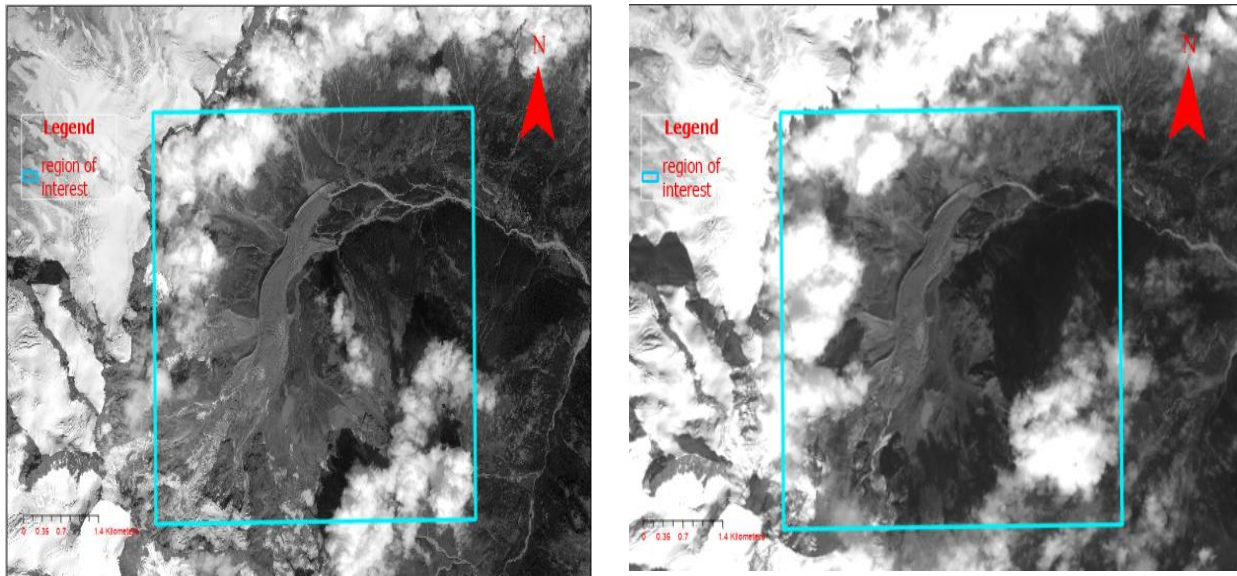
Figure 6.3 spot 5 panchromatic images of the belvedere glacier which are taken from HRG instrument with a 5m resolution which has our study area belvedere glacier during the end of glacier period in 2003 and Aug 8 and September 24 respectively.

Data used from sentinel 1 data base.

To select images that can used for InSAR data processing for DEM we need to have a Suitable perpendicular baseline: The distance between the satellites' positions at the time of image acquisition should be between 150 and 300 meters []. If the perpendicular is too small, these topographic effects on the differential phase are not pronounced enough. With too large baselines, the coherent phase is increasingly different, also leading to decorrelation and even temporal base line also should in the data downloaded for this analysis this both criteria is satisfied.

Data used during the analysis from Aug 10, 2019, and August 16, 2019, this can be downloaded for free from the Copernicus website.

- **S1A_IW_SLC__1SDV_20190810T172327_20190810T172354_028510_033918_77 90**
- **S1B_IW_SLC__1SDV_20190816T172238_20190816T172305_017614_021234_6E 55**

Since the about data area Single Look Complex products have spatial resolutions that depend on acquisition mode. Different acquisition modes are already explained in chapter 3 sentinel 1 section and the mode we interest in for our data processing is IW which has a resolution(range*azimuth) of 2.7x22 m to 3.5x22 m and a Pixel spacing of 2.3x14.1 m.

Shapefiles from ARPA Piemonte

In order to understand the discharge in the valley shapefiles baci base shapefile from the Piemonte region was used as these represents the administrative boundaries of the region as shown in below Figure 5.8, the Anza Alto Torrente region is the valley location of belvedere glacier.

Gauges in the region

In the order to calculate the discharge in the valley we need the daily temperature and precipitation data of the study area. This is data can downloaded from the http://www.arpa.piemonte.it/ website and you can see in the point shape file in our area of interest for the stimulation of the HBV model the gauges which has daily temperatures and precipitation data as shown in the Figure 5.8 which fall in our study area are used you can see some of the gauges are outside the study area but an approximation has been made even the nearby gauges around the valley are considered to run the hydrological model..

Belvedere Glacier shape

The shape of the glacier cannot extracted from the satellite images of spot 5 directly so I have used the data from Glacier Land Ice Monitoring from Space(GLIMS) website http://www.glims.org/ which is managed by NASA has a repository of all the glaciers in the world at different time periods so in order to calculate the volume of the glacier in 2003 from the DEM generated from spot 5 image processing which you will see in detail in chapter 6 this shape file will be used to outline the glacier in the valley as shown in the below figure 5.8.
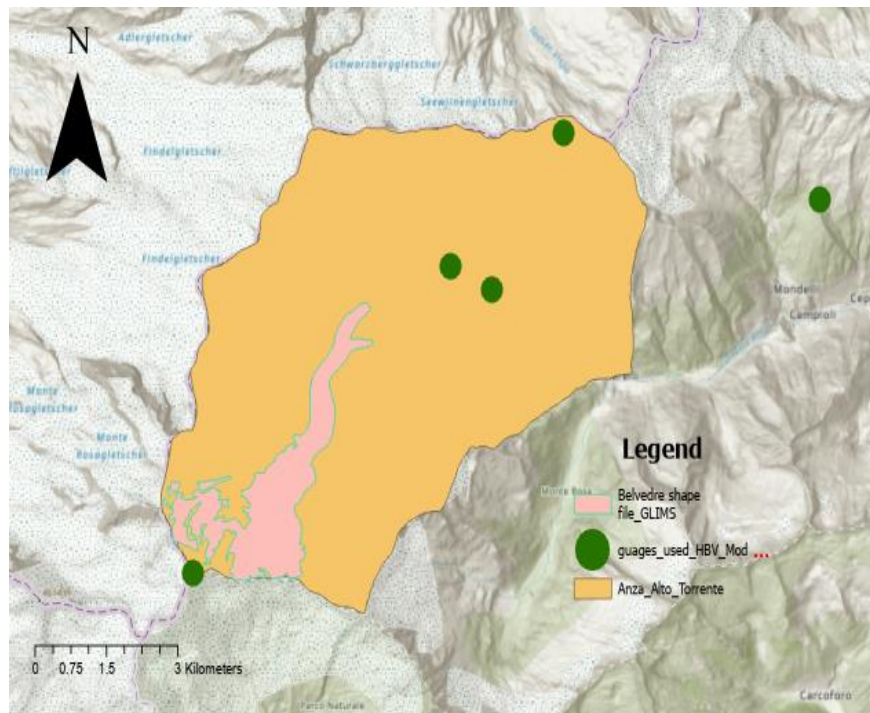
Figure 6.4 The Belvedere_shape_Glims is the Belvedere glacier shape in 2003 the analysis of this shapefile is done by Dr.Paul frank from University of Zurich-Irchel Department of Geography, Glaciology and Geomorphodynamics Group. Green dots are the Gauge stations which fall near our study area and the Anza alto torrente is administrative boundary derived from the BACI shapefiles from Regione Piemonte .

Digital elevation model DTM 10

This digital elevation model of whole Piemonte contains elevation data of the whole region with 10m and this was published in 2011 and can downloaded from geoportal website of the region. This DEM used to evaluate the accuracy of the DEM generated from the spot 5 images as show described in the flow chart of chapter Figure 5.3 which you will see in detail in chapter 8.

Corine Land Cover

The CORINE Land Cover (CLC) inventory was initiated in 1985 (reference year 1990). Updates have been produced in 2000, 2006, 2012, and 2018. It consists of an inventory of land cover in 44 classes. CLC uses a Minimum Mapping Unit (MMU) of 25 hectares (ha) for areal phenomena and a minimum width of 100 m for linear phenomena. This is used to

understand land cover of region and to calculate the percentage of land covered of different classes for the simplicity of our analysis in hydrological stimulation 3 classes has been used bare rock, vegetated area, glacier and snow since it's a mountainous region we can make this approximation below Figure 6.5 shows the land cover with different classes of the study area.
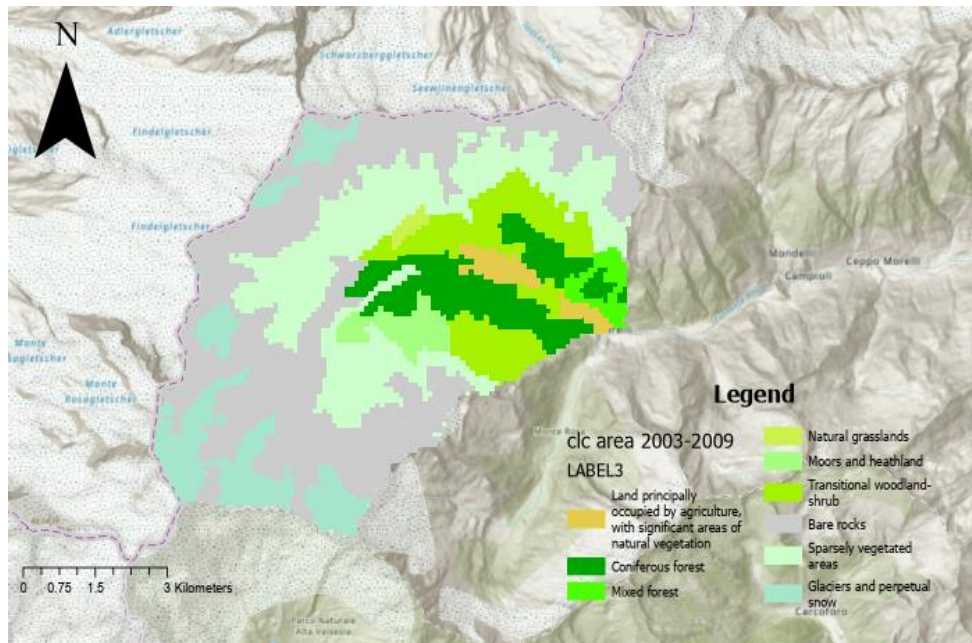
Figure 6.5 Corine land cover usage of the study area in 2012 with 25m geometrical accuracy each colour in the map represents the classification of land use according to Corine land cover classes.

Shuttle Radar Topography Mission DEM(SRTM)

SRTM is DEM with global and is freely available for download from United states geological survey(USGS) Website and specifications of this DEM are reported in the below Table 5.1

Projection	Geographic
Horizontal Datum	WGS84(World Geodetic System 1984)
Vertical Datum	EGM96 (Earth Gravitational Model 1996)
Vertical Units	Meters
Spatial Resolution	1 arc-second for global coverage (~30 meters) 3 arc-seconds for global coverage (~90 meters)
Raster Size	1 degree tiles
C-band Wavelength	5.6 cm

Table 6.1 Specifications of the SRTM that is used in the radar image processing

Chapter 7

Processing of SPOT 5 optical scenes and Sentinel 1 Radar images

The processing of both the images is done in two different image software because the image are completely different. The software's used are Agisoft metashape which needs a professional license and other one SNAP which is an open-source software which is provided by ESA for sentinel data processing.

7.1 Data processing of SPOT 5 optical scenes at the end of the glacier period during the year 2003

Agisoft Meta shape

It is a cutting-edge software solution, with its engine core driving photogrammetry to its ultimate limits, while the whole system is designed to deliver industry specific results relying on machine learning techniques for post-processing and analysis tasks. The software allows to process images from RGB or multispectral cameras, including multi-camera systems, into the high-value spatial information in the form of dense point clouds, textured polygonal models, georeferenced true Ortho mosaics and DSMs/DTMs. Further post-processing enables to eliminate shadows and texture artifacts from the models, calculate vegetation indices and extract information for farming equipment action maps, automatically classify dense point clouds, etc.

Satellite imagery processing is supported with Common processing workflow for panchromatic and multispectral satellite images, provided that sufficiently accurate Rational Polynomial coefficient (RPC) data is available for each image.

Data processing of spot 5 images for the year 2003 at the end of the glacier period for August 8 and September 24

Data used to process in the software.

1. 001-002_S5_054-257-1_2003-08-03-10-35-53_HRG-2_A_DT_TT

2 004-006_S5_054-257-0_2003-09-24-10-35-37_HRG-2_A_DT_TT

The source of this data is already described in chapter 6

The common processing workflow is similar the workflow described in chapter 4 Figure 4.3. But there are 2 challenges in processing the spot 5 images in the software.

1.Data that is downloaded from spot 5 heritage as described in the chapter 5 is a Level 1A product which is not georeferenced, and we need Level 2A product that can be used for processing.

2.And second challenge is the spot 5 images does not have RPC coefficients

To georeferenced the spot 5 images CNES (Centre National D'Etudes Spatiales) provides a service where we can transform the Level 1A image to Level 2A carto for more info about spot 5 images please refer to spot 5 handbook which is available to download for free at CNES website.

The service takes as input SWH (Spot world heritage)-1A product and generates standard ortho-rectified on DEM product (SWH-2A-Carto products) where the altitude and spatial resolution are set up by the processing in a cartographic projection. A metadata file is added to the product. If a pair of SPOT 5 THR images is provided as input, a supermode processing (fusion of two images at 5 m GSD (Ground sampling distance) to compute a more resolved image at 2.5m GSD) followed by a deconvolution (reduction of blur) processing are performed(Latry C. and Rougé B., 1998) as shown in the below Figure 6.1. Ortho-rectification takes only a few seconds to process, supermode+deconvolution takes between 3 and 4 minutes.
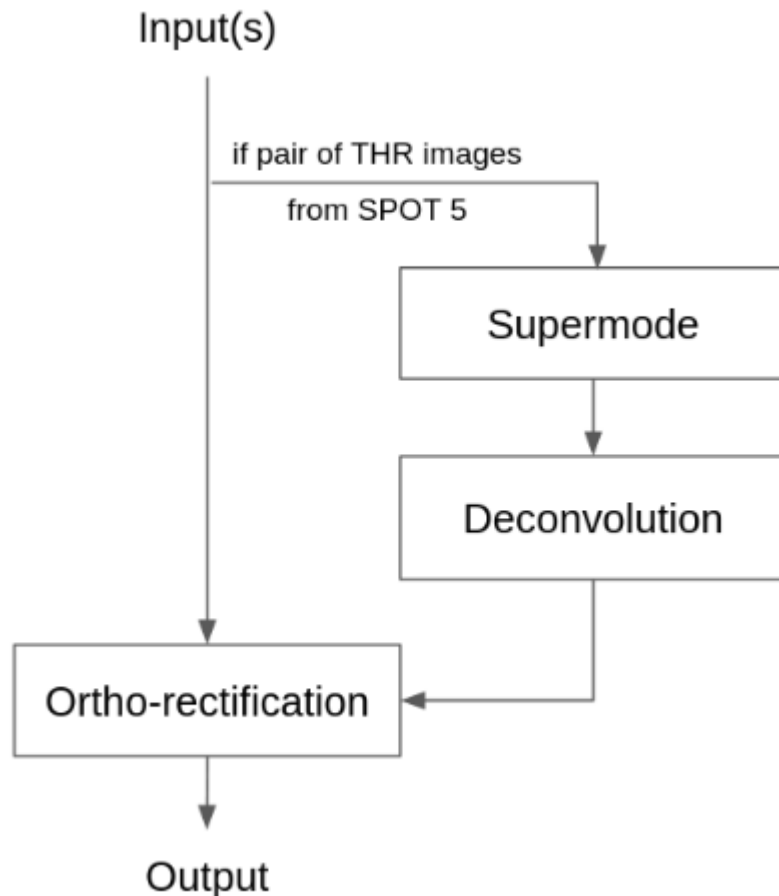
Figure 7.1 spot 5 level 1A to level 2A carto process description this can done at the CNES website https://swh-2a-carto.fr/ for free and the output will be delivered to the email immediately.

Input product: SPOT Level 1A

Radiometry:

- Detectors normalization applied (dark current offset and sensitivity gain)
- 8 bit coded – instrument digital counts (no calibration)

Geometry:

- No geometrical correction
- Each line corresponds to a full detector array acquisition (square image)
- Pixel resolution not consistent in the field of view (specially for oblique viewing)

Output product: SPOT Level 1A

Radiometry

- 8 bit coded – instrument digital counts (no calibration)

Geometry

- Data is projected in UTM projection using a world DEM (1km GSD)
- Product orientated with respect to the geographic North.
- Pixel resolution is fixed, defined by the sensor and the satellite in this data processing it is 5m since Panchromatic band spot 5 images are used

As no Ground control points are used in the processing location, performance corresponds to the initial one of the products:

- About 500 m (RMS) for SPOT 1/2/3
- About 200 m (RMS) for SPOT 4
- About 50 m (RMS) for SPOT 5

After transformation from level 1A to Level 2A carto the data of spot 5 which are described in chapter 5 changes to as following:

- 001-002_S5_054-257-1_2003-08-03-10-35-53_HRG-2_A_DT_TT_CARTO
- 004-006_S5_054-257-0_2003-09-24-10-35-37_HRG-2_A_DT_TT_CARTO

Now these images are already projected with respective to geographic north now these are like normal images which you take from a drone or some UAV etc now these images can be processed in the software without any RPC'S but still there is one challenge which needs to tackled that is Ground control points(GCP'S) in the study area since we are processing images in the past dates have highlighted in the file names described in the above section it is impossible to go to the past and mark the GCP'S and tie points in the study area or we don't have any topographic maps which from the past which has this information so an approximation has been considered for this analysis to identify the time invariant points along the boundary of the glacier and on the glacier mass in both the spot 5 images on August 8 2003 and September 24 2003 as shown in Figure 6.2 and figure 6.3 shows the quality of accuracy of the points pixel to pixel comparison in both the images

\
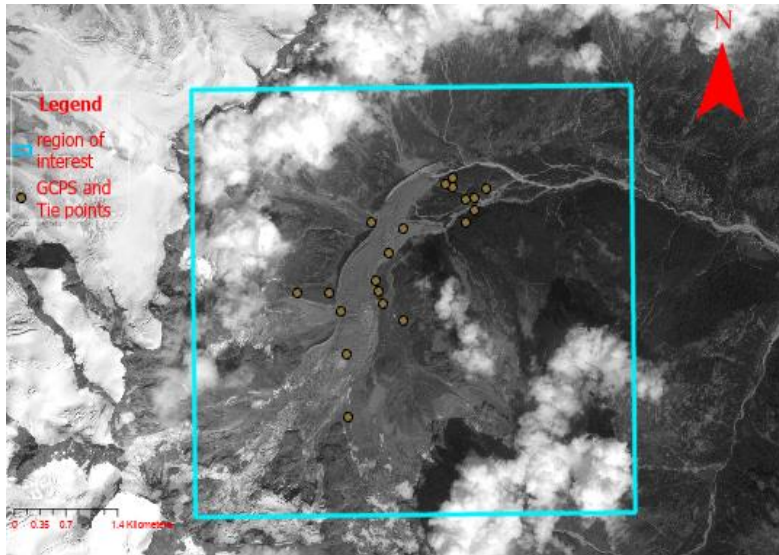
Figure 7.2 spot 5 image panchromatic image with 5m resolution on 24 September 2003 is marked with 20 Ground control points(GCP's) and tie points identified along the glacier and on the glacier on both the images.

This method of selecting time invariant points manually on the glacier is forced approximation due to data unavailability of topographic maps for the region which contains this information. Selecting time invariant points in this region is very difficult because the geomorphology around the glacier changes considerably since it is very unstable.

And the final DEM generated from this analysis is as shown below Figure 6.3
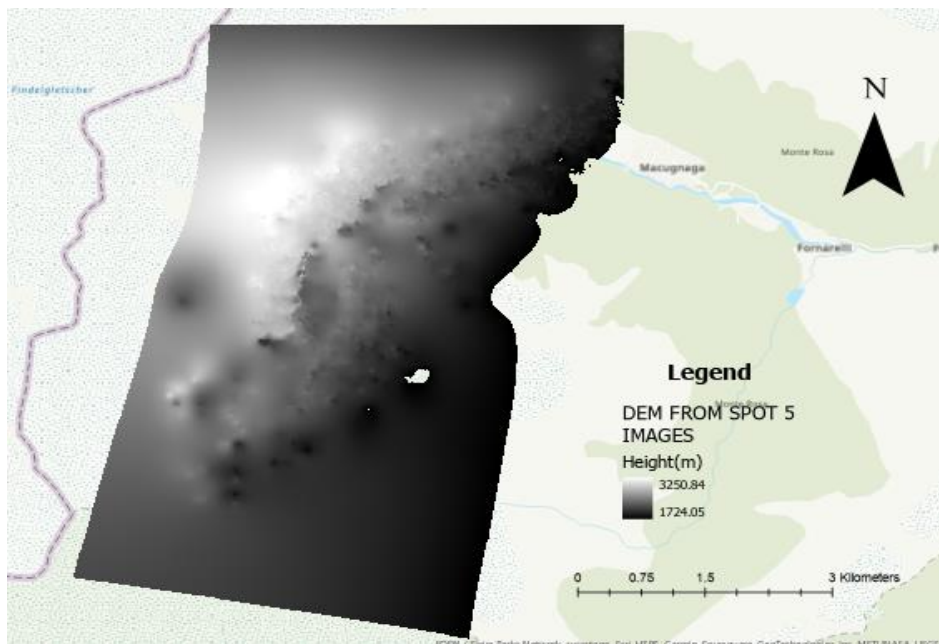
Figure 7.3 We can clearly see in this above there is lot of noise in the final output and RMSE for this DEM is calculated in chapter 9 which shows the quality of this DEM Obtained.

7.2 Data processing of Sentinel 1 Radar images at the end of the glacier period during the year 2019

The software and external packages used for this processing are SNAP and snaphu.

SNAP (Sentinel Application Platform)

A common architecture for all Sentinel Toolboxes is being jointly developed by Brockmann Consult, SkyWatch and C-S called the **Sentinel Application Platform** (SNAP).

The SNAP architecture is ideal for Earth Observation processing and analysis due to the following technological innovations: Extensibility, Portability, Modular Rich Client Platform, Generic EO Data Abstraction, Tiled Memory Management, and a Graph Processing Framework.

Advantages of SNAP

- Common architecture for all Toolboxes

- Very fast image display and navigation even of giga-pixel images

- Graph Processing Framework (GPF): for creating user-defined processing chains

- Advanced layer management allows adding and manipulation of new overlays such as images of other bands, images from WMS servers or ESRI shapefiles.

- Rich region-of-interest definitions for statistics and various plots

- Easy bitmask definition and overlay

- Flexible band arithmetic using arbitrary mathematical expressions

- Accurate reprojection and ortho-rectification to common map projections,

- Geo-coding and rectification using ground control points.

- Automatic SRTM DEM download and tile selection

- Product library for scanning and cataloguing large archives efficiently.

- Multithreading and Multi-core processor support

- Integrated World Wind visualisation

SNAPHU(Statistical-Cost, Network-Flow Algorithm for Phase Unwrapping**)**

As discussed in the chapter 3 during the sentinel 1 data processing steps we need a external plugin for unwrapping the wrapped interferogram that is generated from the radar images that are used for the processing (see chapter 5). Two-dimensional phase unwrapping is the process of recovering unambiguous phase data from a 2-D array of phase values known only modulo 2π radians. SNAPHU is an implementation of the Statistical-cost, Network-flow Algorithm for Phase Unwrapping proposed by Chen and Zebker. This algorithm poses phase unwrapping as a maximum a posteriori probability (MAP) estimation problem, the objective of which is to compute the most likely unwrapped solution given the observable input data. Because the statistics relating the input data to the solution depend on the measured quantity, SNAPHU incorporates three built-in statistical models, for topography data, deformation data, and smooth generic data. The posed optimization problem is solved approximately with use of network-flow techniques. As SNAPHU uses an iterative optimization procedure, its execution time depends on the difficulty of the interferogram. After the phase is unwrapped it can be imported to SNAP for further analysis.

Data used during the end of the glacier period in 2019:

- S1A_IW_SLC__1SDV_20190810T172327_20190810T172354_028510_033918 _7790
- S1B_IW_SLC__1SDV_20190816T172238_20190816T172305_017614_021234_ 6E55

The criteria used to select this image is as follows:

- Short temporal baseline which is 6 days (August 10 and August 16) for this pair of images as you can see dates of images which is highlighted in rectangular box for both the file names above.
- Suitable perpendicular baseline: The distance between the satellites' positions at the time of image acquisition should be between 150 and 300 meters [119]. If the perpendicular base line(see Figure 7.4)is too small, these topographic effects on the differential phase are not pronounced enough. With too large baselines, the coherent phase is increasingly different, also leading to decorrelation. The Sentinel-1 mission was mainly designed for the retrieval of deformations (DInSAR) and not for DEM generation [120]. Most of the baselines between two consecutive images are below 30

meters. Image pairs with short temporal baselines and large perpendicular baselines can be hard to find. A helpful tool to identify the baseline of two images and to find suitable image pairs is provided by the Alaska Satellite Facility: ASF Baseline tool. For the above image pair perpendicular base line is 162m as shown in below Figure 6.4.
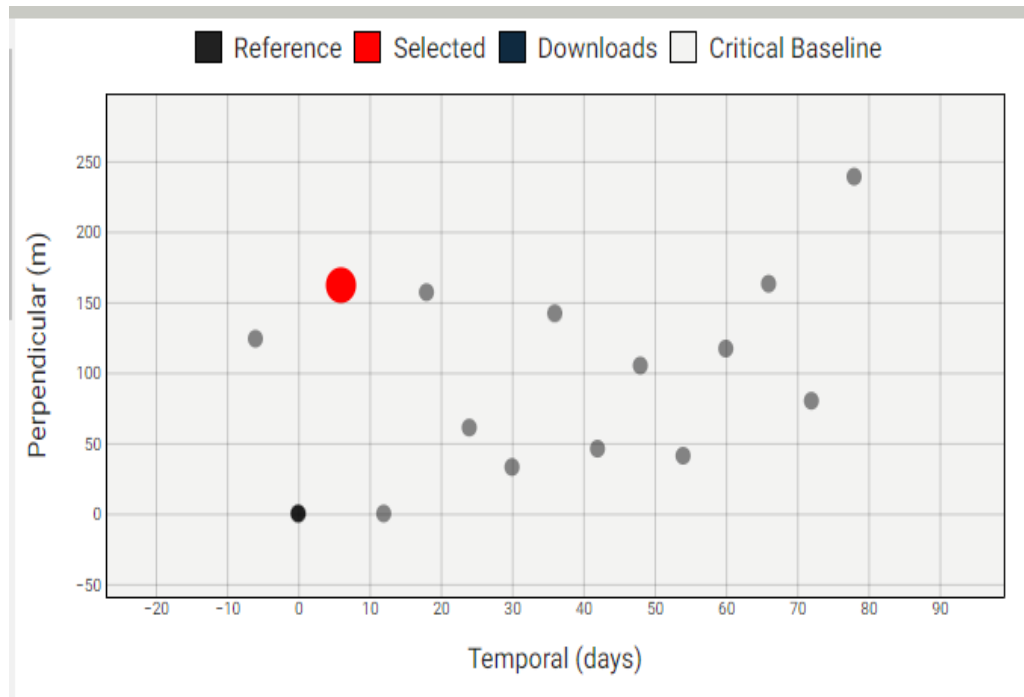
Figure 7.4 The black dot in graph is the reference image (August 10,2019) from the image pair and the red dot refer to the secondary image (August 16,2019) you can clearly see in the above image the perpendicular base line is above 150m and less than 300m.

- Suitable atmospheric conditions: Water vapor in the atmosphere causes phase delays as shown in Figure 7.5 and potentially decreases the quality of the measurement. It is therefore advisable to select images acquired during dry periods and to make sure that no rainfall occurred during both image acquisitions.
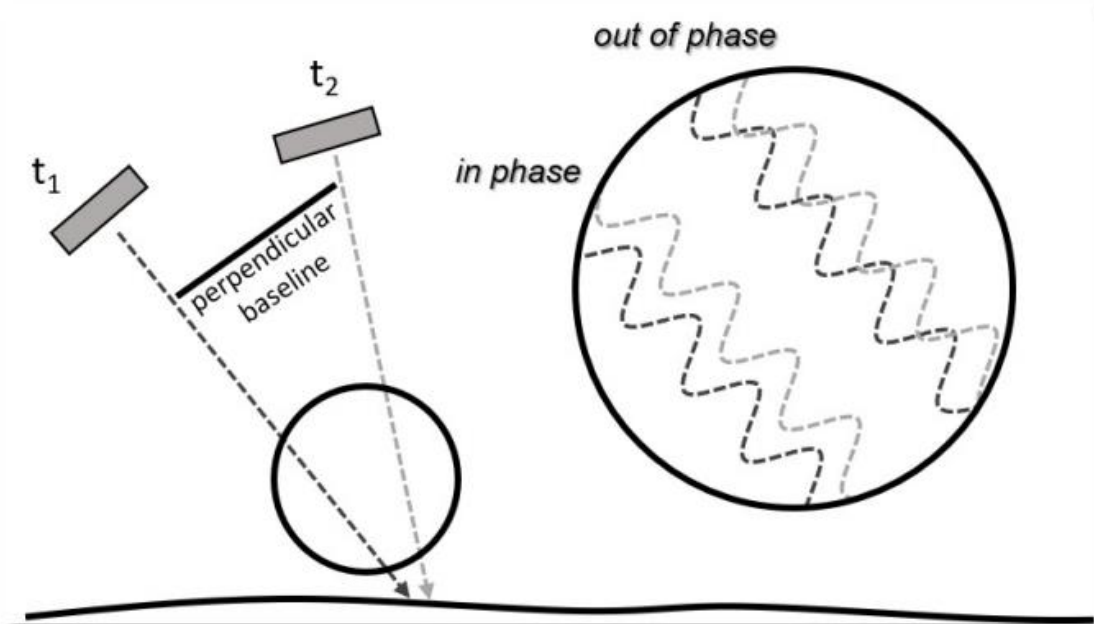
Figure 7.5: Image geometry and phase decorrelation

In order we save the computation time we are not going to process the whole radar images in the SNAP I'm going to confine my analysis just around the belvedere glacier.In chapter 3 the procedure to process the radar images has already been explained in section 3.5 so now we are just going see some intermediate results of the processing because a lot of information about the processing can be observed which should be taken into account before reaching the final output .

Coherence is main tool to judge whether the images are successfully co-registration(see chapter 3 section 3.5) is successfully achieved for both master and secondary image in the below Figure 7.6 you can coherence of both the images after co-registration white shade and black shade of the pixels and histogram of the coherence is plotted as shown in Figure 7.7
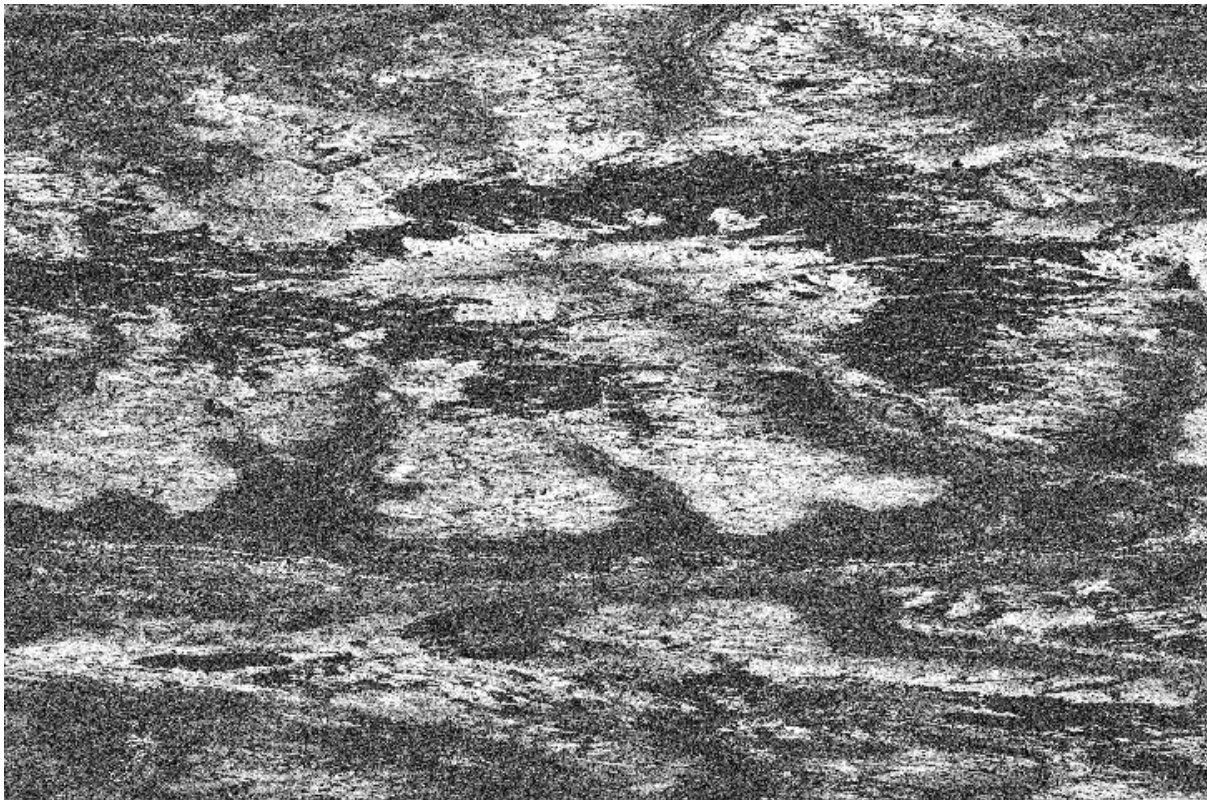
Figure 7.6 coherence is calculated as a separate raster band and shows how similar each pixel is between the secondary and reference images in a scale from 0 to 1 Areas of high coherence will appear bright. Areas with poor coherence appear dark.
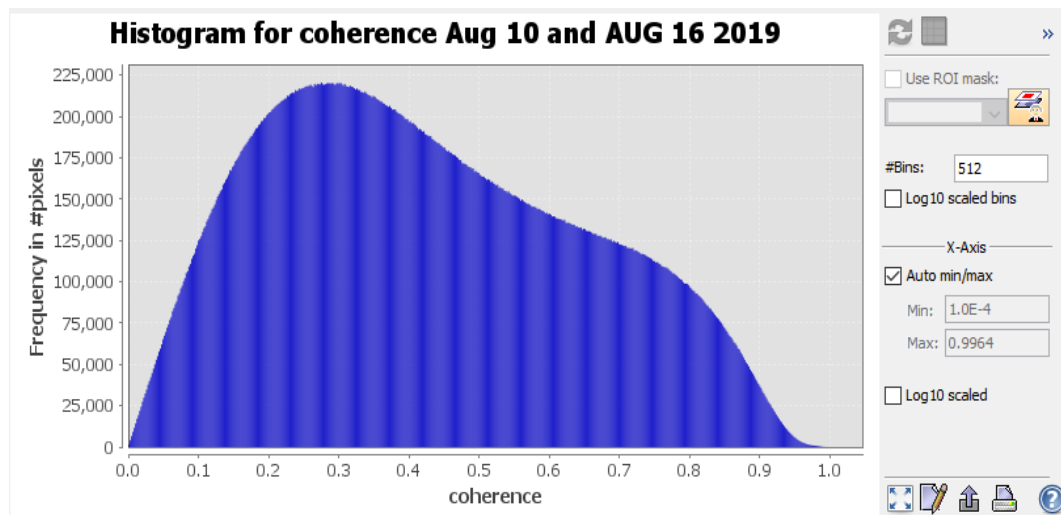
Figure 7.7 There are no specific rules to interpret the coherence generally above 0.6 is considered as high coherence and below 0.3 is considered as low coherence but in this above figure most of the pixel coherence is between 0.3 to 0.6 and also some portion of image has very high coherence, so we might achieve at least a decent quality DEM for belvedere glacier.

Interferogram is displayed in a rainbow colour scale as shown in below Figure 6.10. The patterns also called fringes appear in an interferogram cycles of arbitrary colours with each cycle representing half sensor wavelength.
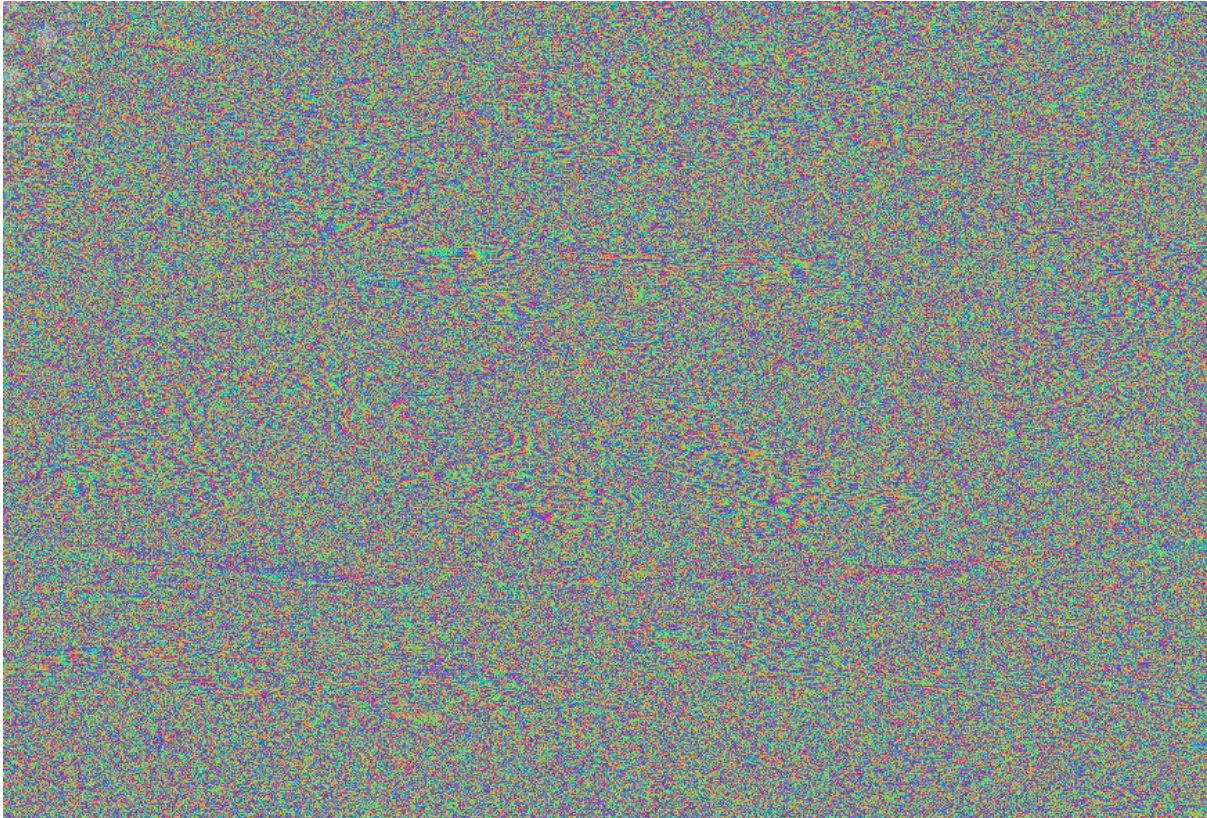
Figure 7.8 Interferogram generated from august 10,2019 and august 16,2019 sentinel 1 images. To derive a DEM of sufficient quality, the fringes in the image must be visible throughout image in the above image it is visible, and area of phase decorrelation (dark pixels in Figure 7.7) appear as a noise in the interferogram.

This interferogram is further refined using Goldstein phase filter (see chapter 3 section 3.5) to reduce the noise of the interferogram as shown in the Figure 7.9
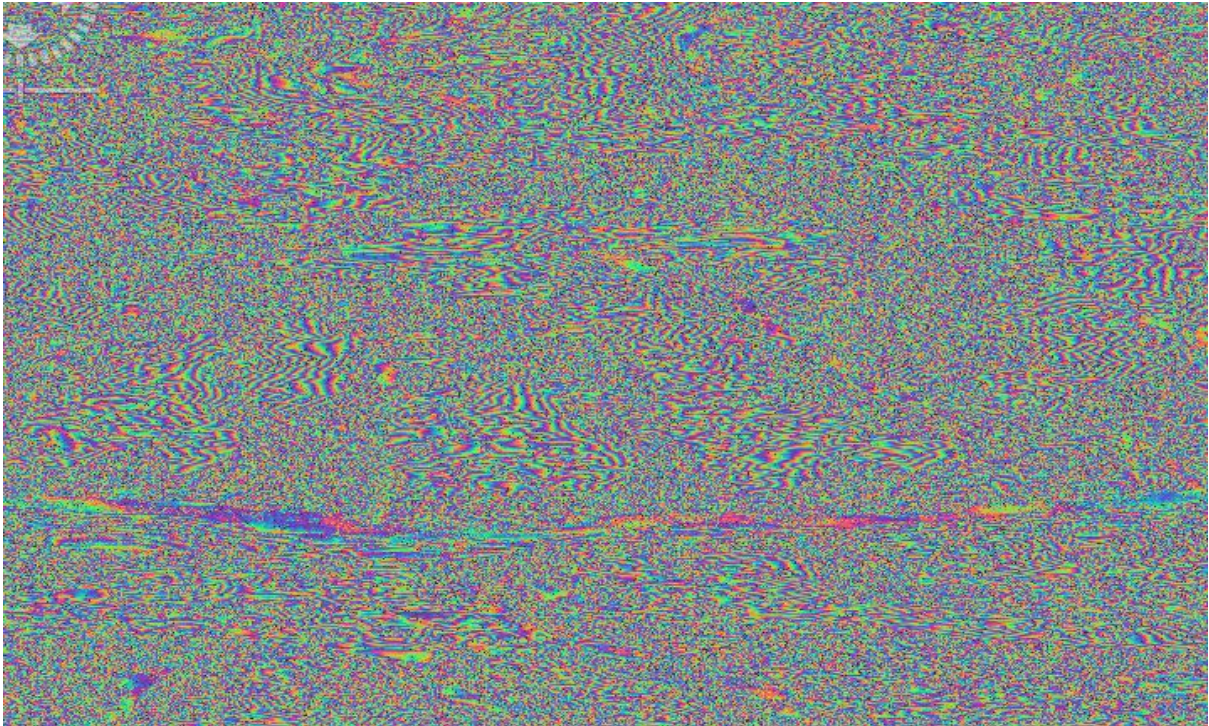
Figure 7.9 Interferogram after Goldstein phase filtering the noise to interferogram greatly reduced compared to unfiltered interferogram as shown in the Figure 7.8

Finally, the interferogram in Figure 7.9 is unwrapped as discussed in chapter 3 section 3. using snaphu and final result is shown in the below Figure 7.10
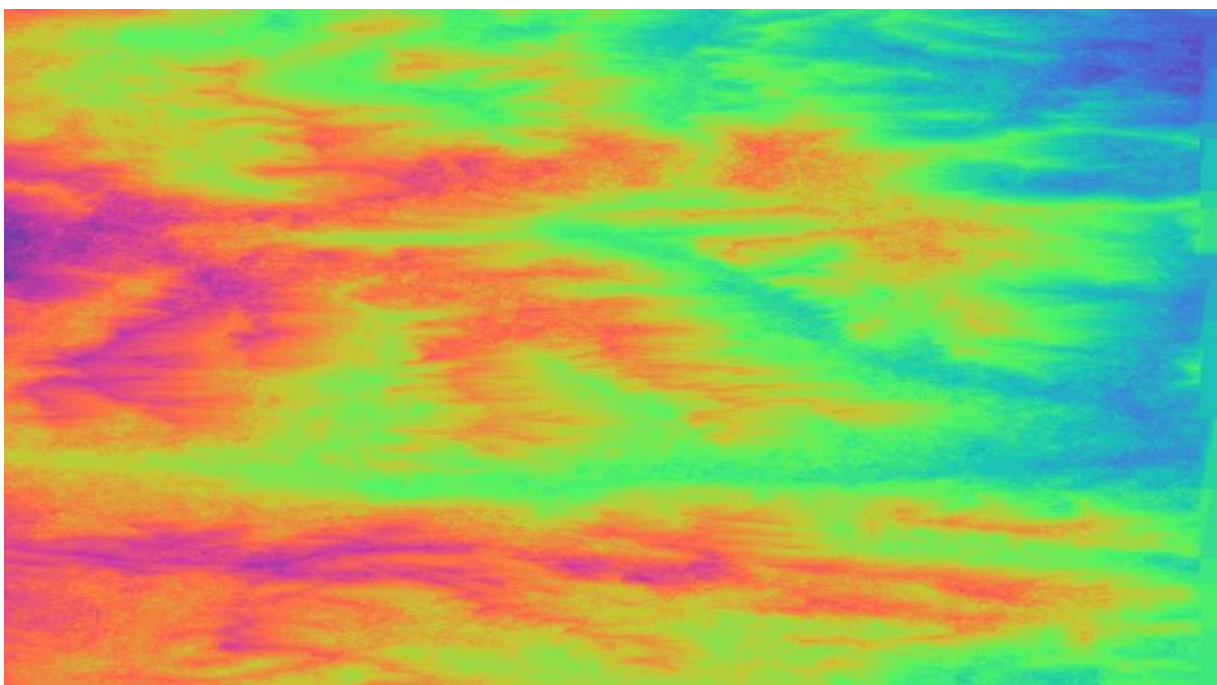
Figure 7.10 After unwrapping of the interferogram is done the restoring of the correct multiple of 2π to each point of the interferometric phase image is complete as shown in Figure 3.19

Finally, this unwrapped phase is converted to metric measure using a reference DEM SRTM (see chapter 6) to put elevations at correct level and then terrain correction is applied to metric measure and finally the DEM is produced and exported as KMZ file as shown in below Figure 7.11 with a quality of 13.91m and the validation of this DEM is done in chapter 9.
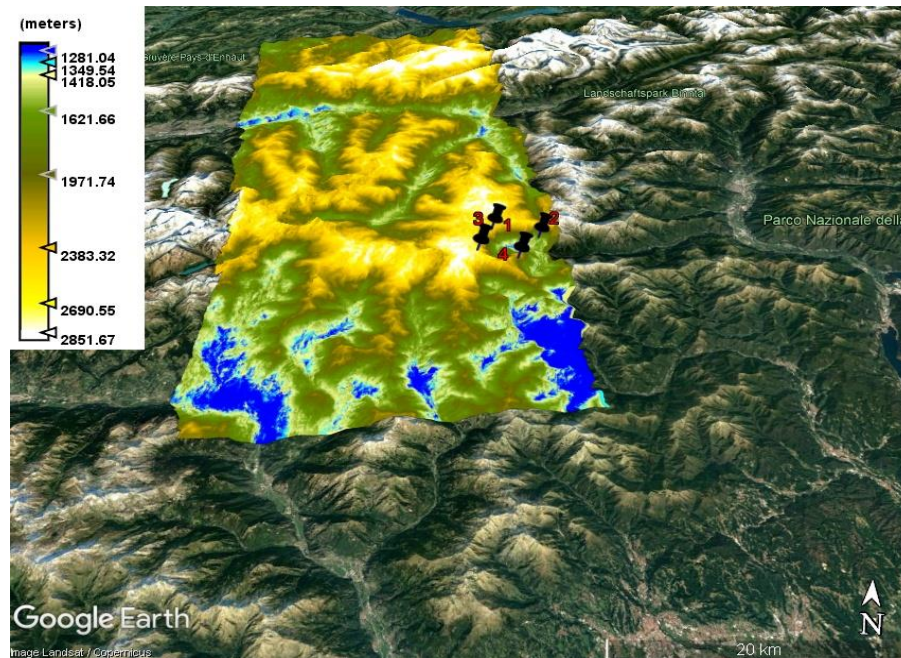
Figure 7.11 DEM generated from the sentinel 1 data around the belvedere glacier at the end of the glacier period in 2019.belevedere glacier falls in inside the area surrounded by pins as shown in the above image.

CHAPTER 8

HBV MODEL STIMULATION FOR BELVEDERE GLACIER

Firstly, lets describe how ice accumulation, melt and glacial runoff are represented in HBV-light before we describe how areal changes of the glaciers are represented. The glacier area within a catchment is conceptually simulated by two reservoirs representing glacier ice and the liquid water contained within the glacier. There can be a snowpack on top of the glacier, which also consists of a solid (snow) and a liquid (water content) reservoir. The snow and glacier routine calculations are performed at each simulation time step for each elevation zone, for which elevation bands of 100 to 200 m are typically used. The elevation zones can be further subdivided according to three aspect classes (N, S, and W/E). Depending on the temperature in relation to the threshold temperature, precipitation falls either as snow or rain. In case of rain, the precipitation is added to the water content of the snow if a snow layer is present or to the water content of the glacier otherwise. If the temperature is above the threshold temperature, melt takes place in the snowpack based on a degree-day factor, and the melted snow is added to the water content of the snowpack. In the case that the water content exceeds the snow water holding capacity, the amount exceeding the snow water holding capacity flows out and is added to the liquid water reservoir of the glacier. If the temperature is below the threshold temperature, part of the water content in the snow layer refreezes.

Preparation of catchment

Elevation and Vegetation zones

HBV model needs a catchment that specifically needs to be prepared for our region of interest that contains elevation zones and Vegetation zones to keep the model simple I have divided the catchment into 2 elevation zones as shown in Figure 8.1 and 3 vegetation zones(bare rocks,snow,trees) from corine land cover as shown in Figure 6.5 Strictly speaking in HBV modelling the final number of zones and vegetation zones must be computed according to final model efficiency in a iterative process.
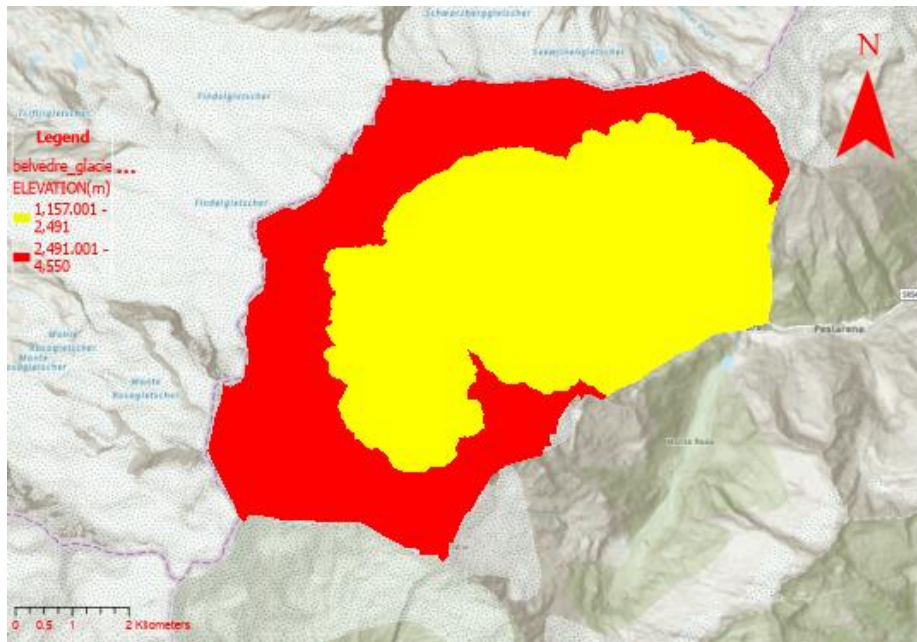
Figure 8.1 DEM(DTM-10) is divided in 2 elevation zones with zone 1 ranging from 1157m-2491m and zone 2 ranging from 2491m-4550m

For glacier modelling we further need the orientation each cell of the catchment and this is computed using Arcgis and Aspect map of the Catchment is generated as shown in Figure
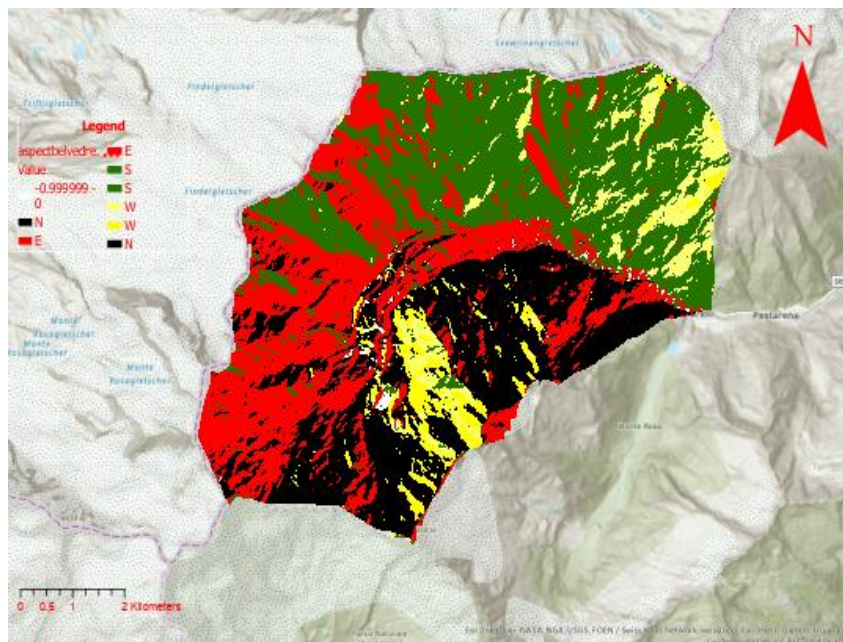
Figure 8.2 Orientation of Catchment in all 4 different directions generated from DTM-10 for each cell of DTM-10 in the catchment.

Combing this both the information with CLC land lover I calculated the ratio of the area of each vegetation zone to the total area of the catchment as for each direction in each elevation zone using a model(see apendex1) and sum of the this ratio's should be 1 other wise HBV model does not run.

Precipitaion(P),Temperature(T) and Discharge(Q)

The PTQ-file contains time series of precipitation [mm/Δt], temperature [ºC] and discharge [mm/Δt]. If the catchment consists of more than one sub catchment, a distinct set has to be specified for each of the sub catchments. Time series can be daily, hourly basis, or any other time interval, as long as the time interval remains constant over the time series. The areal average precipitation is calculated as a weighted mean of precipitation stations in and around the catchment. The weight c_i of station i can be determined subjectively or by Thiessen polygons or by the isohyetal method. In this case I have used simple arithmetic mean and determined the weight of each station determined in the Figure 6.4

Temperature data is needed in catchments with snow and is calculated as a weighted mean of stations in and around the catchment. When different elevation zones are used temperature will be corrected for elevation above sea level with usually -0.6 ^{0}C per 100 m (parameter TCALT).

And Discharge(Q) is obtained from gauge station that is present at the tongue of the glacier that measured the glacier discharge from 2003-2009 after that this station stopped functioning and was not replaced so we have a limited amount of time series data for the analysis but HBV model becuase we need atleast 10 years data to run a robust HBV model. Let's see how the stimulation go with this limited amount of data.

So now we need to calibrate the catchment parameters for different routines (snow routine soil moisture routine, Glacier routine, Response routine, routing routine) described in Chapter 4.

Calibration of HBV Model

There are various steps which we can follow for the calibration of HBV model.

- Trial-and-error or automatic calibration
- Different criteria can be used to assess the fit of simulated runoff to observed runoff: visual inspection of plots with Q_{Sim} and Q_{Obv} and statistical criteria.

- The coefficient of efficiency, R_{eff} (Nash Sutcliffe coefficient), is normally used for assessment of simulations by the HBV model.

Automatic calibration

In order to speed up the calibration process HBV light offers a tool called Monte Carlo stimulation. The Monte Carlo simulation is a mathematical technique that predicts possible outcomes of an uncertain event. Computer programs use this method to analyse past data and predict a range of future outcomes based on a choice of action. In this stimulation we can define lower and upper limit of each parameter and Run the model by defining the Coefficient of efficiency R_{eff} >0.5 is defined to save all the calibrated parameters which has R_{eff}>0.5.So my stimulation I defined R_{eff} >0.7 and saved all the calibrated parameters for this coefficient of Efficiency.From this parameters I have chosen the the parameters which has highest R_{eff} value and I stimulated the discharge of the catchment and output is reported in Below Figure 8.3 with model efficiency 0.7454 and this is the best estimate I can get with the available data.

HBV-BELEVEDRE

Water Balance [mm/year]		Subcatchment 1
Sum Qsim	=	1827
Sum Qobs	=	1907
Sum Precipitation	=	518
Sum AET	=	168
Sum PET	=	537
Contribution of Q1	=	0.000
Contribution of Q2	=	0.036
Goodness of fit		
Coefficient of determination	:	0.7468
Model efficiency	:	0.7454

Figure 8.3 Summary of the model stimulation from the HBV light for the calibrated parameters using Monte Carlo stimulation.

CHAPTER 9

Validation of Results

In this chapter we will investigate the quality of the DEM obtained from stereoscopic and Insar techniques from SPOT 5 and Sentinel-1 satellites which were used during data processing in this thesis which we discussed in chapter 4.

To measure the quality of any DEM produced from we need the time invariant points (GCP'S) in our study area. The invariant points helps us to see the bias between the elevations of the DEM(produced) and the GCP'S which are collected around the study area manually using total station network around the study area and points should have high precision and accuracy .But the data processing done in chapter 7 doesn't have any GCP'S for Aug 2003 SPOT 5 Scenes for our study area described in chapter 5 so to evaluate the accuracy of the DEM generated so I have to manually added the control points along the boundary of glacier as shown in Figure 7.2 for the scenes of spot 5 images belvedere glacier from generated from Politecnico di Torino glaciology lab as described in chapter 5 which has an accuracy of 40cm see figure 6.1.This is   approximation made due data availability limitations and to proceed to data processing the images for SPOT 5 in Meta shape software. The reference DEM used for the evaluation of accuracy of the DEM's obtained at the end of data processing in chapter 6 see Figure 7.3 and Figure 7.11 is DTM 10 for more details about see chapter 6 which is easily available from the website of geoportal of Piemonte region for the whole Piemonte region. And the results obtained are not very promising which we you see in RMSE values in Table 9.1 for Spot DEM and sentinel 1 DEM for the years 2003 and 2019.

The main stage for assessing the accuracy is the

- Generation of error map using raster calculator using pixel to pixel analysis as shown in Figure 8.1 and Figure 8.2. The elevation difference between the reference DEM and DEM obtained from spot 5 is very high which has ridiculous variation between -1093m and 2075m compared to DEM obtained from sentinel 1 Images has a better variation of between 1820m to 93 m,
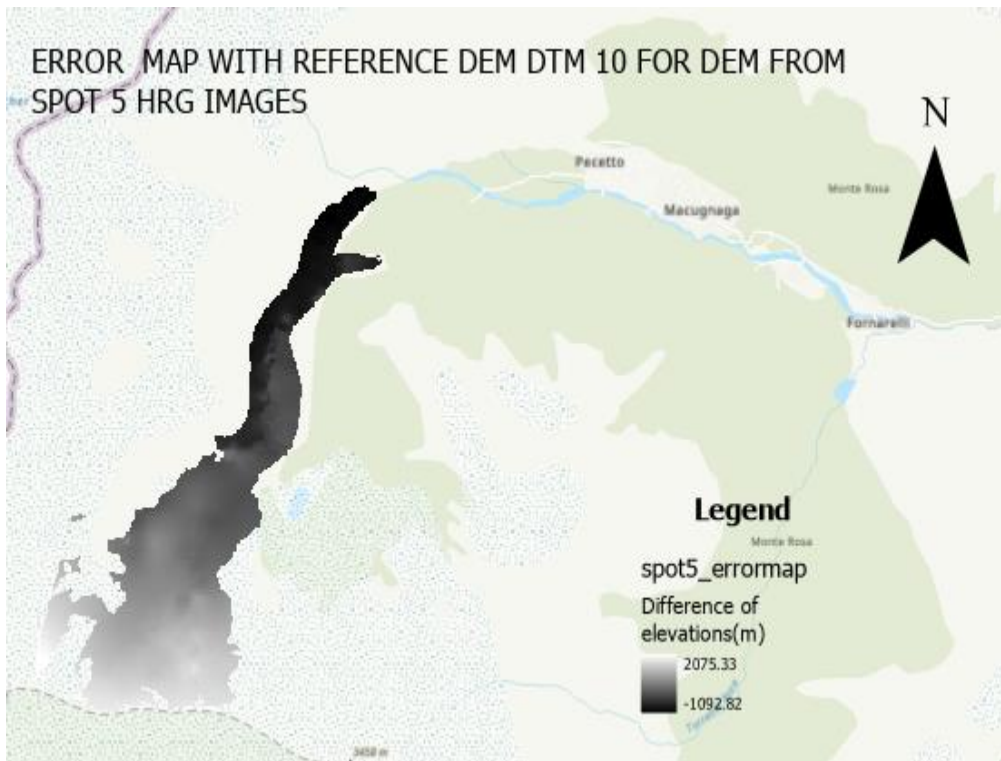
Figure 9.1 This error map is generated using raster calculator for the dem obtained in Figure 7.3 from spot 5 images with reference to DTM 10 and we can see in the above map the elevation difference between each pixel of the DEM is very high, so the quality of DEM is not very good.
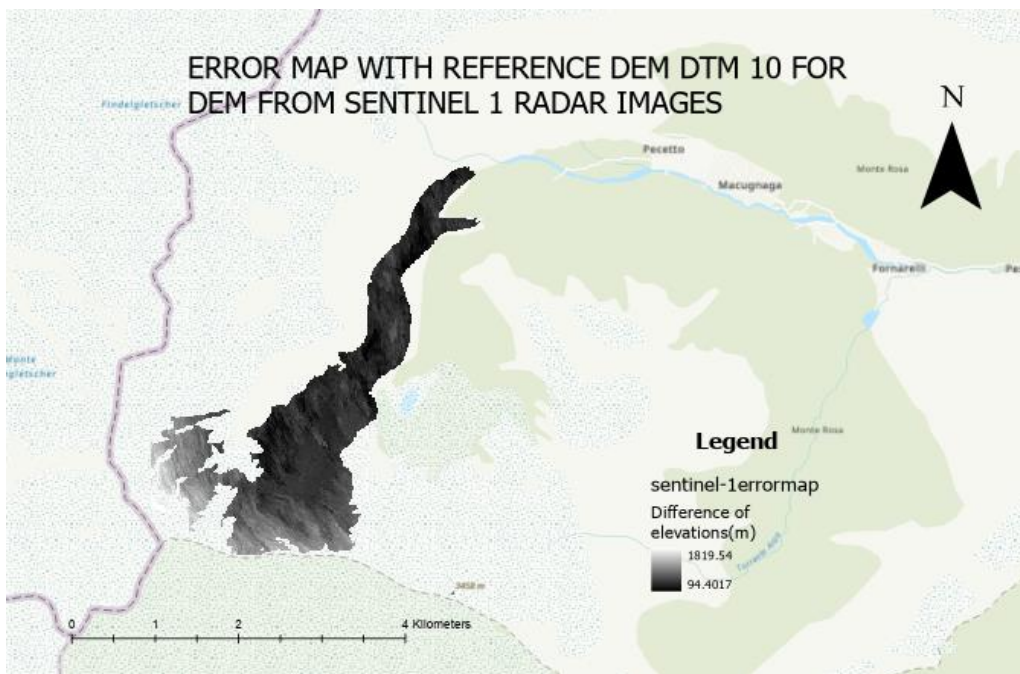
Figure 9.2 This error map is generated using raster calculator for the DEM obtained in Figure 7.11 from sentinel images with reference to DTM 10 and the elevation difference between each pixels of the DEM is not very high compared to spot 5 DEM.

Root Mean Square Error(RMSE)

Calculate RMSE value by converting the error maps into points as shown in Figure 9.1 and Figure 9.2. And then using field statistics RMSE has been estimated for both DEM in Figure 7.3 and Figure 7.11 is reported in below Table 9.1.

Satellite platform	RMSE of DEM(m)
SPOT 5	741
SENTINEL 1	247

Table 9.1 RMSE values of the elevation (vertical accuracy) of DEM with respective to reference DEM (DTM 10)

From RMSE values in Table 9.1 we can conclude that the DEM'S obtained in Figure 7.3 and 7.11 has lot of noise and DEM's obtained are not very reliable for the calculation of volume loss for the belvedere glacier between 2003 and 2019 to have multitemporal view of the glacier which was the one of the aims of this thesis.

CONCLUSION

While working with the open-source satellite data to monitoring glaciers there are lot of limitations the first limitation in my case using Spot-5 imagery is the resolution which is 5m we need better resolution in the order of centimetres which can be obtained only from the commercial satellite images described in Table 5.1 but the cost for each image is around 250 euros for minimum of 25km^2 for each image for the area of our interest and second limitation is the cloud cover of the image its very difficult to find a very clear cloud cover images around the belvedere glacier and the shadows of the clouds are present on glacier see Figure 7.2 this will not help the software meta shape to generate a very good quality dense point cloud which is need to generate a good quality DEM and one more big limitation is old satellite images from does not have rationalized polynomial coefficient's which is a compulsory need for metashape software to process the satellite images and this is mostly available in latest commercial satellite imagery Beijing-3A, Ikonos, Planet Labs, Pleiades, SuperView, Jilin, WorldView etc.Due to these limitations the DEM quality from the Spot 5 is varying from 1km to 2km which does not make any sense where as DEM generated from Sentinel 1 radar image the DEM quality varies from 93m to 1.8km even this is not a good enough estimate to estimated the volume lost in the glacier from time period between 2003 and 2019.But Sentinel 1 imagery does not have any of the problems that spot 5 images since these are radar images they are not affected by cloud cover but they are affected by coherence of the image pair that has been used in InSAR process for the registration of the images to generate the DEM see Figure 7.7 more than 50% of the pixels are with coherence around 0.5 and 0.3 which is not good enough to generate good quality DEM at the end of the glacier period in the August. There are possible distortions in SAR images and they are shadow, foreshortening, and layover. Shadows on a SAR image indicate those areas on the ground which has not been illuminated by the SAR signal. Foreshortening occurs when the local incidence angle is smaller than the illumination angle, but larger than 0°. Layover is an extreme form of foreshortening. For small incidence angles or very steep ground relief features, the backscatter often returns from the top of the feature before the base. This occurs where the local incidence angle is greater than incidence angle. On the SAR image, this appears as if the highest point of the vertical feature is laid over top of its base in the direction of the sensor. Since our glacier in a rugged mountain terrain the SAR images may be subjected to these distortions this might have effected the elevations of the DEM generated from Sentinel 1 data and this might have contributed the high values in the difference in elevations as shown in Figure 9.2 and Finally regarding the HBV model for our catchment they main limitation is discharge data from Anza gauge station at the glacier tongue

which is available from 2003-2009 but even with this limited data and just with basic division of the catchment into 2 elevation zones and 3 vegetation zone this still gives a better a fit between observed discharge and stimulated discharge which is around 74 % model efficiency as shown Figure 8.3 so this might give still better results for this glacier if more input discharge data and dividing the catchment into more than 2 elevation zones until coefficient of determination converges to 1 and then model can used to compare the volume lost during the same time period which we were looking from satellite image method in order to see whether the values or comparable or not.

References

[1].Huggel, C., M. Carey, J.J. Clague and A. Kääb (eds.), 2015a: The high-mountain cryosphere: Environmental changes and human risks. Cambridge University Press, Cambridge. 363 pp. ISBN 9781107065840.

[2]. Jones, B. and B.C. O'Neill, 2016: Spatially explicit global population scenarios consistent with the Shared Socioeconomic Pathways. Environ. Res. Lett., 11(2016), 084003, doi:10.1088/1748-9326/11/8/084003.

[3] Janzwood, Scott. (2020). Confident, likely, or both? The implementation of the uncertainty language framework in IPCC special reports. Climatic Change. 162. 1-21. 10.1007/s10584-020-02746-x.

[4] RGI 7.0 Consortium, 2023. Randolph Glacier Inventory - A Dataset of Global Glacier Outlines, Version 7.0. Boulder, Colorado USA. NSIDC: National Snow and Ice Data Center. doi:10.5067/f6jmovy5navz. Online access: https://doi.org/10.5067/f6jmovy5navz

[5] Farinotti, D., Huss, M., Fürst, J. J., Landmann, J., Machguth, H., Maussion, F., & Pandit, A. (2019). A consensus estimate for the ice thickness distribution of all glaciers on Earth. Nature Geoscience, 12(3), 168-173.

[6] Solomina, O. N., Bradley, R. S., Jomelli, V., Geirsdottir, A., Kaufman, D. S., Koch, J., ... & Yang, B. (2016). Glacier fluctuations during the past 2000 years. Quaternary Science Reviews, 149, 61-90.

[7] Zemp, M., Frey, H., Gärtner-Roer, I., Nussbaumer, S. U., Hoelzle, M., Paul, F., ... & Vincent, C. (2015). Historically unprecedented global glacier decline in the early 21st century. Journal of glaciology, 61(228), 745-762.

[8] Medwedeff, W. G., & Roe, G. H. (2017). Trends and variability in the global dataset of glacier mass balance. Climate Dynamics, 48(9-10), 3085-3097.

[9] Gardner, A. S., Moholdt, G., Cogley, J. G., Wouters, B., Arendt, A. A., Wahr, J., ... & Paul, F. (2013). A reconciled estimate of glacier contributions to sea level rise: 2003 to 2009. science, 340(6134), 852-857.

[10] Lüning, S., Gałka, M., Bamonte, F. P., García-Rodríguez, F., & Vahrenholt, F. (2022). Attribution of modern Andean glacier mass loss requires successful hindcast of pre-industrial glacier changes. Journal of South American Earth Sciences, 104024.

[11] Tanoue, M., Hirabayashi, Y., & Ikeuchi, H. (2016). Global-scale river flood vulnerability in the last 50 years. Scientific reports, 6(1), 36021.

[12] Marzeion, B., Cogley, J. G., Richter, K., & Parkes, D. (2014). Attribution of global glacier mass loss to anthropogenic and natural causes. Science, 345(6199), 919-921.

[13] Bodin, X., Thibert, E., Sanchez, O., Rabatel, A., & Jaillet, S. (2018). Multi-annual kinematics of an active rock glacier quantified from very high-resolution DEMs: An application-case in the French Alps. Remote Sensing, 10(4), 547.

[14] Prinz, R., Nicholson, L. I., Mölg, T., Gurgiser, W., and Kaser, G.: Climatic controls and climate proxy potential of Lewis Glacier, Mt. Kenya, The Cryosphere, 10, 133–148, https://doi.org/10.5194/tc-10-133-2016, 2016.

[15] Rets, Ekaterina P; Popovnin, Viktor V; Toropov, Pavel A; Smirnov, Andrew M; Tokarev, Igor V; Chizhova, Julia N; Budantseva, Nadine A; Vasil'chuk, Yurij K; Kireeva, Maria B; Ekaykin, Alexey A; Veres, Arina N; Aleynikov, Alexander A; Frolova, Natalia L; Tsyplenkov, Anatolii S; Poliukhov, Alexey; Chalov, Sergey R; Aleshina, Maria A; Kornilova, Ekaterina D (2018): Glaciological, hydrological, meteorological observations and isotopes sampling results during 2007-2017 at Djankuat Glacier Station in the North Caucasus, Russia. PANGAEA, https://doi.org/10.1594/PANGAEA.894807, Supplement to: Rets, Ekaterina P; Popovnin, Viktor V; Toropov, Pavel A; Smirnov, Andrew M; Tokarev, Igor V; Chizhova, Julia N; Budantseva, Nadine A; Vasil'chuk, Yurij K; Kireeva, Maria B; Ekaykin, Alexey A; Veres, Arina N; Aleynikov, Alexander A; Frolova, Natalia L; Tsyplenkov, Anatolii S; Poliukhov, Aleksei A; Chalov, Sergey R; Aleshina, Maria A; Kornilova, Ekaterina D (2019): Djankuat glacier station in the North Caucasus, Russia: a database of glaciological, hydrological, and meteorological observations and stable isotope sampling results during 2007–2017. Earth System Science Data, 11(3), 1463-1481, https://doi.org/10.5194/essd-11-1463-2019.

[16]Wada, Y., Van Beek, L. P. H., Viviroli, D., Dürr, H. H., Weingartner, R., & Bierkens, M. F. (2011). Global monthly water stress: 2. Water demand and severity of water stress. Water Resources Research, 47(7).

[17]Moyer, A. N., Moore, R. D., and Koppes, M. N. (2016) Streamflow response to the rapid retreat of a lake-calving glacier. Hydrol. Process., 30: 3650–3665. doi: 10.1002/hyp.10890.

[18] Bard, A. et al., 2015: Trends in the hydrologic regime of Alpine rivers. Journal Of Hydrology, 529, 1823-1837,doi:10.1016/j.jhydrol.2015.07.052

[19] Bocchiola, D., 2014: Long term (1921-2011) hydrological regime of Alpine catchments in Northern Italy. Advances in Water Resources, 70, 51-64, doi:10.1016/j.advwatres.2014.04.017.

[20] Fleming, S. W., & Dahlke, H. E. (2014). Modulation of linear and nonlinear hydroclimatic dynamics by mountain glaciers in Canada and Norway: Results from information-theoretic

polynomial selection. Canadian Water Resources Journal/Revue canadienne des ressources hydriques, 39(3), 324-341.

[21] Mukhopadhyay, B., & Khan, A. (2014). A quantitative assessment of the genetic sources of the hydrologic flow regimes in Upper Indus Basin and its significance in a changing climate. Journal of Hydrology, 509, 549-572.

[22] Duethmann, D., Bolch, T., Farinotti, D., Kriegel, D., Vorogushyn, S., Merz, B., ... & Güntner, A. (2015). Attribution of streamflow trends in snow and glacier melt-dominated catchments of the T arim R iver, Central A sia. Water Resources Research, 51(6), 4727-4750.

[23] Reggiani, P., & Rientjes, T. H. M. (2015). A reflection on the long-term water balance of the Upper Indus Basin. Hydrology research, 46(3), 446-462.

[24] Beamer, J. P., Hill, D. F., Arendt, A., & Liston, G. E. (2016). High-resolution modeling of coastal freshwater discharge and glacier mass balance in the Gulf of Alaska watershed. Water Resources Research, 52(5), 3888-3909.

[25] Wang, L. et al., 2015: Glacier changes in the Sikeshu River basin, Tienshan Mountains. Quaternary International, 358,153-159, doi:10.1016/j.quaint.2014.12.028

[26] Brahney, J., Weber, F., Foord, V., Janmaat, J., & Curtis, P. J. (2017). Evidence for a climate-driven hydrologic regime shift in the Canadian Columbia Basin. Canadian Water Resources Journal/Revue canadienne des ressources hydriques, 42(2), 179-192.

[27] Kormann, C., Francke, T., Renner, M., & Bronstert, A. (2015). Attribution of high resolution streamflow trends in Western Austria–an approach based on climate and discharge station data. Hydrology and Earth System Sciences, 19(3), 1225-1245.

[28] Jones, D. B., S. Harrison, K. Anderson and R. A. Betts, 2018: Mountain rock glaciers contain globally significant water stores. Scientific Reports, 8, 2834, doi:10.1038/s41598-018-21244-w

[29] Lamontagne-Hallé, P., McKenzie, J. M., Kurylyk, B. L., & Zipper, S. C. (2018). Changing groundwater discharge dynamics in permafrost regions. Environmental Research Letters, 13(8), 084017.

[30]Gruber, S. et al., 2017: Review article: Inferring permafrost and permafrost thaw in the mountains of the Hindu Kush Himalaya region. The Cryosphere, 11 (1), 81-99, doi:10.5194/tc-11-81-2017.

[31] Kenner, R. et al., 2017: Factors Controlling Velocity Variations at Short-Term, Seasonal and Multiyear Time Scales,Ritigraben Rock Glacier, Western Swiss Alps. Permafrost and Periglacial Processes, 28 (4), 675-684,doi:10.1002/ppp.1953.

[32] Niu, F. et al., 2012: Development and thermal regime of a thaw slump in the Qinghai–Tibet plateau. Cold Regions Science and Technology, 83–84, 131-138, doi:10.1016/j.coldregions.2012.07.007.

[33] Paul, F., Kääb, A., & Haeberli, W. (2007). Recent glacier changes in the Alps observed by satellite: Consequences for future monitoring strategies. Global and Planetary Change, 56(1-2), 111-122.

[34] Arenson, L. U., W. Colgan and H. P. Marshall, 2015a: Chapter 2 - Physical, Thermal, and Mechanical Properties ofSnow, Ice, and Permafrost. In: Snow and Ice-Related Hazards, Risks, and Disasters [Shroder, J. F., W. Haeberli and C. Whiteman (eds.)]. Academic Press, Boston

[35] Stoffel, M. and C. Graf, 2015: Debris-flow activity from high-elevation, periglacial environments.[Huggel, C., M.Carey, J. J. Clague and A. Kääb (eds.)]. Cambridge University Press, Cambridge, 295-314.

[36] Wirz, V., M. Geertsema, S. Gruber and R. S. Purves, 2016: Temporal variability of diverse mountain permafrost slope movements derived from multi-year daily GPS data, Mattertal, Switzerland. Landslides, 13 (1), 67-83, doi:10.1007/s10346-014-0544-3.

[37] Allen, S. K., S. C. Cox and I. F. Owens, 2011: Rock avalanches and other landslides in the central Southern Alps of New Zealand: a regional study considering possible climate change impacts. Landslides, 8 (1), 33-48, doi:10.1007/s10346-010-0222-z.

[38] Ravanel, L. and P. Deline, 2011: Climate influence on rockfalls in high-Alpine steep rockwalls: The north side of the Aiguilles de Chamonix (Mont Blanc massif) since the end of the 'Little Ice Age'. The Holocene, 21 (2), 357-365, doi:10.1177/0959683610374887.

[39] Fischer, L. et al., 2012: On the influence of topographic, geological and cryospheric factors on rock avalanches and rockfalls in high-mountain areas. Natural Hazards and Earth System Sciences, 12 (1), 241-254,doi:10.5194/nhess-12-241-2012.

[40] Fischer, L., C. Huggel, A. Kääb and W. Haeberli, 2013: Slope failures and erosion rates on a glacierized high-mountain face under climatic changes. Earth Surface Processes and Landforms, 38 (8), 836-846, doi:10.1002/Esp.3355.

[41] Faillettaz, J., M. Funk and C. Vincent, 2015: Avalanching glacier instabilities: Review on processes and early warning perspectives. *Reviews of Geophysics*, **53** (2), 203-224, doi:10.1002/2014rg000466.
[42] Schweizer, J., Bruce Jamieson, J., & Schneebeli, M. (2003). Snow avalanche formation. Reviews of Geophysics, 41(4).
[43] Eckert, N., Keylock, C. J., Castebrunet, H., Lavigne, A., & Naaim, M. (2013). Temporal trends in avalanche activity in the French Alps and subregions: from occurrences and runout altitudes to unsteady return periods. Journal of Glaciology, 59(213), 93-114.
[44] Steinkogler, W., Sovilla, B., & Lehning, M. (2014). Influence of snow cover properties on avalanche dynamics. Cold Regions Science and Technology, 97, 121-131.
[45] Carrivick, J. L., & Tweed, F. S. (2016). A global assessment of the societal impacts of glacier outburst floods. Global and Planetary Change, 144, 1-16.
[46] Frey, H. et al., 2010: A multi-level strategy for anticipating future glacier lake formation and associated hazard potentials. Natural Hazards and Earth System Sciences, 10 (2), 339-352, doi:10.5194/nhess-10-339-2010.
[47] Gardelle, J., E. Berthier, Y. Arnaud and A. Kääb, 2013: Region-wide glacier mass balances over the Pamir-Karakoram-Himalaya during 1999-2011. The Cryosphere, 7 (4), 1263-1286, doi:10.5194/tc-7-1263-2013.
[48] Loriaux, T. and G. Casassa, 2013: Evolution of glacial lakes from the Northern Patagonia Icefield and terrestrial waterstorage in a sea-level rise context. Global and Planetary Change, 102, 33-40, doi:10.1016/j.gloplacha.2012.12.012.

[49] Benn, D. I., Bolch, T., Hands, K., Gulley, J., Luckman, A., Nicholson, L. I., ... & Wiseman, S. (2012). Response of debris-covered glaciers in the Mount Everest region to recent warming, and implications for outburst flood hazards. Earth-Science Reviews, 114(1-2), 156-174.

[50] Nrama, C., Daiyrov, M., Tadono, T., Yamamoto, M., Kääb, A., Morita, R., & Ukita, J. (2017). Seasonal drainage of supraglacial lakes on debris-covered glaciers in the Tien Shan Mountains, Central Asia. Geomorphology, 286, 133-142.

[51] Paul, F. and N. Mölg, 2014: Hasty retreat of glaciers in northern Patagonia from 1985 to 2011. Journal of Glaciology,60 (224), 1033-1043, doi:10.3189/2014JoG14J104.

[52] Zhang, G. et al., 2015: An inventory of glacial lakes in the Third Pole region and their changes in response to global warming. Global and Planetary Change, 131, 148-157, doi:10.1016/j.gloplacha.2015.05.013.

[53] Buckel, J., J. C. Otto, G. Prasicek and M. Keuschnig, 2018: Glacial lakes in Austria - Distribution and formation sincethe Little Ice Age. Global and Planetary Change, 164, 39-51, doi:10.1016/j.gloplacha.2018.03.003.

[54] Sun, J. et al., 2018a: Linkages of the dynamics of glaciers and lakes with the climate elements over the Tibetan Plateau.Earth Science Reviews, 185, 308-324, doi:10.1016/j.earscirev.2018.06.012.

[55] Carroll, D., Sutherland, D. A., Shroyer, E. L., Nash, J. D., Catania, G. A., & Stearns, L. A. (2015). Modeling turbulent subglacial meltwater plumes: Implications for fjord-scale buoyancy-driven circulation. Journal of Physical Oceanography, 45(8), 2169-2185.

[56] Round, V., Leinss, S., Huss, M., Haemmig, C., & Hajnsek, I. (2017). Surge dynamics and lake outbursts of Kyagar Glacier, Karakoram. The Cryosphere, 11(2), 723-739.

[57] Knight, P.G., 1999, Glaciers: Cheltenham, United Kingdom, Stanley Thornes Ltd., 261 p

[58] Mercanton, P.L., 1916, Vermessungen am Rhonegletscher. Mensurations au Glacier du Rhone 1874–1915: Geleitet und herausgegeben von der Gletscher-Kommission der Schweizerishen Naturforschenden Gesselschaft, v. LII, 190 p.

[59] Haeberli, W., 1998, Historical evolution and operational aspects of worldwide glacier monitoring, in Haeberli, W., Hoelzle, M., and Suter, S., eds., Into the Second Century of World Glacier Monitoring—Prospects and Strategies: Paris, UNESCO Publishing, 35–51.

[60] Riedel, J.L., and Burrows, R.A., 2005, Long term monitoring of small glaciers at North Cascades National Park: a prototype park for the North Coast and Cascades Network: North Cascades National Park, Washington, 39 p.

[61] Tangborn, W.V., 1980, Two models for estimating climate-glacier relationships in the North Cascades, Washington, USA: Journal of Glaciology, v. 25, p. 3–21.

[62] Paterson, W.S.B., 1994, The physics of glaciers, third edition: Oxford, Elsevier, 480 p.

[63] Hall, F.C., 2002, Photo point monitoring handbook: General Technical Report PNW-GTR-526, Portland, Oregon: U.S. Department of Agriculture, Forest Service, Pacific Northwest Research Station, 134 p.

[64] Østrem, G., 1975, ERTS data in glaciology—an effort to monitor glacier mass balance from satellite imagery: Journal of Glaciology, v. 16, p. 403–415.

[65] Meier, M.F., and Post, A.S., 1962, Recent variations in mass net budgets of glaciers in Western North America: International Association of Scientific Hydrology (IAHS), Publication No. 58, p. 63–77.

[66] Singh, P., and Singh, V.P., 2001, Snow and glacier hydrology: Dordrecht, Netherlands, Kluwer Academic Publishers, 742 p.

[67] Fountain, A.G., Krimmel, R.M., and Trabant, D.C., 1997, A strategy for monitoring glaciers: U.S. Geological Survey Circular 1132, 19 p.

[68] Kaser, G., Fountain, A., and Jansson, P., 2003, A manual for monitoring the mass balance of mountain glaciers: UNESCO, Paris, IHP-VI Technical Documents in Hydrology No. 59, 107 p.

[69] Hubbard, B., and Glasser, N.F., 2005, Field techniques in glaciology and glacial geomorphology: West Sussex, United Kingdom, John Wiley and Sons, 400 p.

[70] Cox, L.H., and March, R.S., 2004, Comparison of geodetic and glaciological mass-balance techniques, Gulkana Glacier, Alaska, U.S.A: Journal of Glaciology, v. 50, p. 363–370, doi: 10.3189/172756504781829855.

[71] Andreassen, L.M., 1999, Comparing traditional mass balance measurements with long-term volume change extracted from topographical maps: a case study of Storbreen glacier in Jotunheimen, Norway, for the period 1940–1997: Geografi ska Annaler, v. 81A, p. 467–476, doi: 10.1111/j.0435- 3676.1999.00076.x.

[72] Arendt, A.A., Echelmeyer, K.A., Harrison, W.D., Lingle, C.S., and Valentine, V.B., 2002, Rapid wastage of Alaska glaciers and their contribution to rising sea level: Science, v. 297, p. 382–386, doi: 10.1126/ science.1072497.

[73] Østrem, G., and Haakensen, N., 1999, Map comparison or traditional mass balance measurements: which method is better?: Geografi ska Annaler,v. 81A, p. 703–711, doi: 10.1111/j.0435-3676.1999.00098.x.

[74] Elsberg, D.H., Harrison, W.D., Echelmeyer, K.A., and Krimmel, R.M., 2001, Quantifying the effects of climate and surface change on glacier mass balance: Journal of Glaciology, v. 47, p. 649–658, doi: 10.3189/172756501781831783. lsberg, D.H., Harrison, W.D., Echelmeyer, K.A., and Krimmel, R.M., 2001, Quantifying the effects of climate and surface change on glacier mass balance: Journal of Glaciology, v. 47, p. 649–658, doi: 10.3189/172756501781831783.

[75] Huybrechts, P., De Nooze, P., and Decleir, H., 1989, Numerical modeling of Glacier d'Argentiere and its historic front variations, in Oerlemans, J., ed., Glacier fluctuations and climatic change: Boston, Kluwer Academic Publishers, p. 373–390.

[76] Porter, S.C., 1977, Present and past glaciation thresholds in the Cascade Range, Washington—Topographic and climatic controls and paleoclimatic implications: Journal of Glaciology, v. 18, p. 101–116.

[77] Meierding, T.C., 1982, Late Pleistocene glacial equilibrium-line altitudes in the Colorado Front Range: A comparison of methods: Quaternary Research, v. 18, p. 289–310, doi: 10.1016/0033-5894(82)90076-X.

[78] Rodbell, D.T., 1992, Late Pleistocene equilibrium-line reconstructions in the northern Peruvian Andes: Boreas, v. 21, p. 43–52.

[79] Williams, R.S., Jr., Hall, D.K., and Benson, C.S., 1991, Analysis of glacier facies using satellite techniques: Journal of Glaciology, v. 37, p. 120–128.

[80] Berthier, E., Vadon, H., Baratoux, D., Arnaud, Y., Vincent, C., Feigl, K.L., Remy, F., and Legresy, B., 2005, Surface motion of mountain glaciers derived from satellite optical imagery: Remote Sensing of Environment, v. 95, p. 14–28, doi: 10.1016/j.rse.2004.11.005.

[81] Molnia, B.F., 1993, Major glacier surge continues: Eos (Transactions, American Geophysical Union), v. 74, p. 521–524, doi: 10.1029/93EO00675.

[82] Hooke, R.L., 2005, Principles of glacier mechanics: Cambridge, United Kingdom, Cambridge University Press, 429 p.

[83] Bergstrom, S. (1976) Development and Application of a Conceptual Runoff Model for Scandinavian Catchments. SMHI, Reports RHO, 7.

[84]https://www.researchgate.net/publication/223572580_Development_and_test_of_the_distributed_HBV-96_hydrological_model

[85] Köplin, N., Schädler, B., Viviroli, D. and Weingartner, R.: The importance of glacier and forest change in hydrological climate-impact studies, Hydrol. Earth Syst. Sci., 17(2),

619–635, doi:10.5194/hess-17-619-2013, 2013.

[86] Miller, J. D., Immerzeel, W. W. and Rees, G.: Climate Change Impacts on Glacier Hydrology and River Discharge in the Hindu Kush – Himalayas A Synthesis of the Scientific Basis, Mt. Res. Dev., 32(4),461–467, doi:10.1659/MRD-JOURNAL-D-12-00027.1, 2012.

[87] Stahl, K., Weiler, M., Kohn, I., Seibert, J., Vis, M. and Gerlinger, K.: The snow and glacier melt components of streamflow of the river Rhine and its tributaries considering the influence of climate change, Final report to the International Commission for the Hydrology of the Rhine Basin (CHR).[online] Available from: www.chr-khr.org/en/publications, 2017.

[88] Hagg, W., Braun, L. N., Kuhn, M. and Nesgaard, T. I.: Modelling of hydrological response to climate change in glacierized Central Asian catchments, J. Hydrol., 332(1–2), 40–53,doi:10.1016/j.jhydrol.2006.06.021, 2007.

[89] Granshaw, F.D., 2002, Glacier change in the North Cascade National Park Complex, Washington, 1958 to 1998 [M.S. Thesis]: Portland State University, 94 p.

[90] Vadon, H., and Berthier, E., 2004, Measurement of glacier velocity fields using very precise multitemporal correlation on high resolution SPOT5 images: ISPRS Symposium, Istanbul, July 2004.

[91] Longley, Paul A.; Goodchild, Michael F.; Maguire, David J.; Rhind, David W. (2011). Geographic Information Systems & Science (3rd ed.). Wiley.

[92] Huss, M., Farinotti, D., Bauder, A. and Funk, M.: Modelling runoff from highly glacierized alpine drainage basins in a changing climate, Hydrol. Process., 22, 3888–3902, doi:10.1002/hyp, 2008.

[93] Stahl, K., Moore, R. D., Shea, J. M., Hutchinson, D. and Cannon, A. J.: Coupled modelling of glacier and streamflow response to future climate scenarios, Water Resour. Res., 44(2), W02422, 1–13, doi:10.1029/2007WR005956, 2008.

[94] Linsbauer, A., Paul, F. and Haeberli, W.: Modeling glacier thickness distribution and bed topography over entire mountain ranges with GlabTop: Application of a fast and robust approach, J. Geophys. Res.,117(F3), F03007, doi:10.1029/2011JF002313, 2012.

[95] Radić, V., Hock, R. and Oerlemans, J.: Analysis of scaling methods in deriving future volume evolutions of valley glaciers, J. Glaciol., 54(187), 601–612, doi:10.3189/002214308786570809, 2008

[96] Stahl, K., Moore, R. D., Shea, J. M., Hutchinson, D. and Cannon, A. J.: Coupled modelling of glacier and streamflow response to future climate scenarios, Water Resour. Res., 44(2), W02422, 1–13, doi:10.1029/2007WR005956, 2008.

[97] Bongio, M., Avanzi, F. and De Michele, C.: Hydroelectric power generation in an Alpine basin: Futurewater-energy scenarios in a run-of-the-river plant, Adv. Water Resour., 94, 318–331,doi:10.1016/j.advwatres.2016.05.017, 2016.

[98] Immerzeel, W. W., Shrestha, A. B., Bierkens, M. F. P., Beek, L. P. H. and Konz, M.: Hydrological response to climate change in a glacierized catchment in the Himalayas, Clim. Change, 110, 721–736,doi:10.1007/s10584-011-0143-4, 2012.

[99] Huss, M., Jouvet, G., Farinotti, D. and Bauder, A.: Future high-mountain hydrology: a new parameterization of glacier retreat, Hydrol. Earth Syst. Sci., 14(5), 815–829, doi:10.5194/hess-14-815-30 2010, 2010.

[100] Farinotti, D., Usselmann, S., Huss, M., Bauder, A. and Funk, M.: Runoff evolution in the Swiss Alps: projections for selected high-alpine catchments based on ENSEMBLES scenarios, Hydrol. Process.,26(13), 1909–1924, doi:10.1002/hyp.8276, 2012.

[101] Finger, D., Hugentobler, A., Huss, M., Voinesco, A., Wernli, H., Fischer, D., Weber, E., Jeannin, P.-Y.Y., Kauzlaric, M., Wirz, A., Vennemann, T., Hüsler, F., Schädler, B. and Weingartner, R.: Identification of glacial meltwater runoff in a karstic environment and its implication for present andfuture water availability, Hydrol. Earth Syst. Sci., 17(8), 3261–3277, doi:10.5194/hess-17-3261-2013,2013.

[102] Gabbi, J., Farinotti, D., Bauder, A. and Maurer, H.: Ice volume distribution and implications on runoff projections in a glacierized catchment, Hydrol. Earth Syst. Sci., 16(12), 4543–4556, doi:10.5194/hess16-4543-2012, 2012.

[103] Huss, M. and Fischer, M.: Sensitivity of Very Small Glaciers in the Swiss Alps to Future Climate Change, Front. Earth Sci., 4(April), 1–17, doi:10.3389/feart.2016.00034, 2016.

[104] Huss, M., Zemp, M., Joerg, P. C. and Salzmann, N.: High uncertainty in 21st century runoff projections from glacierized basins, J. Hydrol., 510, 35–48, doi:10.1016/j.jhydrol.2013.12.017, 2014.

[105] Sorg, A., Huss, M., Rohrer, M., & Stoffel, M. (2014). The days of plenty might soon be over in glacierized Central Asian catchments. Environmental Research Letters, 9(10), 104018.

[106] Addor, N., Rössler, O., Köplin, N., Huss, M., Weingartner, R. and Seibert, J.: Robust changes and sources of uncertainty in the projected hydrological regimes of Swiss catchments, Water Resour. Res.,50, 1–22, doi:10.1002/2014WR015549, 2014.

[107] Gabbi, J., Carenzo, M., Pellicciotti, F., Bauder, A. and Funk, M.: A comparison of empirical and physically based glacier surface melt models for long-term simulations of glacier response, J. Glaciol.,60(224), 1199–1207, doi:10.3189/2014JoG14J011, 2014.

[108] Linsbauer, A., Paul, F., Machguth, H. and Haeberli, W.: Comparing three different methods to modelscenarios of future glacier change in the Swiss Alps, Ann. Glaciol., 54(63), 241–253,doi:10.3189/2013AoG63A400, 2013.

[109] Ragettli, S., Pellicciotti, F., Bordoy, R. and Immerzeel, W. W.: Sources of uncertainty in modeling theglaciohydrological response of a Karakoram watershed to climate change, Water Resour. Res., 49(9),6048–6066, doi:10.1002/wrcr.20450, 2013.

[110] Salzmann, N., Machguth, H. and Linsbauer, A.: The Swiss Alpine glaciers" response to the global "2 ^{0}C air temperature target," Environ. Res. Lett., 7(4), 44001, doi:10.1088/1748-9326/7/4/044001, 2012

[111] Vincent, C., Harter, M., Gilbert, A., Berthier, E. and Six, D.: Future fluctuations of Mer de Glace, French Alps, assessed using a parameterized model calibrated with past thickness changes, Ann.Glaciol., 55(66), 15–24, doi:10.3189/2014AoG66A050, 2014.

[112] Li, H., Beldring, S., Xu, C.-Y., Huss, M., Melvold, K. and Jain, S. K.: Integrating a glacier retreat model into a hydrological model – Case studies of three glacierised catchments in Norway andHimalayan region, J. Hydrol., 527, 656–667, doi:10.1016/j.jhydrol.2015.05.017, 2015.

[113]https://www.researchgate.net/publication/200459375_Elevation_modelling_from_satellite_visible_and_infrared_VIR_data

[114] Toutin, T., 1995. Generating DEM from Stereo Images with a Photogrammetric Approach: Examples with VIR and SAR Data. EARSeL Journal "Advances in Remote Sensing", vol. 4, No. 2, pp. 110–117.

[115] 3D GLACIER MAPPING BY MEANS OF SATELLITE STEREO IMAGES: THE BELVEDERE GLACIER CASE STUDY IN THE ITALIAN ALPS / Giulio Tonolo, F.; Cina, A.; Manzino, A.; Fronteddu, M.. - In: THE INTERNATIONAL ARCHIVES OF THE PHOTOGRAMMETRY, REMOTE SENSING AND SPATIAL INFORMATION SCIENCES. - ISSN 1682-1777. - ELETTRONICO. - XLIII-B2-2020:(2020), pp. 1073-1079. [10.5194/isprs-archives-XLIII-B2-2020-1073-2020].

[116]Glacier hazards at Belvedere glacier and the Monte Rosa east face, Italian Alps: Processes and mitigation by Andreas Kääb,Christian Huggel ,Secondo Barbeto

[117] Diolaiuti, G., D'Agata, C., & Smiraglia, C. (2003). Belvedere Glacier, Monte Rosa, Italian Alps: tongue thickness and volume variations in the second half of the 20th century. Arctic, Antarctic, and Alpine Research, 35(2), 255-263.

[118] Latry, C., & Rouge, B. (1998, October). Spot5 thr mode. In Earth observing systems III (Vol. 3439, pp. 480-491). SPIE.

[119] Braun, A. (2021). Retrieval of digital elevation models from Sentinel-1 radar data – open applications, techniques, and limitations. Open Geosciences, 13(1), 532-569. https://doi.org/10.1515/geo-2020-0246

[120] Geudtner, D., Prats, P., Yague-Martinez, N., Navas-Traver, I., Barat, I., & Torres, R. (2016, June). Sentinel-1 SAR interferometry performance verification. In Proceedings of EUSAR 2016: 11th European Conference on Synthetic Aperture Radar (pp. 1-4). VDE.

Data sources used:

Copernicus Sentinel data 2019, processed by ESA.

SPOT 5 Data 2003 courtesy of Spot world heritage data base.